SAPIENZA
UNIVERSITÀ DI ROMA

Modelling facies heterogeneity in carbonate ramp systems. From petrophysical characteristics to forward modelling

Faculty of Mathematical, Physical and Natural Sciences
XXXIV PhD cycle in Earth Sciences

Ph.D. student: Andrea Tomassi

Supervisor
Fabio Trippetta

Co-supervisor
Marco Brandano

SSD GEO/03

Table of contents

Introduction

In the last decades digital modelling applied to geological research is getting increasing attention (Alaei, 2012; Tomassetti et al., 2018; Trippetta et al., 2020; De Franco et al., 2019; Mascolo and Lecomte, 2021). Indeed, relevant implications both in scientific and economic terms could be inferred by using this technique. In particular, the application of digital models in complex geologic scenarios is critical for the understanding of potentially exploitable systems from multiple perspectives. Starting from the most classical model application for the exploitation of oil and gas fields passing through the implementation of extraction strategies - by reducing uncertainties (Macgregor & Moody, 1998; Racey 2001) - digital models find new place in latest applications such as natural gas storage. Recently, models are also applied for the study of geological bodies, potential reservoirs for the CO_2 or hydrogen injection (Dockrill and Shipton, 2010; Trippetta et al., 2013; Aminu et al., 2017; Heinemann et al., 2018). Modelling contribute and facilitate to capture and store gases in the subsurface, balancing their release into the atmosphere. Digital modelling represents one of the major innovative strategies in the control of greenhouse gases concentration in atmosphere, a currently trending topic from media, public opinion, and political points of view. Another possible application of digital models for subsurface gas storage involves the monitoring of reservoirs in order to ascertain and quantify gas leakage through fault or fracture systems (Wang et al., 2018). Moreover, radioactive waste storage could be integrated as current and powerful employment of digital models (Malvić et al., 2020). In particular, the technological tools used for these purposes are called forward models since their outcomes gives predictive results on the processes happened in the past and protracted towards the future. They appear extremely suitable for the study of geological subsurface formations that can be also applied to an emerging field such as the development of geothermal energy power plants (De Franco et al., 2019). All these are topics of great actuality since world governments' plans are

directed towards the total replacement of classic energy sources from hydrocarbons with green energies.

However, digital modelling needs input data such as geometries and rock properties that should be well constrained. Seismic exploration is probably the most powerful tool for investigating subsurface rock formations (Avseth et al., 2010). Important progress has been made in recent years, but significant problems remain in the geologic interpretation of seismic data. The reflections that can be read in seismic data depend on the Acoustic Impedance (AI) contrast in the transit of the P-wave between layers in the subsurface. AI depends on the density (ρ) and the P-wave velocity (Vp) of the medium through which wave propagates (AI= ρ Vp). These petrophysical characteristics, in turn, are controlled by structure, texture, porosity, and boundary conditions of the rocks (Dvorkin et al., 2014; Tomassetti et al., 2018; Trippetta et al., 2020; Brandano et al., 2020). These two links, one between rock structure and its elasticity and the other between elasticity and signal propagation, form the physical basis of seismic interpretation (Anselmetti and Eberli, 1993; Eberli et al. 2003; Weger et al. 2009; Hairabian et al. 2014; Dvorkin et al., 2014). Dealing with these relationships, we are facing the so-called inverse problem. We see from seismic sections the resulting seismic images of rock formations where the same signal can be the result of a combination of different features. It should be, thus, very useful to well understand what are the features that lead to a certain seismic image.

Synthetic seismic modelling (or forward modelling) is a fundamental prospecting method for understanding the features leading to the corresponding seismic images of subsurface structures and reservoir architectures (Alaei, 2012). Forward modelling methodology, as approach to the interpretation of seismic data, involves the detailed characterization of lithology, density, porosity, seismic velocity and fluid in the rock, as well as the reservoir geometry. As a result, the corresponding seismic properties are calculated, and then synthetic seismic traces are generated. These issues became essential for lithologies characterized by a complex seismic interpretation (Al-Salmi et al., 2019).

In addition, synthetic seismic forward models allow accurate analysis of fault zones. The study of seismic response in fault zones is crucial since the

fracturing or compaction that faults create strongly modifies the petrophysical characteristics of rocks by affecting their properties (Botter et al., 2017; Kolyukhin et al., 2017). Synthetic seismic forward models are, therefore, mandatory for the comprehension of faults behaviour through seismic imaging. Faults play a key role in reservoirs by increasing or limiting fluid flow. Even if interpretation of seismic data is a pivotal method for studying the subsurface, the internal structure and properties of fault zones are often below the limit imposed by seismic resolution (Botter et al., 2017). Despite the impact of faults on reservoir permeability, modelling tools and workflows still lack for realistic representation of fault zones in models (Tveranger et al., 2005; Braathen et al., 2009; Manzocchi et al., 2010).

With facies analysis and petrophysical data it is possible to build field-based digital models fundamental in understanding architectures of carbonate sedimentary bodies which often constitute reservoir surface analogues of buried world-wide petroleum systems, CO_2, hydrogen, radioactive waste storage sites and geothermal fields. Surface analogues are rocks with depositional, textural, and petrophysical characteristics similar to those constituting the petroleum system, but they outcrop on the surface. Starting from petrophysical characteristics of facies, forward models can be built.

In this thesis, as a case study for the development of a forward model, rocks belonging to the carbonate realm, more specifically carbonate ramps, were analyzed.

Carbonate ramps constitute important hydrocarbon deposits in North Africa (Macgregor & Moody, 1998), Venezuela, and many other regions of the World (Racey, 2001) due to their excellent porosity and permeability characteristics. However, the depositional model that is the basis for a proper interpretation produces many uncertainties arising from the difficulty in attributing different facies to a depositional environment and process due to the poor occurrence of sedimentary structures (Buxton and Pedley, 1989; Pomar and Kendall, 2008; Burchette, 2012; Bassi et al., 2013; Tomassetti et al., 2018; Tomassetti et al., 2022). In addition, strong lateral heterogeneity in terms of petrophysical characteristics, components, structure, and texture leads to complex distinction of facies belts (Tomassetti et al., 2018; Trippetta et al., 2020; Brandano et al., 2020). To overcome these issues, quantification of

petrophysical characteristics can be crucial in understanding facies heterogeneity from a physical perspective to be incorporated in synthetic seismic forward models building. Carbonate rocks are often difficult to interpret seismically because the slight acoustic impedance contrast at the interface between carbonate facies in subsurface does not allow a clear resolution of major reflectors and reservoir formations. Strong constraints are often imposed by geophysical survey techniques characterized by low resolution especially in carbonates and interpretation capabilities that depend on the interpreter skill (Tomassetti et al., 2018; Trippetta and Geremia, 2019; Faleide et al., 2021). These constraints can be overtaken through the modelling of surface analogues allowing a detailed analysis on the facies association but also their petrophysical characteristics and seismic properties such as acoustic impedance (Tomassetti et al., 2018; Lipparini et al., 2018; Trippetta and Geremia, 2019; Brandano et al., 2020).

In order to analyse the petrophysical characteristics and seismic response of the carbonate realm through modelling two carbonate ramps both belonging to the Adria plate were considered as case studies. The first is the Chattian carbonate ramp of the Porto Badisco calcarenite outcropping in the southern Salento peninsula, the southernmost portion of the Apulian carbonate platform. The Porto Badisco carbonate ramp is an excellent surface analogue of exploited oil and gas field in the offshore Venezuela, Philippine and South China Sea (Zampetti et al., 2005; Sattler et al.,2004; Fournier and Borgomano, 2007; Lallier et al., 2012; Marini and Spadafora, 2014; Pomar et al., 2015; Valencia and Laya, 2020) as well as fields in offshore Adriatic Sea such as Ombrina Mare field (Campagnoni et al., 2013). In this carbonate system firstly the analysis of outcropping facies was carried out observing over 100 thin sections produced. Consequently facies association modelling was performed through Petrel software (mark of Schlumberger) using TGSim stochastic approach algorithm adopting the depositional model based on field data. This model is useful for qualitatively understand the broad facies spacial distribution which reflects the abrupt heterogeneity from a sedimentary point of view. To physically quantify the lateral facies heterogeneity the petrophysical characteristics such as porosity, density and seismic velocity were measured and analyzed through a multi-analytical approach. Density

measurements were carried out with the helium pycnometer. Porosity was firstly calculated from the density data and then was additionally measured through image analysis and point counting to cross-correlate the values. Seismic velocity was measured by using an ultrasonic generator connected to piezoelectic transducers and to an oscilloscope. The analysis performed on the carbonate ramp outcropping in Porto Badisco offers the opportunity to analyze facies heterogeneity, modeling its distribution and physically quantifying it through petrophysical characterization. From the petrophysical data, it was possible to construct 2D models of the distribution of porosity and P-wave seismic velocity along the depositional model.

This study, which can be applied globally to carbonate platforms, emphasizes with the modelling exercise how facies heterogeneity is an intrinsic feature of these systems. The petrophysical characterization which provides quantitative values to the heterogeneity allow to build more complex models such as seismic forward models discussed in the second chapter.

The other case study is represented by the Cenozoic carbonate ramp outcropping on the Majella Massif in Abruzzi, the northernmost portion of the Apulian carbonate platform which gives the opportunity to study a carbonate ramp surface analogue of a buried reservoir. Also in Majella the Oligo-Miocene stratigraphic interval represented by the Bolognano Formation which is the reservoir of the system is considered an excellent surface analogue of the productive fields in the Adriatic Sea, offshore Venezuela, Philippines and many others worldwide (Tomassetti et al., 2021). Specifically, this system offers the opportunity to integrate the facies heterogeneity in the synthetic seismic forward modelling and understand its seismic response without the introduction of artificial noise to obtain additional information. On the Majella Massif a model of the facies heterogeneity to understand their seismic response was performed. After analyzing the facies and measuring their petrophysical characteristics, the data obtained were used as input for build a 3D property modelling in Petrel software representing the entire carbonate ramp from the topographic surface to the Upper Cretaceous from the platform top going towards the basin located northward from the Majella Massif. From the 3D model was cut a section whose data were used as input in Matlab (mark of Mathworks) in order to perform the synthetic seismic forward model

with the geophysical codes provided by the CREWES consortium. The resulting forward model represent the seismic response of the facies heterogeneity of carbonate rocks. In addition, from the obtained seismic images it is possible to evaluate the presence of hydrocarbons and to identify how the presence of important bituminous impregnations – that can be appreciated in the field in Majella – modify the seismic response. The workflow developed to quantify the signature of the facies heterogeneity of carbonate rocks and the presence of infilling hydrocarbons is applicable to other systems worldwide, which is a large issue that is still open and can help in the problems relative to seismic interpretation associated with these systems.

Given the presence of a buried normal fault system in the study area, a forward modelling in the fault zones was performed as well. By measuring the petrophysical characteristics of the fault rocks characterized by both fracturing or compaction, fault zones were modeled. Two end member scenarios with two opposite behaviors of the rocks belonging to the damage zone were modeled in Matlab. A scenario in which the damage zone is characterized by fracturing and therefore rocks affected by greater porosity than the host rock. In the other scenario was modeled a damage zone with lower porosity than the host rock caused by the presence of compaction bands. Consequently, the seismic response of these end members was compared to understand how faults affect the seismic response of carbonate ramp systems. Notoriously, fault systems globally characterize carbonate ramps, and understanding their seismic response facilitates interpretation of the deformation behavior that a fault can assume under different boundary conditions. This can lead to an understanding of whether faults behave as barriers or conduits for fluids with the important implications for the study of fluid leakage from reservoirs.

Thesis objectives

The objective of this thesis is to improve the seismic interpretation capabilities of carbonate systems increasing knowledge on the seismic response of these rocks and the peculiarities that characterize them. The implications of this work are to be considered useful both in energy supply, improving the exploitation of oil systems or geothermal fields, and in identifying reservoir rocks for the storage of gas or radioactive waste in the subsurface. The application aim lies in employment of the results of this research to carbonate ramp systems globally. To pursue this goals was built a digital seismic model from outcrop and laboratory data that explains how frequent features in carbonate systems such as facies heterogeneity, hydrocarbons and faults affects the seismic response of rocks. Facies heterogeneity is modeled through the reconstruction of the depositional model and the facies association and distribution. This modelling should be also quantified through petrophysical and seismic properties measurements. The petrophysical characterization led to understand variations in acoustic impedance and corresponding seismic facies of different lithologies which are similar to formations currently acting as reservoirs in the subsurface. The goal is achieved by the construction of synthetic seismic sections in a seismic forward modelling allowing the characterization of the intervals that act as reservoirs. Moreover, forward modelling, also gives a reference model for seismic interpretation. From this model it is possible to quantify the petrophysical variations caused by heavy hydrocarbon presence and fault zones in order to understand how these strongly affect the seismic properties of rocks and to identify differences in the seismic facies. The achievement of the objectives in this thesis will bring new knowledge useful for digital modelling both in terms of facies and petrophysical heterogeneity and in terms of seismic response of rocks affected by the presence of hydrocarbons and fault zones.

Forward modelling is a tool widely used and has become essential in seismic interpretation (Routa and Mohanty, 2020). Quantifying the relationships between seismic data and real rock properties and their uncertainties have

become more critical in the last decade, especially after the great improvement in seismic acquisition and processing. There is an increased possibility and at the same time a need to interpret amplitudes in detail for hydrocarbon detection, reservoir characterization and monitoring (Avseth et al., 2005).

Forward models Increase the understanding and interpretation capabilities by delineating the seismic response of rocks leading to minimizing uncertainties in petroleum system management decisions (Neto et al., 2020; Danaei et al., 2020).

The connection between facies variations, petrophysical characteristics, and seismic response, which is the focus of this study, will allow to expand the knowledge on the mechanisms that control their dynamics.

Thesis overview

In the first part of this thesis, a brief introduction outlines the research objectives, the framework of the project and the innovation of the research. Potential achievement and advancement of knowledge and case studies are explored in the same section.

In the first chapter the petrophysical characterization and the facies heterogeneity digital modelling of a carbonate ramp system is analyzed, useful for understanding complex sedimentary systems.

The second chapter focuses on forward modelling of facies heterogeneity starting from the petrophysical characteristics of the involved rocks. It is also dedicated to synthetic seismic modelling, that represents a source of information for seismic interpretation of facies. The variations of seismic response caused by the presence of hydrocarbons impregnating the rocks are also discussed.

The same workflow is adopted in the third and final chapter. The analysis of the structures characterizing the systems – such as the faults – is presented.

Seismic response of fault systems is studied to clarifying the seismic behaviour of the rocks constituting the fault zone through seismic imaging.

Methods and workflow

In this thesis a complex workflow consisting of several preparatory steps, was built and developed (Fig. I). The methods and workflow here presented can be applied globally for synthetic forward seismic modelling of any type of geological situations and lithologies. Their application to reservoirs can lead to important implications overcoming the classic exploitation for the production of hydrocarbons thus reducing the uncertainties of management for extraction strategies. This workflow can bring both economic and scientific goals regarding the modelling for a huge number of fields *i.e*. mining strategies, CO_2, hydrogen or radioactive waste storage, gases leakage from reservoirs through fault systems, or the study for the exploitation of geothermal fields.

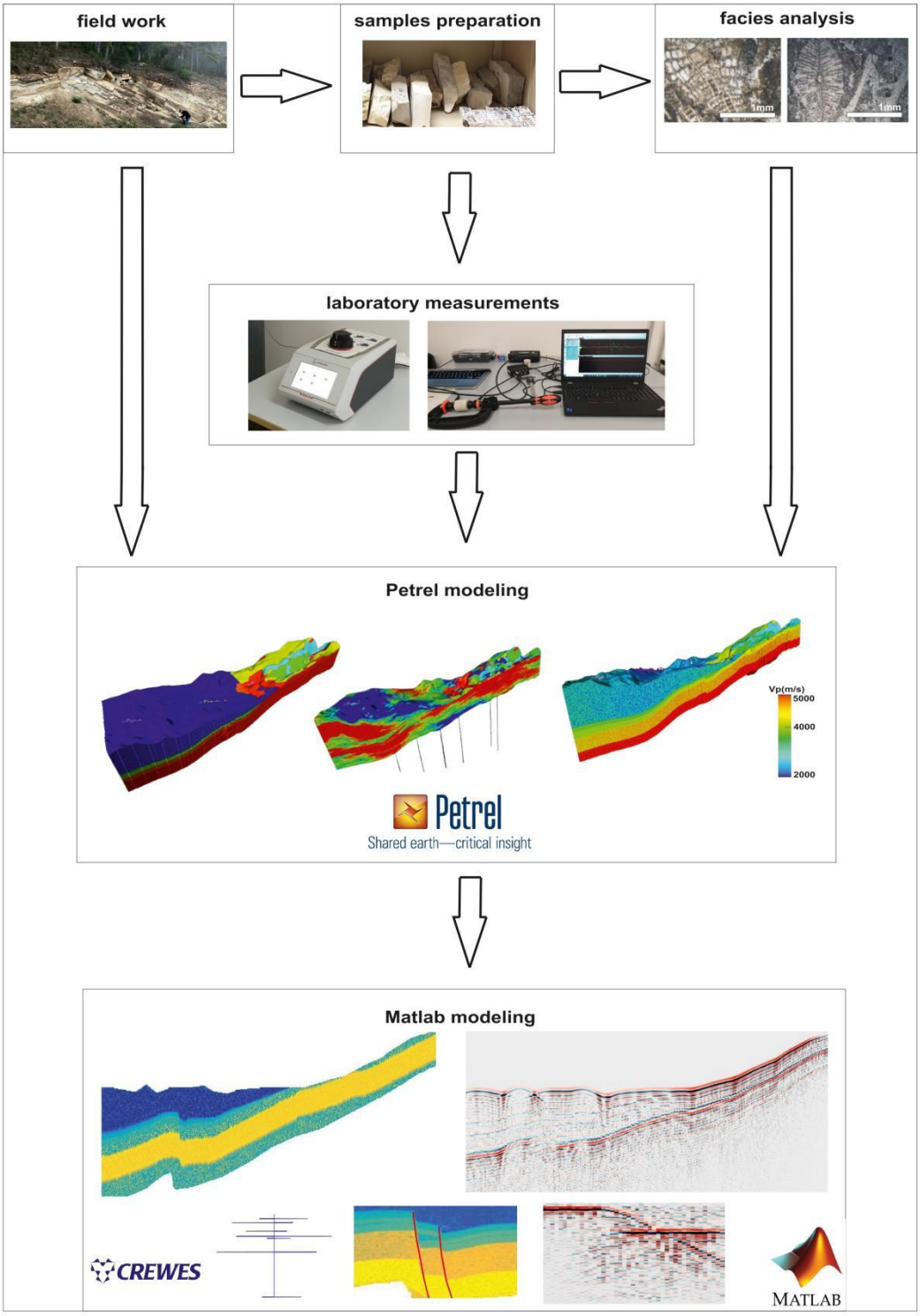

(Fig. I) Schematic workflow chart

Field work

First and foremost is the field work which involves the study and the sampling of lithologies. Sampling covered the Chattian Porto Badisco calcarenite outcropping in the Salento Peninsula, southernmost portion of the Apulian Carbonate Platform. On the Majella Massif, the northernmost portion of the Apulian Carbonate Platform the Campanian-Maastrichtian Orfento Formation, the Paleocene-Eocene Santo Spiritio Formation and the Oligo-Miocene Bolognano Formation were sampled. In the field, the faults developed in the lithologies of the Majella Massif were identified and their kinematic indicators and throws were observed. Field work also included the measurement of stratigraphic sections used as input data for the modelling exercise presented.

Facies analysis

After lithologies collection, samples are prepared for the analyses. In this work, a thin section was produced for each sample to perform facies analysis with a transmitted light microscope. Through the recognition of components, structures and textures constituting rocks it is possible to predict geometries, lateral extent and spatial distribution of sedimentary bodies, such as reservoirs (Catuneanu, 2006). Given its importance as qualitatively measurement of the system heterogeneity, a facies analysis exercise was performed in all three chapters of this thesis.

Laboratory measurements of petrophysical characteristics

Measurements of petrophysical characteristics are performed in laboratory to quantify facies and system heterogeneity.
Each sampled rock block is cut into square-based parallelepipeds with approximately 4 cm sides and approximately 5 cm height. Subsequently, samples are dried in an oven for 24h at 60°C to remove in-pores water.

Once dried, samples are analyzed with the AccuPyc II 1340 helium pycnometer from Micrometrics – with an accuracy of 0.05% and repeatability of 0.01 %. –, and with an Anton Paar Ultra-pyc 5000 helium pycnometer – with an accuracy of 0.02% and repeatability of 0.01 %. – in order to measure density and calculate porosity. The pycnometer diffuses helium (He) inside the pores of the sample. Helium small atomic radius allows for his penetration even in the smallest voids. According to this principle we can evaluate the volume of a rock, excluding the volume occupied by the pores.

We calculate the bulk density as the dry weight/volume ratio of the sample and. To evaluate the facies heterogeneity we calculate the grain density, the density of the rock components without the effect of porosity, as the weight/volume ratio of the matrix obtained pulverizing the samples. Being all the samples carbonate rocks the grain density remains constant while the bulk density values are distributed in a wide range highlighting the difference in density between facies. The connected porosity value for each sample is calculated by dividing the difference between the geometric volume of the sample – measured with a micrometer gauge – and the volume measured by pycnometer with the geometric volume. Porosity is also investigated in the first chapter with the point counting method on thin sections performed with JMicrovision software and with image analysis carried out with imageJ software described in detail in chapter one.

In addition to density and porosity, this workflow also includes the measurement of the seismic velocities of the samples, essential for modelling. P-wave velocity (Vp) and S-wave velocity (Vs) are measured by using the pulse-transmission technique (Wang et al., 1997). We use the USB 8M 8-channels multiplexed system ultrasonic device generator developed by Mistras Eurosonic. The device is connected with two 1 MHz piezoelectric transducers: one on the top of the sample for signal emission and another on the base of the sample for signal reception after waves propagation through the sample. The transducers are held in contact with the faces of the samples by placing them between the jaws of a bench clamp. Via the USB 8M device it is possible to control amplification, filtering and probe signal quantification. Signals of the waveforms are recorded and displayed by using the scanning imaging processes based on a Mistras Ultrasonic EuroscanV software. Using

this software, the first arrivals of the P and S-waves are analyzed and picked manually from the waveforms.
The petrophysical characterization methodology is applied to all samples collected to develop this work. In the first chapter it allows for the quantification of facies heterogeneity of the system for further modelling in Petrel (mark of Schlumberger). In the second- and third-chapters data obtained from laboratory measurements are used as input for 3D property modelling in Petrel in turn input for synthetic seismic forward modelling.

Petrel modelling

The widely used Petrel (mark of Schlumberger) software platform provides tools to solve complex structural and stratigraphic challenges. Within a single environment it is possible to perform stratigraphic and seismic interpretation in addition to fault, facies, and geo-cellular property modelling. Moreover, the developing of stratigraphic and structural 2D to 3D models populating the geo-cellular model with facies and petrophysical properties is possible using a range of deterministic and stochastic algorithms.
For the Porto Badisco calcarenite case study, Petrel is used to build a field-based detailed 3D model of facies association and distribution giving some clues to understand the high degree of facies heterogeneity. As first step the grid is built. Small cells dimensions – 8mx8mx0,2m (the 0,2m Z-dimension is equal to the thinnest geological object observed) – guarantee the reflection of the horizontal and vertical facies variation (Amour et al., 2012; Tomassetti et al., 2018). As a further step, topography from a digital earth model (DEM) with a resolution of 8m (as the X-Y cells size) – used as the top surface of the model grid – is imported. The bottom surface of the model grid is set at a 0 m a.s.l. as the lowest stratigraphic data. In order to populate the grid with the facies, the field-measured stratigraphic logs are imported into Petrel so cells constituting the grid model can be intersected by logs (Tomassetti et al., 2018). Since the stochastic approach results a suitable method to reproduce the facies heterogeneity of carbonates (Falivene et al., 2006) the Truncated Gaussian Simulation (TGSim) algorithm of Petrel is preferred. Geostatistical

parameters such as vertical and horizontal dimensions of facies distribution are obtained directly from field outcrop measurements (Tomassetti et al., 2018).

On the Majella Massif case study, a 3D Petrel model – where petrophysical characteristics of the sampled rocks are distributed – is exploited as input for forward synthetic seismic modelling. The 3D structural model building starts with the construction of a dense grid composed of 10x10x10m sized cells oriented parallel to the dip of the main tectonic structures. The topography is imported from a digital earth model (DEM) with a resolution of 10m. This surface constitutes the top surface of the model. The Upper Cretaceous, instead, represents the model bottom surface. Formation tops are then modeled using the well-tops data of the investigated formations (ViDEPI Project, 2012) and the thicknesses obtained from stratigraphic sections measured in the field. Consequently, six zones in the Petrophysical 3D model corresponding to the lithologies under study in Chapters 2 and 3 are defined. At this point, the process of cells populating started by assign the proper seismic velocities for each cell. Calculations from laboratory measurements and outcrops data allows for the creation of seven pseudo-wells logs with values sampled every 1m. Pseudo-wells are synthetic well log created in a location where no wells have been drilled but where logs have been calculated from other data such as nearby drilling, geophysical surveys, laboratory measurements and outcrops data. Upscaling from 2D to 3D values of measured petrophysical characteristics inserted in the pseudo-wells led to force the model in populating the cells with constrained data. Inside each of the six zones, the layering interval to horizontally distribute petrophysical characteristics – with thickness of 10 meters as the dimensions of the grid cells – is defined.

Petrophysical modelling is then performed through the Petrel property modelling tool to distribute the values of the measured characteristics such as seismic velocity in the volume using different geostatistical data interpolation algorithms. The algorithms used, all provided by Petrel property modelling tool are the User Defined algorithm, the “Sequential Gaussian Simulation”, the “Kriging" and a combination of the latter two, the “Sequential Gaussian Simulation Co-Kriging”. The petrophysical zones are firstly populated with the

User Defined algorithm (UD) customized by the operator. Variables derive from laboratory measurements, and they provide constant velocity values for each zone by averaging the measured seismic velocity values. To simulate a heterogeneous distribution of velocities through the model, cells are populated using the “Sequential Gaussian Simulation (SGS)” algorithm. This stochastic method produces a range of uncertainty of a variable causing local changes and randomization in the distribution of properties (Journel and Ying, 2001). As expected, it will be shown that SGS stochastic algorithm gives a more realistic random distribution of the seismic velocity if compared to the UD algorithm approach, but the lateral continuity of horizons is not preserved. Therefore, it became necessary to use other interpolation algorithms to distribute the properties of the rocks in the model.

The “Kriging (KG)" algorithm has been chosen. It has a deterministic approach which results in a preserved continuity of the strata with respect to SGS. However, as for the same context modeled at a smaller scale by Trippetta et al., 2021, it led to an excessive smooth of the values populating most of the cells with the mean seismic velocity value due to its deterministic approach (Dubrule, 1998; Chambers et al., 2000, Trippetta et al., 2021).

To preserve the strata continuity and to achieve the minimum variance of error in modelling, but also to avoid an excessive smoothing (Vo Thanh and Lee, 2021), “SGS Co-Kriging (SGS-CK)” algorithm has been then used. This algorithm employs data from correlated variables to improve the estimation of all variables (Myers 1984). Whit SGS-CK it is possible to insert a second interpolation variable (Manthena et al., 2009; Esmaeilzadeh et al., 2013). As second variable, the constant interval velocity values of the previously created 3D model with the UD algorithm is inserted. This second variable is distributed through the model with the “normal score transformed method” using a 0.8% percentage variance. SGS-CK algorithm satisfactory represents the heterogeneous distribution of seismic velocity within the 3D volume maintaining at the same time the lateral continuity of the zones. Consequently, it results to be the best algorithm present in the property modelling tool of Petrel to represent the heterogeneity of the system.

The last step of modelling in Petrel is the 2D section generation which is used as input data to run synthetic seismic in Matlab (mark of Mathworks). Thanks

to Petrel calculator tool it is possible to generate a section parallel to a volume grid axis using the following equation:

$$S = If\ (x = n, Property) \quad (I)$$

where n is the value of x (grid axis) along which was cut the section. The section is, then, converted into points reflecting the values of a single grid cell. Thus, every point is characterized by three values representing the horizontal distance (x), the depth (z) and the property distributed. Consequently, the points are extracted as a spreadsheet, and they are imported into Matlab. There, the extracted spreadsheet is converted in a seismic velocity values matrix used as velocity model needed to run the synthetic seismic section (De Franco et al., 2019).

Matlab modelling

Modelling in Matlab is applied in the second and third chapters of this thesis to pursue the goal of producing synthetic seismic models.

1D seismic models are usually performed to predict the seismic response and to investigate the link between the geological beds and reflection seismic data (Alaei, 2012). Synthetic seismic forward modelling starts with a 1D model carried out in Matlab. To highlight the seismic response of the lithologies, a synthetic seismic trace – with layers characterized by variable thicknesses, densities and seismic velocities – was performed. Thus I wrote a simple script (Appendix A) in which it is possible to calculate the acoustic impedances (AI), the reflection coefficients (RC), the two-way travel times (TWT). The script allows the convolution of a waveform with the reflectivity series obtaining a synthetic 1D seismogram.

It is, then possible to calculate the acoustic impedances (AI) for each layer by using:

$$AI_{(i)}=[\rho_{(i)}V_{(i)}] \quad (II)$$

Where ρ is the density and V is the seismic velocity of P-waves of each lithology; i is the number of the layer.
Thus, the reflection coefficient (RC) for each layer is calculated through the normal incidence formula:

$$RC_{(i)} = [AI_{(i+1)} - AI_{(i)}] / [AI_{(i+1)} + AI_{(i)}]; \quad \text{(III)}$$

The two-way travel time (TWT) is finally computed:

$$TWT_{(i)} = 2 \sum_{i=1}^{n} (L_{(i)} / V_{(i)}) \quad \text{(IV)}$$

Where n is the total number of layers, L represents the layer thicknesses and V is the seismic velocity (Vp) of the layer i.
A sampling interval of 0,002 seconds and a zero-phase Ricker wavelet with 40Hz frequency is set. The sampling frequency and interval have been chosen to have a good compromise between depth penetration and resolution without incurring in aliasing phenomena. Through the convolution of the wavelet with the RC values and the reflectivity series, a synthetic 1D seismogram is obtained.
In Chapter 2 the influence of hydrocarbon is evaluated. The 1D synthetic seismic trace is obtained starting from velocity values measured on both clean and bitumen-saturated samples. Results are then compared.
However when the velocity distribution is laterally heterogeneous, 1D model errors can have significant consequences on the reliability of the resulting velocity distribution, that's why we proceeded with a 2D approach.
The last workflow step is the 2D synthetic seismic forward modelling. There are many approaches to seismic modeling classified by Carcione et al., 2002 into three main categories: direct methods, integral-equation methods, and ray-tracing methods.
In this work we decide to solve the wave equation using direct methods, in which the geological model is approximated by a numerical mesh discretized in a finite numbers of points. In these techniques called finite difference time domain methods, but also called grid methods and full-wave equation methods, the solution of the wave equation gives the full wavefield (Carcione et al., 2002).

We used finite difference time domain methods because are more convenient for a situation of the subsurface of the Majella area where a dense grid is required for physical reasons such as fine layering and heterogeneities.
Finite difference time domain methods do not have restrictions on the material variability and are accurate if the grid used is composed
by sufficiently fine sized cells. With these methods is possible to assign different acoustic properties to every grid point simulating complex subsurface models. The technique is well suited for the production of seismic images useful in the interpretation of the results. A limt of these methods is that they can be more time-expensive than the other methods (Carcione et al., 2002). This modelling method is performed in Matlab with the CREWES (Consortium for Research in Elastic Wave Exploration Seismology) toolbox. The CREWES consortium proposes several numerical methods for exploratory seismology with algorithms including the finite difference modelling for exploding reflectors. The finite difference time domain method is a numerical method applicable to structurally complex media (Moczo et al., 2007). It differs from ray tracing method where significant amount of power scattered from the surfaces is not considered (Wang et al., 2002). Instead, the finite difference time domain method calculates the total wave field. The function script *afd_explode* is chosen. It uses an input velocity matrix characterized by 10x10m sized cells used as velocity model to calculate the exploding reflector directly from the velocity model if it is assumed a normal incidence reflectivity (Margrave and Lamoureux, 2019). This velocity model into *afd_explode* creates an exploding reflector seismogram by inserting the correct variables in the script. Variables are the input velocity matrix, the sample interval, the size of time step for modelling, the maximum time of the seismograms, the positions receivers in x and z, the wavelet frequency and a laplacian approximation which is an operator used in the finite difference method to have a discretization of the grid points with neighbor points (Patra and Karttunen, 2006; Margrave and Lamoureux, 2019). For the modelling exercise shown in this thesis, the first variable inserted was the velocity matrix represented by the sections extracted from Petrel, considering both constant interval velocities and heterogeneous velocities matrix. Sample interval was set at 2ms and the size of time step for modelling was imposed equal to 0,5ms. The maximum time of the

seismograms was cut at 2,5sec depth. After performing a sensitivity test on frequencies equal to 10Hz, 20Hz, 40Hz, 80Hz, 100Hz, 200Hz the 40Hz frequency wavelet results the best compromise between resolution and signal penetration at depth. A nine-point laplacian approximation was adopted (Cho et al., 2007). At this point, it has been possible to run the output seismogram performing the convolution between AI and RC with a zero-phase Ricker wavelet resulting in a synthetic seismic stack section (De Franco et al., 2019).
Comparisons of seismic outputs are carried out to evaluate the influence of facies heterogeneity and to identify the influence of hydrocarbons presence on the seismic response. Thus, a first comparison between the 2D synthetic seismic stack section – generated from the constant interval velocity model – with the 2D synthetic seismic stack section – produced by the heterogeneous velocity model – is made. A second comparison is carried out between the latter and the synthetic seismic stack section generated using velocities measured on bitumen-saturated rocks.
To ascertain the influence of the presence of faults in the seismic response, in the third chapter seismic velocities of the fault zone were modified before running the forward modelling. Seismic velocities of rocks less than 50 meters far from the fault were increased or decreased using Matlab *roipoly* command in the velocity matrix exported previously from Petrel. *Roipoly* allows to specify polygonal region of interest creating an interactive polygon tool associated with the velocity matrix displayed. *Roipoly* returns a mask as a binary image, setting pixels inside the polygonal region of interest to 1 and pixels outside to 0. Adding the desired velocity value to the *roipoly* output a mask with the required value to be added to the velocity matrix is produced.
Once created the two velocity models the synthetic seismic was run with the *afd_explode* script of CREWES to obtain two different seismic responses to be compared. A 100m wide and a 50m wide fault zones were created with the *roipoly* command. Since the seismic response did not show substantial differences, only the one closest to the realistic size of a fault zone (the 50m width) is discussed in Chapter 3.

Chapter 1: Modelling lateral facies heterogeneity of a carbonate ramp. Petrophysical characteristics of an Oligocene carbonate platform (Salento, southern Italy)

1.1 Outcrop-based facies modelling and heterogeneity quantification: from the field to laboratory to software models.

This study focuses on the Chattian Porto Badisco Calcarenite carbonate ramp outcropping in the Salento peninsula. In this work continuous exposures of outcrops allow observations and insights offering the opportunity to build 2D petrophysical models and detailed 3D model of facies association and distribution. Field work measurement and facies recognition together with sampling allow to reconstruct the depositional model. Once field-data are obtained, it is possible to perform the digital modelling of the facies variation in space. From the samples collected it is possible to evaluate facies heterogeneity through the observation of components constituting the rocks performing the facies analysis. To have a quantitative evaluation of the facies heterogeneity petrophysical characterization measurements are performed. Density, porosity and seismic velocity measured in this work are expressed in a wide range of values. In order to ascertain the distribution of petrophysical features reflecting facies heterogeneity along the depositional model, 2D models were produced on the distribution of porosity and P-wave seismic velocity. Outcrop 3D modelling is validated by the comparison with field data confirming that field-based models are crucial in understanding sedimentary geometries and providing some clues to understand the high degree of facies heterogeneity in carbonate systems (Tomassetti et al., 2018; Jafarian et al., 2018).

Therefore, this study can contribute to fill the gap for the building of realistic 3D geological models of the carbonate ramp systems and to link the sedimentological and petrophysical properties retrieved from outcrop studies.

1.2 Geological setting

The case study is from the southern portion of the Apulian carbonate platform (ACP), in the Salento peninsula and corresponds to the Porto Badisco calcarenite (Fig.1.1). The ACP is an extensive carbonate platform that has set and developed along the southern margin of the Tethys Ocean since the Mesozoic (Bernoulli, 1972, 2001; D'Argenio, 1976; Bosellini, 2004). It extends from southeastern Abruzzi, with the Majella Massif representing the northernmost portion of the ACP, through Apulia and the Adriatic (Zappaterra, 1994; Eberli et al., 1993; Bosellini, 2002, 2004). From the Upper Triassic to the Upper Cretaceous a massive carbonate platform, the ACP, developed on the Adria plate (Ricchetti et al., 1992). The carbonate production shifts to the platform margins between the Paleogene and Middle Miocene in carbonate ramp depositional environments and in this context the Chattian Porto Badisco calcarenite has developed (Bosellini et al., 1999). Porto Badisco calcarenite (Upper Chattian) is a bioclastic calcarenite which have a maximum thickness of about 60 meters. Sedimentary structures often occur as ghosts as they are deleted due to bioturbation. Facies variations are most recognizable by the rapid change in components. The major calcium carbonate producers are the large benthic foraminifera with a large contribution from red algae and from small colonies of corals arranged in several mounds a few meters high (Pomar et al. 2014).

In Porto Badisco a drainage channel produced through erosion a ravine with excellent exposure of the outcrops where it is possible to perform sampling and stratigraphic logs measurements (Fig.1.1).

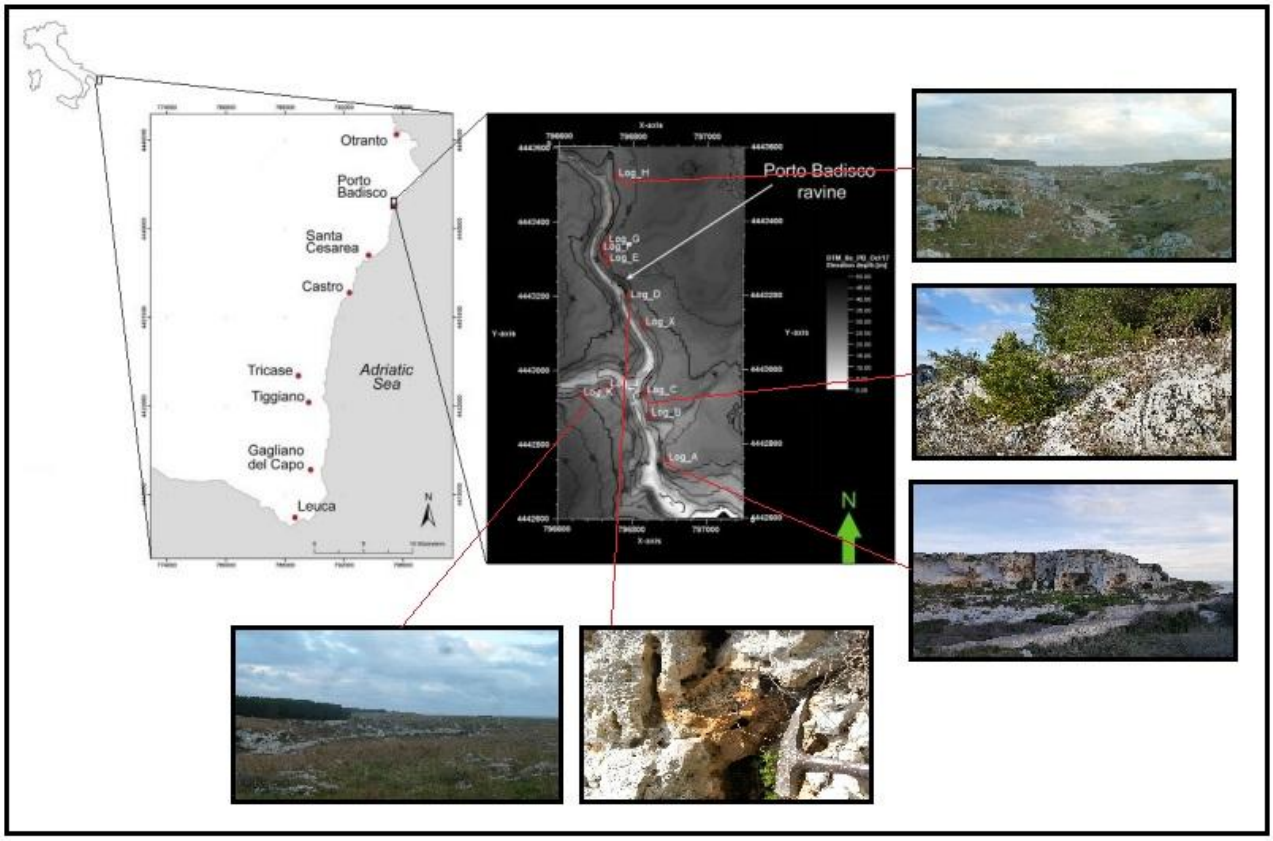

Fig.1.1. Location of the southern portion of the Salento Peninsula where the study area is located. Porto Badisco area digital elevation model (DEM with horizontal resolution of 8 m) with the Porto Badisco ravine. The location of the eleven measured stratigraphic field logs are represented with red dots (modified after Tomassetti et al., 2018). View of some of the outcrops from which the samples were collected.

1.3 Methods

1.3.1 Field data acquisition

Eleven stratigraphic logs have been measured in the Porto Badisco ravine. They are correlated one to each other thanks to three key horizons throughout the study area. Nine logs are parallel to the depositional dip direction of the strata (Fig. 1.2-A), along the margin of the N-S oriented Porto Badisco ravine, instead two logs are perpendicular to the depositional dip direction E-W oriented (Fig. 1.2-B). The Porto Badisco Calcarenite shows sub-horizontal beds with dip azimuth of 150°. All the six facies defined by Pomar et al. (2014) are recognized and sampled in the study area. Over 100 samples were collected, from the bottom to the top of each stratigraphic log, with an average sampling rate of one meter at each facies switch.

1.3.2 Thin sections analysis

From the sampling of the facies, 108 thin sections are obtained and analyzed with an optical microscope for the determination of textures, cements and the identification of the skeletal components that distinguish the facies and their depositional environments. The classification of the facies is based on Dunham (1962) and Embry & Klovan (1971).
A quantitative analysis is carried out on the thin sections to estimate the facies porosity. This analysis uses the point counting method in order to identify the frequencies of the main components in the different samples. For a porosity analysis, three components are counted: granules, pores and cement. To reach a statistical significance 500 random points are counted using JMicroVision software for each thin section. The random path has been adopted, excluding other point counting techniques that consider grain size and/or grain packing, since facies are very different from each other with different grain sizes and with different relations between the grains, so porosity is expressed through the samples in a random way without following preferential distributions.

1.3.3 Image analysis

Using ImageJ software, slab scans of samples are analyzed to obtain further feedback on the percentage of porosity. Based on the color contrast between pore and matrix it is possible to analyze the color curves. By setting the image in binary 8bit BW format the software allows to calculate the percentage of black (pores) or white (matrix). Plotting the percentage of white pixels vs. the percentage of black pixels on a frequency histogram it is possible to achieve an estimation of porosity. Also for this methodology, as for the point counting on thin sections, porosity is measured only in 2D, however the image area is notably larger being about 10 times the dimensions of a typical thin section.

1.3.4 Pycnometer measures of density and porosity

Density and porosity are measured using AccuPyc II 1340 helium pycnometer from Micrometrics. Bulk and grain density are quantified. The connected

porosity is then calculated by dividing the difference between the geometric volume of the sample and the volume measured by pycnometer with the geometric volume (Ruggieri and Trippetta, 2020; Trippetta et al., 2020).

1.3.5 Seismic velocity

P-wave velocity (Vp) and S-wave velocity (Vs) are measured axially on the samples by using the pulse-transmission technique (Birch, 1961, 1960; Wang, 1997). A 900-mV pulse generator is used to excite a 1 MHz frequency piezoelectric transmitting transducer. The resulting waveforms are recorded using a receiving transducer. After preamplification, signals are recorded and displayed on a digital oscilloscope. Consequently first arrivals of P and S waves are picked manually from the waveforms (Trippetta and Geremia 2019).

1.3.6 Software modelling

Laboratory measurements allow to build two petrophysical models of the depositional architecture of the Porto Badisco Calcarenite object of this study. Modeling of 2D porosity and P-wave velocity were performed through the correlation of the nine logs parallel to the depositional dip direction of the carbonate ramp thanks to the clear presence of three key horizons observable in the field. The N-S orientation of these models runs parallel to the dip of the depositional system. In grayscale were represented the average porosities measured through the samples and in shadow of red the ranges of the P-wave velocities.

The distribution of petrophysical features was conditioned on the facies distribution of the Porto Badisco ramp and consequently the resulting models are linked to facies heterogeneity.

The 3D facies model of the Porto Badisco Calcarenite is built in Petrel (mark of Schlumberger) as illustrated in the following steps.

Topography is imported from a digital earth model (DEM) with a resolution of 8m as the top surface of the model grid. The bottom surface of the model grid is set at a 0 m a.s.l. as the lowest stratigraphic log data. The maximum vertical

thickness of the model is imposed to 43 m (Tomassetti et al., 2018). The XY cells dimensions is equal to the DEM resolution (8 × 8m). In the Z-dimension, the thinnest geological object observed is a bed about 0.40 m thick so the vertical dimension of the cell is set about 0.20 m because the cells dimension must be small enough to reflect the horizontal and vertical facies variation (Amour et al., 2012; Tomassetti et al., 2018). Layers represented by stratigraphic surfaces are built to complete the grid. In order to populate the grid with the facies, the measured stratigraphic logs are georeferenced and imported into Petrel, in this way cells constituting the grid model are intersected by logs (Tomassetti et al., 2018). Stratigraphic logs were used to give an input to the model on the facies distribution data at observed field locations. Once stratigraphic logs were upscaled intersecting the geocellular model, they were used to constrain the modeling algorithm and thus to create a realistic 3D facies model for the Porto Badisco carbonate ramp. The stochastic approach is the most suitable method to reproduce the facies heterogeneity of carbonates (Falivene et al., 2006) so the Truncated Gaussian Simulation (TGSim) algorithm of Petrel is chosen. To reproduce facies heterogeneity, geostatistical parameters such as vertical and horizontal dimensions of facies distribution are obtained directly from field outcrop measurements (Tomassetti et al., 2018).

1.4 Results

1.4.1 Field data acquisition

Stratigraphic log measurements resulted in correlation panels of facies, in their stratigraphic relationships and in their petrophysical characteristics (Fig.1.2). Data obtained from measured stratigraphic logs makes modelling in Petrel possible. The stratigraphic logs measured in dip direction with respect to depositional profile, with a N-S orientation, (Fig.1.2A) show all the six recognized facies that alternate abruptly along the depositional profile. Logs A, B, C, and X are characterized by the presence of an alternation of more distal facies ranging from the mesophotic zone of the middle ramp settings to the

distal ramp settings. Facies proximal to the shoreline, set in the photic zone of the inner ramp are most abundant in logs E, F, G, and H. Both proximal and distal facies are present in log D demonstrating that heterogeneity is rapidly expressed in a relatively small space. The stratigraphic logs measured in strike direction in the field with respect to depositional profile, with a E-W orientation, (Fig.1.2B) show three of the six recognized facies. Intermediate and distal facies are present in logs C and J, while log K is the one in which distal facies are more abundant than in all measured and sampled logs. The details of the recognized facies are discussed in the next paragraph. In the correlation between the logs is represented with a black dashed line the most continuous of the three key horizons visible along the entire Porto Badisco ravine.

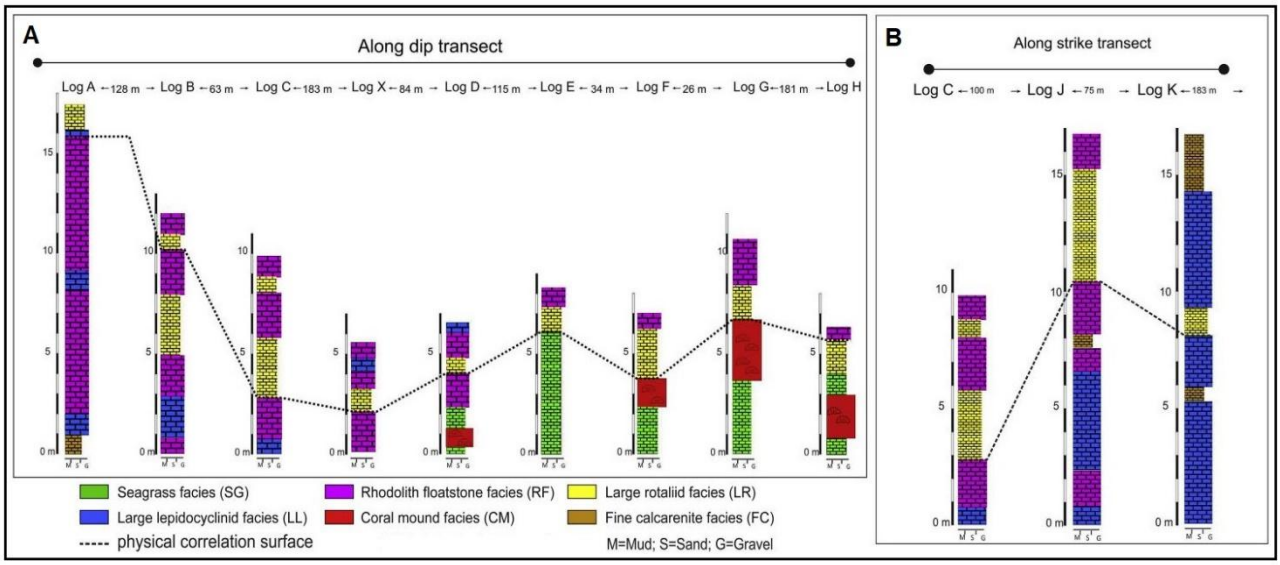

Fig.1.2. A) Stratigraphic logs measured in dip direction in the field showing the six recognized facies; B) Stratigraphic logs measured in strike direction in the field showing three of the six recognized facies. For location of logs see Fig. 1.1. (modified after Tomassetti et al., 2018).

1.4.2 Thin sections analysis

The six facies of the Porto Badisco Calcarenite (Fig.1.3) – defined by Pomar et al. (2014) – are recognized: small benthic foraminifer wackestone-

packstone (SG), coral mounds (CM), large rotalid packstone (LR), rhodolithic floatstone (RF), large lepidocyclinid packstone (LL) and fine calcarenite (FC).

1.4.2.1 Small benthic foraminifer wackestone-packstone (SG)

It is a wackestone-packstone rich in foraminifera and red algae fragments and a minor amount of articulated red algae, fragments of bryozoans and corals. Large porcellanaceous species as Sorites and Austrotrillina and large rotalids including Neorotalia are frequent among the foraminifers. Spiroclypeus, Nephrolepidina and Amphistegina are often present as reworked fragments. Among the smaller taxa miliolides, the textularids and rotalids are abundant.

1.4.2.2 Coral mounds (CM)

Colonies of corals, often in physiological position, create mounds from 2 to over 10 meters high. Beside them, overturned colonies and metric rudstones of fragments of them are often present. The major components of this facies are coral fragments and large benthic foraminifera usually in fragments including nummulitids and large rotalids such as Neorotalia. Porcellanaceous shell miliolids are also present among the foraminifera. Fragments and encrustations of non-articulate red algae such as mastoforoids or Sporolithon are also common. In addition to the components above mentioned, there may also be fragments of brachiopods, bivalves and articulated red algae.

1.4.2.3 Large rotalid packstone (LR)

Common components of this facies are fragments of large rotalids such as Neorotalia, Nummulitids, Operculina and Heterostegina, together with fragments of Nephrolepidina and Amphistegina. Porcellanaceous shell foraminifera and smaller taxa including abundant miliolides can contribute in carbonate construction. Non-articulate red algae in this facies include melobesioids, mastoforoids and Sporolithon. Fragments of echinoderms and bivalves are also common.

1.4.2.4 Rhodolithic floatstone (RF)

The aggregates of subrounded red algae formed by transport down the slope, the rhodolites, that characterize this facies are predominantly in laminar structure, produced by Mesophyllum, Sporolithon, and Lithothamnion. The matrix is a packstone with many rotalids, Eulepidina, nummulitides, Neorotalia, Nephrolepidina, Amphistegina and rare fragments of Miogypsinoides. Bryozoans and fragments of echinids, rare bivalves, decapods and brachiopods are frequent.

1.4.2.5 Large lepidocyclinid packstone (LL)

This facies is characterized by a packstone-grainstone rich in very large lepidocylcinids such as Eulepidina and Nephrolepidina. In addition to the lepidocyclinids rotalids, abundant nummulitids and well conserved Amphistegina, Neorotalia are present. Encrusting and planktonic foraminifers also contribute. In addition to foraminifera, non-articulate red algae, sometimes forming rhodolites can be observed.

1.4.2.6 Fine calcarenite (FC)

This calcarenite is a fine bioclastic packstone to wackestone with well sorted and eroded fragments. Reworked red algae followed by plates of echinids, large rotalids and small benthic foraminifera are dominant. Among the large benthic foraminifera reworked fragments of Miogypsinoides, Neorotalia, lepidocyclinids, nummulitids, and amphisteginae figure.

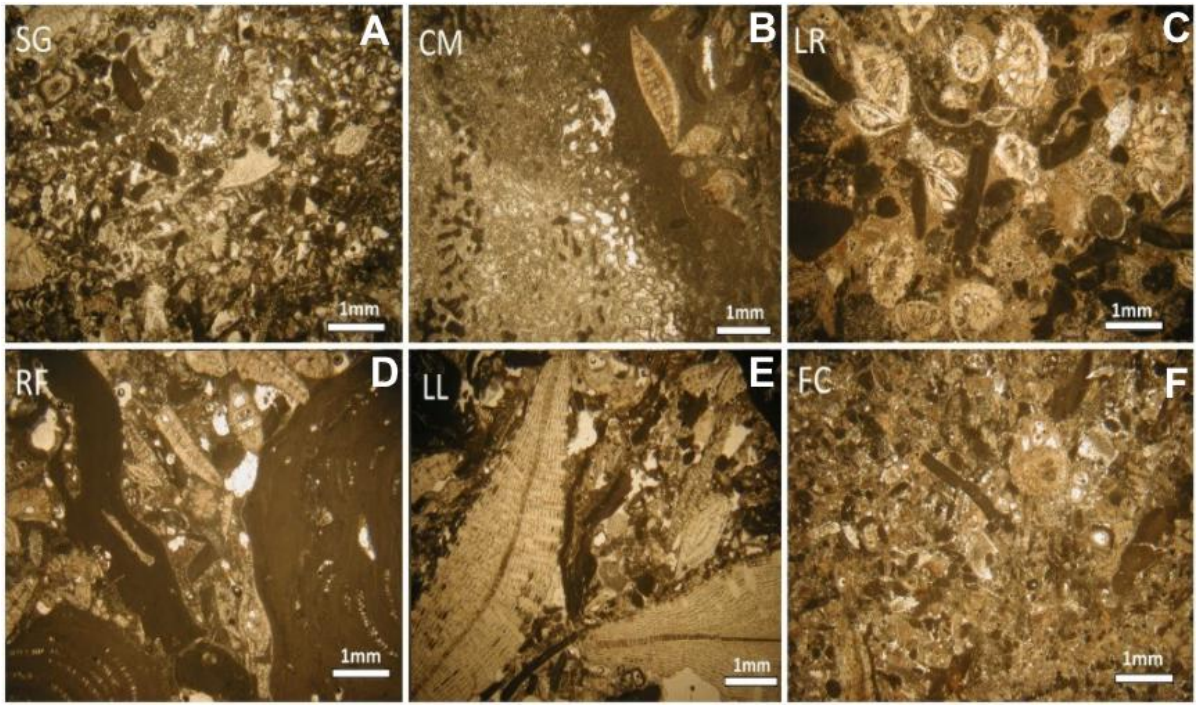

Fig. 1.3. Sampled facies in thin section: A) Small benthic foraminifer wackestone-packstone (SG); B) Coral mounds (CM); C) Large rotalid packstone (LR); D) Rhodolithic floatstone (RF); E) Large lepidocyclinid packstone (LL); F) Fine calcarenite (FC). Scale bar = 1 mm.

1.4.3 Petrophysics

1.4.3.1 Density

The density data obtained with the pycnometer show (in Tab.1.1) stable results especially for Grain density. Calculated values of grain density are constantly around 2700 kg/m^3. More variability is shown by the values of Bulk density ranging from a minimum of about 1700 kg/m^3 measured for the LL facies to a maximum of over 2500 kg/m^3 for the CM facies. Standard deviations (2σ) range from a minimum of 0.0372 g/cm^3 for the SG facies to a maximum of 0.077 g/cm^3 for the LL facies.

Facies	Bulk Density kg/m^3	Grain Density kg/m^3
SG	2390	2750
CM	2530	2750
LR	2230	2750
RF	2110	2730
LL	1710	2740
FC	1930	2730

Tab.1.1. Bulk, core and grain density values (expressed in kg/m^3) of the facies characterized obtained with the helium pycnometer.

1.4.3.2 Porosity

Porosity results measured with the helium pycnometer show total porosities of the samples range in value from 7,8% for the CM facies to over 38% for the LL facies. The effective porosities are equal to the total porosities for the LR, RF, LL, and FC. The effective porosities of the SG and CM facies, 12,11% and 5,8% respectively, are lower than the total porosities revealing a non-connected porosity of 0,88% for the SG facies and 2% for the CM facies respectively. Standard deviations (2σ) range from a minimum of 0,0006% for the FC facies to a maximum of 0,0049% for the CM facies.

Results obtained through point counting on thin sections are critically lower. With this methodology a maximum porosity of 19,72% was measured for the LL facies and a minimum of 5,6% for the SG facies. Porosity values relative to the other facies are 6,4% for the sample referred to CM, 15% for the sample referred to LR, about 7,6% for RF and FC facies.

Porosities derived from image analyses are slightly lower with respect to those obtained by the pycnometer. A porosity of 17,09% was measured for the SG facies, whilst the porosity for the CM sample is 6,84%, the lowest measured among all methodologies. LR facies is characterized by a porosity of 20,73%. The RF facies shows a porosity of 30,40%. The LL facies results the most

porous for all the methodologies with a value of 37,49%. The FC sample is characterized by a total porosity value of around 25,35%. For almost all the the effective porosity represents most of the porosity being total porosity very similar with respect to effective porosity (Tab 1.2).

Facies	ϕ tot. % (pycnometer)	ϕ eff. % (pycnometer)	ϕ % (point counting)	ϕ % (image analysis)
SG	12,99	12,11	5,6	17,09
CM	7,8	5,8	6,4	6,84
LR	18,8	18,8	15	20,73
RF	30,42	30,42	7,6	30,4
LL	38,12	38,12	19,72	34,6
FC	30,32	30,32	7,8	25,35

Tab.1.2. Porosity values (expressed in %) of the facies characterized obtained with the helium pycnometer, point counting and image analysis. Total and effective porosity are relative to the helium pycnometer measurements.

1.4.3.3 Seismic velocity

Measured P and S waves and Vp/Vs ratio of the analyzed facies are reported in Tab.1.3.

The velocities of the longitudinal elastic waves (Vp) through the samples have been measured in a range of values from a minimum of about 3644 m/s of the LL facies up to 5573 m/s measured for CM whilst Vs range from 1911 m/s of FC to 3097 m/s for CM. The Vp/Vs ratio spans from 1,8 calculated for CM facies to 1,97 for RF facies.

Facies	Vp m/s	Vs m/s	Vp/Vs
SG	5183	2718	1,91
CM	5573	3097	1,8
LR	4599	2393	1,92
RF	4395	2234	1,97
LL	3644	1940	1,87
FC	3663	1911	1,91

Tab1.3. Seismic velocity of P and S waves values (expressed in m/s) and Vp/Vs ratio of the facies characterized.

1.4.4 Modelling

N-S oriented 2D petrophysical models built along the dip of the depositional model show that middle ramp facies (LR, RF, LL) have relatively high porosity and lower values of seismic wave velocity. The inner ramp facies (SG, CM), interfingered with the middle ramp facies, show lower porosity values and higher P-wave velocity than the middle ramp lithofacies.

Both 2D models show that facies heterogeneity controlled the distribution of petrophysical values.

In the construction of the 3D facies model TGSim stochastic algorithm of Petrel allows to model the facies heterogeneity characterizing the Porto Badisco carbonate ramp (Tomassetti et al., 2018). By imposing constraints in the input data, Walther's law is adequately respected in the interfingering facies along the carbonate ramp (Matheron et al., 1987). Constraints input data consist of field-measured logs that define the frequency of occurrence of facies, their stacking patterns and their thicknesses in the model. From the comparison between the measured logs and the model, the thicknesses and the lateral relationships of the facies are faithfully respected with the application of the algorithm TGSim (Tomassetti et al., 2018). The adequacy of the algorithm is confirmed by the possibility to recognize and compare the

facies belts of the Porto Badisco Calcarenite as described by Pomar et al. (2014). In the shallow water-inner ramp sectors of the 3D facies model the wackestone-packstone of small benthic foraminifera (SG) overlaps and interdigitates with the zone of coral mounds (CM), surrounded by a large rotalid packstone (LR). Proceeding toward the basin in a deeper zone of the 3D facies model there are the rhodolithic floatstone and then the large lepidocyclinid packstone-rudstone (LL) facies. The most distal facies both in the model and in the depositional profile is represented by a fine calcarenite (FC) (Pomar et al., 2014; Tomassetti et al., 2018).

1.5 Discussion

1.5.1 Thin sections and Facies

The Porto Badisco calcarenite exhibits a complex distribution of facies from innermost shallow-water facies, proceeding to distal facies characterized by aphotic conditions of deeper waters (Pomar et al., 2014). The interpretation of the facies is crucial in tracing the depositional environment, both in terms of bathymetry, hydrodynamic energy and in terms of photic zonation together with the biota that control the carbonate sedimentation. From the reconstruction of the depositional context of each facies a depositional model can be outlined.

1.5.1.1 Small benthic foraminifer wackestone-packstone (SG)

The presence of porcellanaceous foraminifera is indicative of euphotic conditions in a vegetated seagrass meadow area. Sediments trapped in the seagrass rhizomes create the heterogeneous texture with good matrix percentage. Well-preserved amphisteginae and articulated red algae confirm a shallow water environment. The large rotalids, nummulitids, Neorotalia, Spiroclypeus, and lepidocyclinids such as Nephrolepidina, lived more plausibly sheltered by a dense leaf canopy of the seagrass, in areas with mesophotic conditions, rather than at greater depths (Pomar et al. 2014).

1.5.1.2 Coral mounds (CM)

In an area with bathymetries greater than that characterizing the SG facies there are the photic and hydrodynamic conditions for the development of colonies of corals. The corals arranged in small mounds, do not form a rigid structure as a framework resistant to wave motion and elevated to the sea surface, creating cluster reef type structures and not a true frame reef. Small benthic foraminifera, such as miliolides and cibicids, and porcelain fragments are allochthons clasts derived from the seagrass. In situ sediments are represented by fragments of Nephrolepidina, nummulitids, and fragments of corals reworked during storm events or otherwise high energy events. They precipitate onto the flanks of the mounds, where the abundance of fine muddy matrix is an evidence that coral mounds are located below the wave action limit (Pomar et al., 2014).

1.5.1.3 Large rotalid packstone (LR)

This facies is characterized by the presence of both autochthonous components such as nummulitids and Nephrolepidina, and allochthons components deriving from shallower facies (CM and SG) such as Neorotalia, Amphistegina and miliolids. Moving towards greater bathymetries the presence of large rotalids, flattened nummulitids and non-articulated red algae increases. The associations of red algae such as mastoforoidea and the deeper melobesiodeae confirm meso-oligophotic conditions. Large fragmented rotalids indicate the presence of hydrodynamic energy. (Pomar et al., 2014).

1.5.1.4 Rhodolithic floatstone (RF)

This facies suggests deposition within the oligophotic zone characterized by the presence of red algae as mastoforoidee and melobesioidee with a predominantly laminar structure. The mastoforoideae are found in the innermost portion of the oligophotic zone and the melobesioideae in the most distal portion forming some encrustations. This demonstrates that transport has occurred from mesophotic conditions, colonized by mastophoridae, to

oligophotic conditions, where instead melobesioidea dominate. Sediment associated with seagrass and transported at depth is still present. Rolling along the slope profile the red algae often form rounded aggregates called rhodoliths. Oligophotic conditions are also confirmed by the appearance of flat and thin forms of Eulepidine (Pomar et al., 2014, Brandano et al., 2010).

1.5.1.5 Large lepidocyclinid packstone (LL)

In the more distal portions of the oligophotic zone, beyond the rhodolith facies, large and flattened Eulepidines appear. Conditions of greater depth are confirmed by the presence of planktonic foraminifera. Allochthonous components coming from the seagrass are miliolids, Amphistegina and Neorotalia. Other present foraminifera dwellers in the seagrass are nummulitids and Nephrolepidina. The decrease in mud limestone demonstrates some hydrodynamic energy (Pomar et al., 2014).

1.5.1.6 Fine calcarenite (FC)

This facies have components both associated with the euphotic zone, such as Amphistegina, Neorotalia, Miogypsina, small epiphytic taxa that proliferate in the seagrass area, and associated with the oligophotic zone characterized by flat nummulitids and large lepidocyclinids. This fine bioclastic deposit represents the distal accumulation of allochthonous components from shallower ramp sections in a zone of low carbonate production in dysphotic or aphotic conditions (Pomar et al., 2014).

1.5.1.7 Depositional model

The depositional model of the Porto Badisco calcarenite is represented by a homoclinal carbonate ramp characterized by an internal, intermediate and distal zone with homogeneous carbonate production along the entire depositional profile (Fig.1.4). The inner ramp zone, within the euphotic zone is characterized by the SG, LR, and CM facies. Moving towards the intermediate ramp, within the oligophotic zone, there is deposition of the RF and LL facies. the outer ramp is characterized by the FC facies (Pomar et al., 2014).

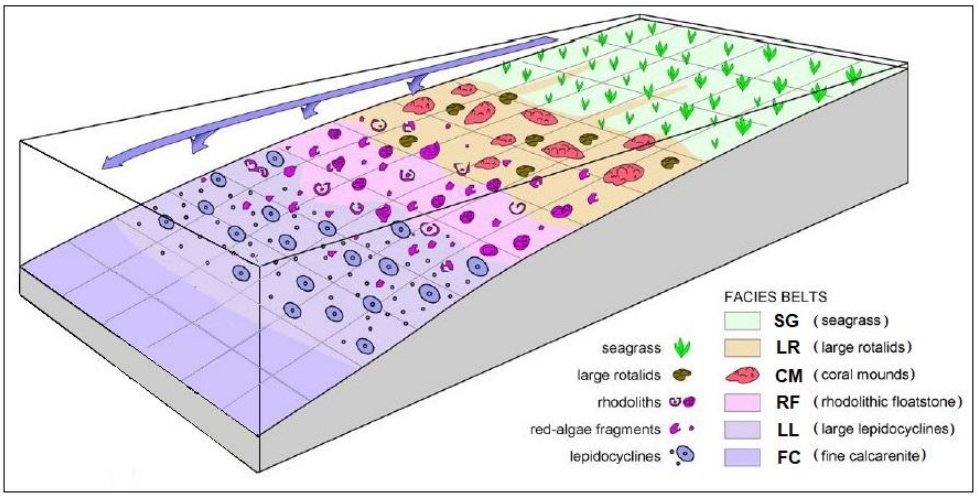

Fig. 1.4. Simplified depositional model of the Chattian Porto Badisco calcarenite carbonate ramp (modified after Pomar et al., 2014).

1.5.2 Petrophysics

The bulk density values obtained with the helium pycnometer are very heterogeneous and occur in a very wide range demonstrating the strong facies variation. Grain density results more stable, with calculated values around 2700 kg/m^3. Facies heterogeneity is confirmed also by pycnometer porosity data. Density data are comparable with data from the literature belonging to the Zhujiang Formation, the reservoir rock at the Liuhua 11-1 field in the South China Sea, which is similar to the Porto Badisco Calcarenite both in terms of skeletal components and in the facies association (Zampetti et al., 2005; Sattler et al.,2004). Another representative analogue in which similar density values to those presented in this paper have been log-measured in the reservoir of the Malampaya oil and gas field, the Nido Limestone, located in the offshore of the Philippine island of Palawan (Lallier et al., 2012; Fournier and Borgomano, 2007). The measured porosity is mostly connected (Tab 1.2). The non-interconnected porosity of the CM and SG facies, 2% and 0.88% respectively, were interpreted as caused by the presence of coral colonies characterized by primary porosity within the corals septa, porosity which has no interaction with effective porosity and possible permeability. Lower porosity values have been generally measured by the point counting technique. Point counting analysis of porosity underestimates

values up to 25% for facies RF. This porosity measurement, although it was performed on several statistically representative samples, is to be considered less reliable than the pycnometer measurement because quantitative point counting analysis is carried out on a small sample area and therefore it may be not representative of highly heterogeneous lithologies. Moreover, point counting works in only two dimensions to measure a petrophysical characteristic such as porosity which affects all the dimensions. Porosity values obtained from the image analysis are closer to data calculated with the pycnometer with respect to point counting porosity measurements (Fig.1.5). This is basically due to the larger area investigated by this technique with respect to point counting. The 10 times larger image allows a better statistics in calculating the pore areas in particular when pores have dimensions of about 1 mm.

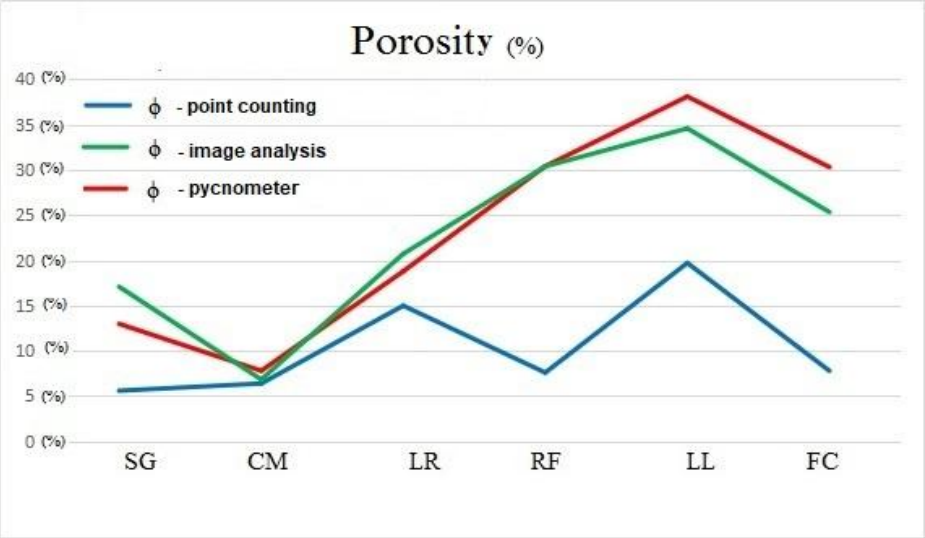

Fig.1.5. Comparison among porosity values of the facies measured through different methodologies. Blue line represents point counting porosity measurement on thin sections. Green line represents image analysis porosity measurement on slabs. Red line represents helium pycnometer porosity measurements on cored samples.

It is therefore clear from these results that porosity measurements are even more accurate when measured on a 3D volume as the pycnometer does.

Porosity data presented in this work are comparable, as well as densities, to those measured in log in the Zhujiang Formation and the Nido Limestone (Zampetti et al., 2005; Sattler et al.,2004; Lallier et al., 2012; Fournier and Borgomano, 2007) and moreover to values measured in the Chattian part of

the San Luis Formation of the Perla Field in the offshore Venezuela (Marini and Spadafora, 2014; Pomar et al., 2015; Valencia and Laya, 2020).

Also the seismic velocity measurements presented here are comparable to those measured in the similar facies constituting the analogues mentioned previously.

Seismic velocity obtained from oscilloscope measurements, show very heterogeneous data coherently with densities and porosities data.

Comparing the Vp values of the facies with the porosity values obtained with the pycnometer, samples show an anti-correlation in which the most porous facies are also those with the lowest Vp values (Fig.1.6).

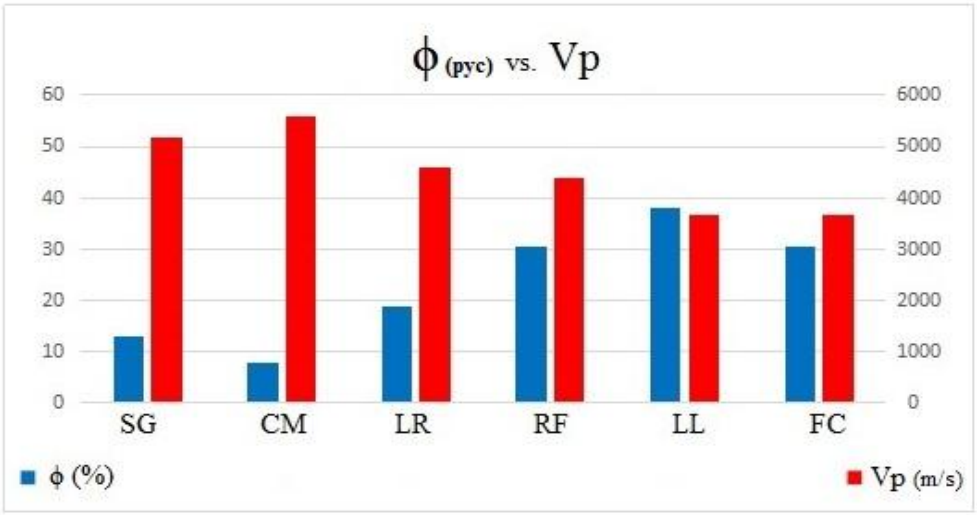

Fig. 1.6. Comparison among porosity values of the facies measured through helium pycnometer and Vp values obtained with the oscilloscope shows that higher porosity samples correspond to lower seismic velocity values.

1.5.3 Modelling

The petrophysical models shown in fig. 1.7 can help to build realistic models of characteristics distribution in other reservoir rocks developed in carbonate ramp systems.

Measured porosity and P-wave seismic velocity show a relatively wide range of values. The broad distribution of petrophysical properties results from heterogeneity due to depositional processes (Agosta et al., 2019) that lead to the development of different structures and textures that characterize each

facies, from grain size to diagenetic pathway to micropaleontological components (Brandano et al.,2020).

The resulting 2D petrophysical models are related to facies heterogeneities. The porosity model is consistent with the 3D facies model, and shows an increase in porosity toward the basin in the central sectors of the ramp where the LR, RF, and LL facies are most present, the latter measured as the most porous in the system. These facies show average porosity values of 19%, 30%, and 38%, respectively. The inner ramp, on the other hand, shows lower porosity values correlated with the SG and CM facies which have average porosity values of 12% and 6% respectively (Fig.1.7A).

As shown in Fig. 1.6, the most porous facies are those with lower seismic velocity values and thus the P-wave seismic velocity model, also well constrained to the 3D facies model, shows larger values for the SG and CM facies characterizing the inner ramp and smaller values related to the LR, RF and LL facies going toward the basin in the middle ramp sectors (Fig.1.7B).

The facies with higher seismic velocity values (CM and SG) were represented in the model in a range from 5573 m/s to 5183 m/s, LR and RF in a range from 4599 m/s to 4395 m/s, and the LL facies with lower values in a range from 3663 m/s to 3644 m/s.

These large variations in measured petrophysical properties allow for better constraints on the 3D modeling of facies heterogeneity.

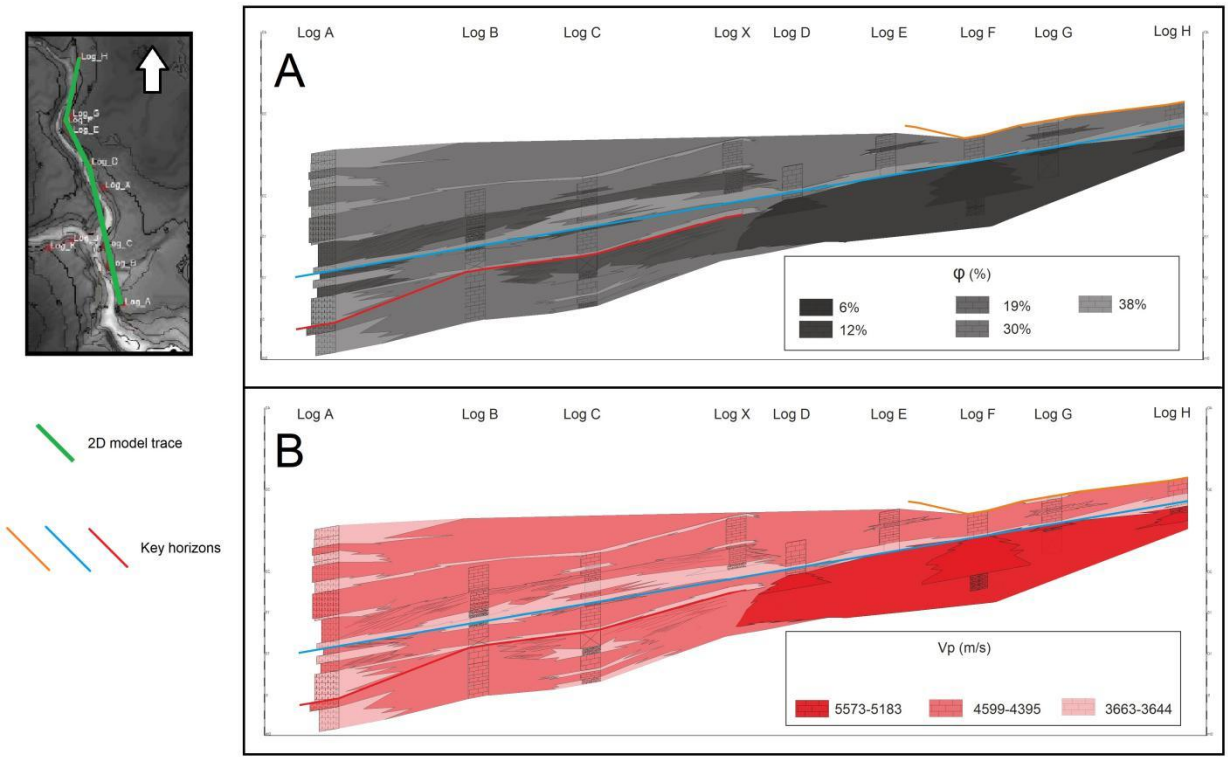

Fig.1.7. 2D Petrophysical models of the Porto Badisco calcarenite oriented approximately N-S along depositional dip direction whose trace is represented with a green line in the location map. Measured along-dip stratigraphic logs (A, B,C, X, D, E, F, G, H) are reported. The three key horizons observable in the field are reported with orange, cyan and red lines. A) Porosity model in which the porosity is represented in gray scale with more intense color for facies characterized by lower porosities and less intense color for higher porosities. B) P-wave seismic velocity model in which the seismic velocity is represented in shadow of red with more intense color for facies characterized by higher seismic velocities and less intense color for lower seismic velocities.

It is possible to recognize in the TGSim-based 3D model the six facies belonging to the Porto Badisco calcarenite (Fig.1.8). The 3D facies model reflects the spatial distribution of the facies on the carbonate ramp with the same distribution visible in outcrop. Comparing the 3D model to the schematic depositional model proposed by Pomar et al. (2014) shown in Fig. 1.4 the facies order is respected from the shallow water SG facies of the euphotic zone passing to the inner ramp CM and LR meso-oligophotic facies to the middle ramp oligophotic RF facies and LL facies of the deeper sector of the oligophotic zone to the last FC aphotic facies.

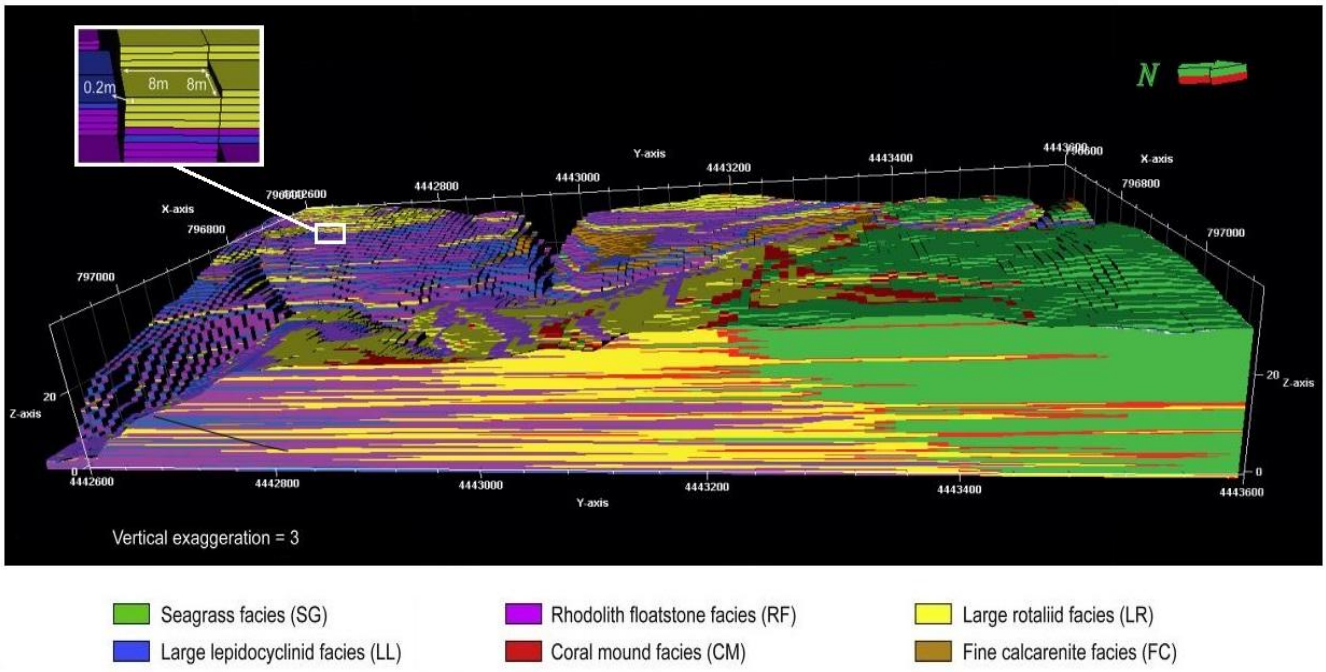

Fig.1.8. 3D facies model of the Porto Badisco carbonate ramp carried out with TGSim algorithm. Trough constraining tools such as measured stratigraphic field logs TGSim allows to replicate the facies variability in depositional profile as described by Pomar et al. (2014) highlighting the high facies heterogeneity (modified after Tomassetti et al., 2018).

Taking into consideration the CM facies, this is interdigitated with its contiguous facies such as SG and LR. The mound structure shape of CM is also respected in the 3D model where it is represented as lenses embedded within the SG and LR facies. Results shows that TGSim and outcrop data adequately match. TGSim algorithm resulted a powerful tool in reproducing the depositional system and facies in agreement with data obtained from field observation.

A possible modeling pitfall that alters results in many cases, especially for facies with a nonlinear distribution, such as granular facies lies in incorrect application of Walther's law to the modeling in an attempt to predict facies distribution in areas without data but this does not appear to be the case in the presented model.

Several papers highlight how 3D models fairly closely reproduce the depositional geometries observed in outcrop, emphasizing the relationships between the stratigraphic architecture of the depositional model and the transitions of facies associations that produce the heterogeneity. San Miguel et al. 2013 modeled the facies heterogeneity of a Kimmeridgian carbonate

ramp in eastern Spain by combining outcrop analysis and construction of a 3D model representing the facies heterogeneity of a carbonate ramp using the TGSim algorithm. Amour et al. 2012 demonstrate that TGSim is a suitable algorithm to simulate the distribution of facies within depositional environments by modeling the spatial heterogeneity of facies on a metric scale in a Jurassic carbonate ramp in the Moroccan Atlas. Tomás et al. 2010 to build a 3D facies model of the Sedini Limestone of the Burdigalian in Sardinia choose a Sequential Indicator Simulation (SISim) algorithm to model only vertical facies relationships. They noticed with TGSim that facies variations for vertical platform evolution are too abrupt. In contrast, for the Porto Badisco calcarenite, the 3D facies model run with the TGSim algorithm fits perfectly with what was observed in the field and described by Pomar et al., 2014.

The 3D facies model provides an improvement in interpret the depositional dynamics described by Pomar et al., 2014 in 2D adding insights on the predictability of the distribution on the facies belts especially in the portions that do not outcrop. A reliable relationship between geology and geostatistics in terms of vertical and horizontal ranges of distribution of values through the use of the stochastic algorithm allows for the assessment of more spatially distributed facies heterogeneity.

The use of a two-dimensional facies model, even if it leads to interpret a correct depositional model, results in a less detailed reproduction of the correlation of the lateral and vertical heterogeneity of facies compared to the algorithm applied in 3D that offers an improved prediction of the facies distribution from a geostatistical point of view (Yao and Chopra, 2000).

The improvements made by 3D imaging in understanding the range of distribution of facies heterogeneity in different environments is critical to enhance subsurface interpretation (Greenfield et al., 2019).

However, stochastic modeling is widely used as one of many tools to improve the description of reservoir analogs combined with data from outcrop studies (Tjolsen et al., 1996).

Chapter 2: From petrophysical properties to forward-seismic modelling of facies heterogeneity in the carbonate realm (Majella Massif, central Italy)

The results of this work have been published to the Journal of Petroleum Science and Engineering edited by Elsevier. (Andrea Tomassi, Fabio Trippetta, Roberto de Franco, Roberta Ruggieri. "*From petrophysical properties to forward-seismic modeling of facies heterogeneity in the carbonate realm (Majella Massif, central Italy)*", 2022, https://doi.org/10.1016/j.petrol.2022.110242).

2.1 Forward modelling of a surface analogue reservoir. Insight from the Majella Massif.

This work addresses the seismic response of carbonate facies. In order to perform a seismic forward modelling samples belonging to the carbonate ramp outcropping on the Majella Massif are collected. Also in this case, the study starts from the field and then it goes to the laboratory where petrophysical characterization of lithologies is carried out. Data are then used to perform forward modelling.

Forward modelling is a fundamental support to the study of the seismic response of reservoirs structure and architecture in the subsurface. Forward modelling can help address issues related to visualization of buried structures and thus facilitate their interpretation, which, especially in carbonate systems, is far from trivial. In addition, synthetic seismic forward modeling can lead to the production of data useful for exploration in those areas where there are few wells drilled or where geophysical surveys have not been conducted. Carbonate reservoirs result in non-univocal seismic response caused by the facies heterogeneity and due to the possible presence of infilling fluids. The carbonate ramp outcropping in the Majella Massif (Central Italy) is an excellent surface analogue of buried heterogeneous structures. It offers the opportunity to directly analyse a carbonate reservoir which clearly shows facies variations and natural hydrocarbon-impregnations allowing to quantify the induced petrophysical changes. In this study original field and laboratory measurements with 3D facies modelling are integrated to carry out 1D and 2D forward seismic models of a carbonate reservoir following a structured workflow. A careful petrophysical characterization – measuring density porosity and seismic wave velocities – is performed in all the sampled facies and it is converted as input for the 3D velocity model. The aim of this work is to model the facies heterogeneity to understand its seismic response and to produce synthetic seismic lines as realistic as possible reproducing what is normally not visible on a commercial seismic line due to lack of resolution facilitating subsurface interpretation. Carbonate reservoir samples belong to the same formation which outcrops naturally in saturated and unsaturated

conditions. As a results it is possible to quantify the influence of such hydrocarbons in seismic forward modelling.
A peculiar workflow is developed. Facies modelling is linked to forward modelling that can be used to better interpret seismic images of fluid-filled carbonate reservoirs with applications in hydrocarbons exploration, geothermal studies, potential CO_2 or hydrogen storage and to monitor possible leakages from the reservoirs (Aminu et al. 2017; Dockrill and Shipton, 2010; De Franco et al., 2019; Heinemann et al., 2018; Trippetta et al., 2013).

2.2 Geological setting

In order to model the heterogeneity of carbonate facies and their seismic response this work focuses on the exceptionally exposed carbonate ramp outcropping on the Majella Massif in central Italy (Fig. 2.1). The Majella Massif is a N–S/NW-SE oriented anticline plunging both North and South (Patacca et al., 2008; Cornacchia et al., 2017). It is the northernmost continuation of the Apulian Carbonate Platform, one of the several peri-Adriatic carbonate platforms developed in the southern margin of the Mediterranean Tethys (Bernoulli, 2001; Rusciadelli and Ricci, 2008; Tomassetti et al.,2018). Its sedimentary succession is represented by Jurassic to upper Miocene limestones and dolostones.
During the Mesozoic, a northward extending erosional escarpment developed, which created a depositional environment suitable for the sedimentation of shallow water carbonates (Vecsei et al., 1998; Vecsei and Sanders, 1999). From Campanian the Orfento Formation has developed prograding on the slope (Rusciadelli and Ricci, 2008). The Paleocene to Eocene succession in represented by the Santo Spirito Formation continuous in the basin and slope and characterized by hiatuses on the platform top. Above a discontinuity surface the Oligo-Miocenic Bolognano Formation overlies the Santo Spirito Formation (Mutti et al., 1997; Brandano et al., 2012, 2016). The Bolognano Formation was divided in five informal members (Mutti et al., 1997, 1999; Brandano et al., 2012, 2016). The first is represented by the Rupelian to late Chattian Lepidocyclina Calcarenites 1 (LP1), a cross-bedded packstones to

grainstone with Larger Benthic Foraminifera. This unit is overlaid by the thin Cherty and Marly Limestone member (CM). Above the latter, the dominance of the foraminifer Lepidocyclina restarted, causing the deposition of the Lepidocyclina Calcarenites 2 member (LP2) from the late Aquitanian to the late Burdigalian. Going upwards in the succession there is the Serravalian-Tortonian Hemipelagic Marls member (HM). The uppermost member belonging to the Bolognano Formation is the Lithothamnion Limestone (LL) Tortonian to Messinian in age (Brandano et al., 2012, 2016).

The Majella carbonate ramp – sedimented from the Cretaceous to the Miocene – represents an excellent surface analogue of carbonate buried reservoirs such as the fields exploited in the Adriatic Sea, offshore Venezuela, Philippines and South China Sea (Tomassetti et al., 2021). Natural bituminous impregnations are quite frequent on the north-western flank of the massif concentrated in the Lettomanoppello-Fonte di Papa-Fonticelle and Sterparo-Cerratina areas, where many shallow wells were drilled in the past for the extraction of heavy hydrocarbon (Lipparini et al., 2018). In addition, this reservoir has been exploited in the Cigno and Vallecupa oil fields located approximately 10km to the north-west of the Majella (Trippetta et al., 2021).

The modelling presented in this work is carried out in the area that extends from the NW side of the Majella, in the Lettomanoppello-Fonte di Papa-Fonticelle and Sterparo-Cerratina areas, which represents the platform top, going towards the North in the Cigno and Vallecupa oil fields (Fig. 2.1).

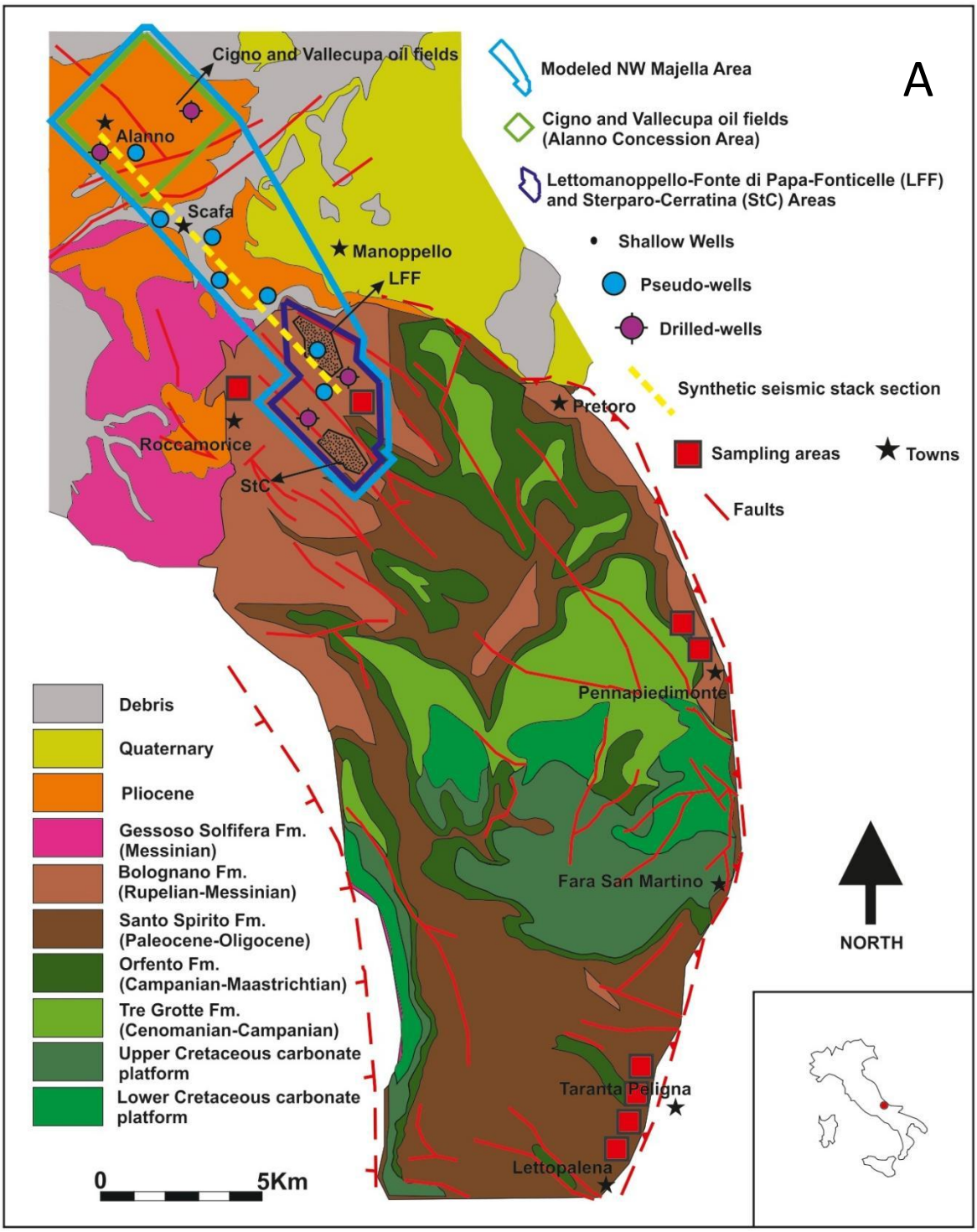
A
Cigno and Vallecupa oil fields
Alanno
Scafa
Manoppello
LFF
Roccamorice
StC
Pretoro
Pennapiedimonte
Fara San Martino
Taranta Peligna
Lettopalena
Modeled NW Majella Area
Cigno and Vallecupa oil fields
(Alanno Concession Area)
Lettomanoppello-Fonte di Papa-Fonticelle (LFF)
and Sterparo-Cerratina (StC) Areas
Shallow Wells
Pseudo-wells
Drilled-wells
Synthetic seismic stack section
Sampling areas
Towns
Faults
Debris
Quaternary
Pliocene
Gessoso Solfifera Fm.
(Messinian)
Bolognano Fm.
(Rupelian-Messinian)
Santo Spirito Fm.
(Paleocene-Oligocene)
Orfento Fm.
(Campanian-Maastrichtian)
Tre Grotte Fm.
(Cenomanian-Campanian)
Upper Cretaceous carbonate
platform
Lower Cretaceous carbonate
platform
0
5Km
NORTH

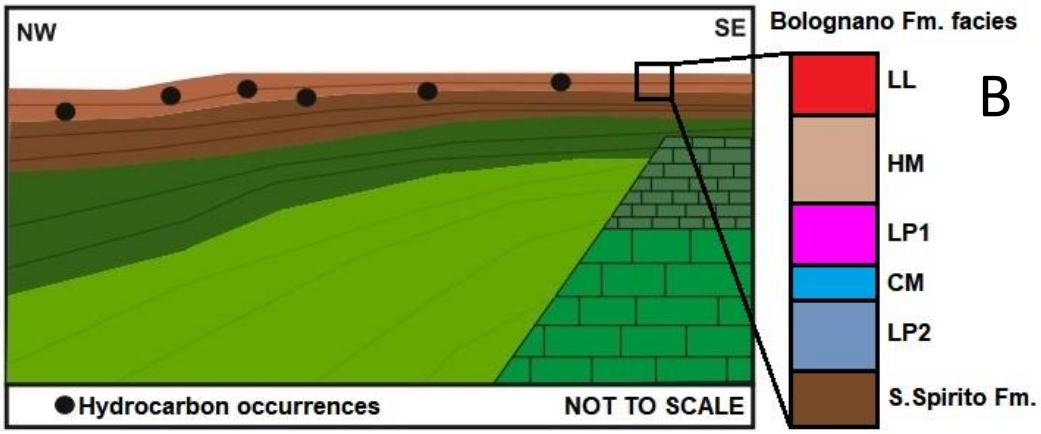

Fig. 2.1. A) Simplified geological map of the Majella Mountain (modified after Vecsei and Sanders, 1999 and Trippetta et al. 2021) showing sampling areas (red squares) and modeled areas: Alanno concession (green boundary), the NW Majella area (blue boundary) that contain the LFF and StC Areas with the shallow wells (black dots), all included in the modeled area (light blue boundary). Location of the synthetic seismic stack section modeled in this work is reported inside the modeled area and represented with a dashed yellow line. Cyan dots circled in black represents the pseudo-wells locations. B) Stratigraphic scheme illustrating stratigraphic relationships and geometries of formations, and facies that characterize the members of the Bolognano Formation. Hydrocarbon occurrences are reported as large black dots.

2.3 Methods

2.3.1 Field work and sampling

Twenty-five rock blocks on the carbonate ramp from top Cretaceous to Miocene are collected in the field to be characterized.

Samples are collected from different locations that correspond to relatively different positions along the depositional profile because it is not always possible to collect samples in the exact areas where the lithologies are modeled. Another fact to be considered is that the facies and the proportions between the different textures change along dip but, despite this fact, the reality limits are too complex to be considered in all its aspects and for this reason models like the one presented in this work are built.

Sampling covered the following formations: the Orfento Formation, the Santo Spirito Formation and the Bolognano Formation outcropping in the study area (Fig. 2.2). The Orfento Formation is sampled in the Pennapiedimonte village area where the Tre Grotte Valley produces large outcrops. The Santo Spirito Formation is mainly sampled on the southern side of the massif close to

Taranta Peligna town but also in the Pennapiedimonte village area. The Bolognano Formation sampling is performed on the NW flank of the Majella Massif close to Roccamorice and Lettomanoppello towns (Fig. 2.2). Sampled rock blocks are successively cut into square-based parallelepipeds with sides of about 4 cm and height of about 5 cm for laboratory measurements.

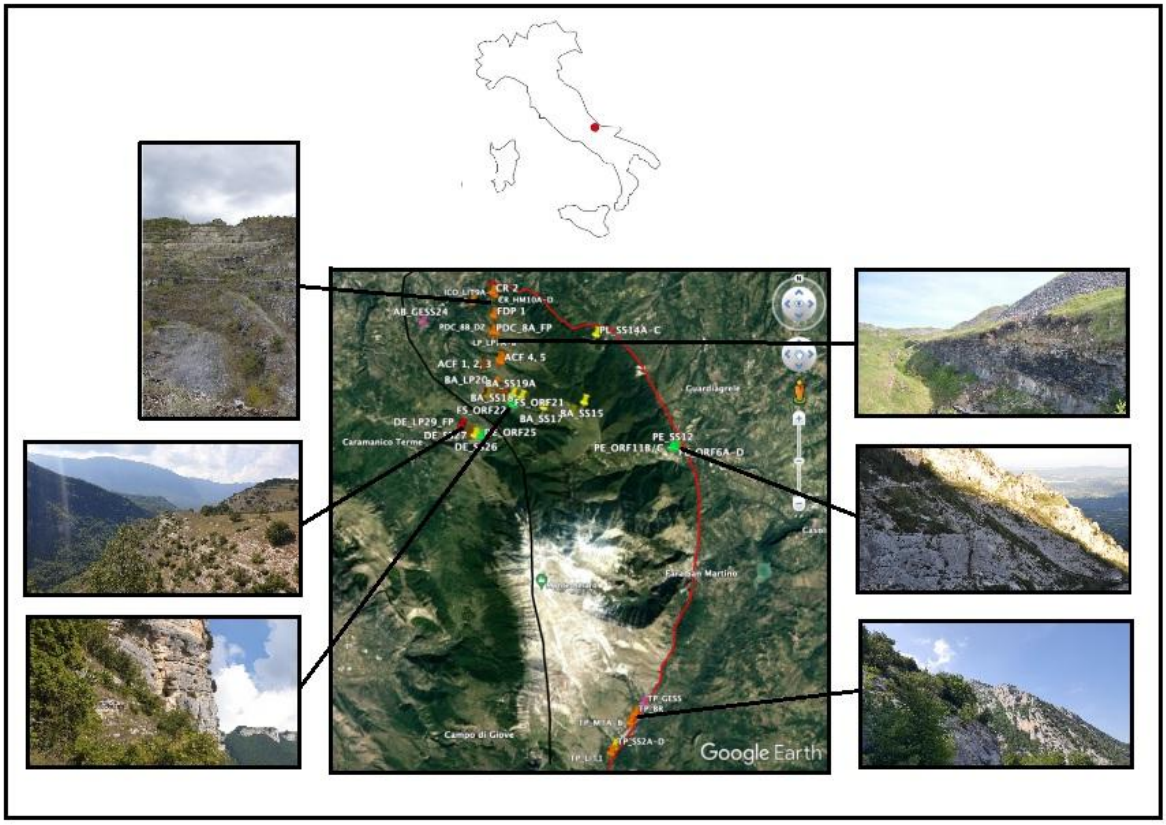

Fig. 2.2. Locations of collected samples and outcrops view.

2.3.2 Laboratory measurements

Density and porosity are measured using Anton Paar Ultra-pyc 5000 helium pycnometer.

P-wave velocity (Vp) and S-wave velocity (Vs) are measured by using the USB 8M 8-channels multiplexed system ultrasonic device generator developed by Mistras Eurosonic connected with two 1 MHz piezoelectric transducers. First arrivals of the P and S-waves are analyzed and they are picked manually from the waveforms. All the above laboratory measurements are carried out on both clean and bitumen-saturated samples. Measured

petrophysical properties (porosity, density and seismic velocity) of both clean and bitumen-saturated samples provide data that allow to perform the forward synthetic seismic modelling with different seismic responses (Trippetta and Geremia, 2019; Ruggieri and Trippetta, 2020).

2.4 Samples characterization

2.4.1 Thin section analysis

A set of 25 thin sections from samples collected during the field work is produced to recognize the facies characterizing the different Formations of the Cretaceous-to-Miocene carbonate ramp succession outcropping on the Majella Massif. The facies are classified according to Dunham (1962) and Embry and Klovan (1971) (Fig.2.3).

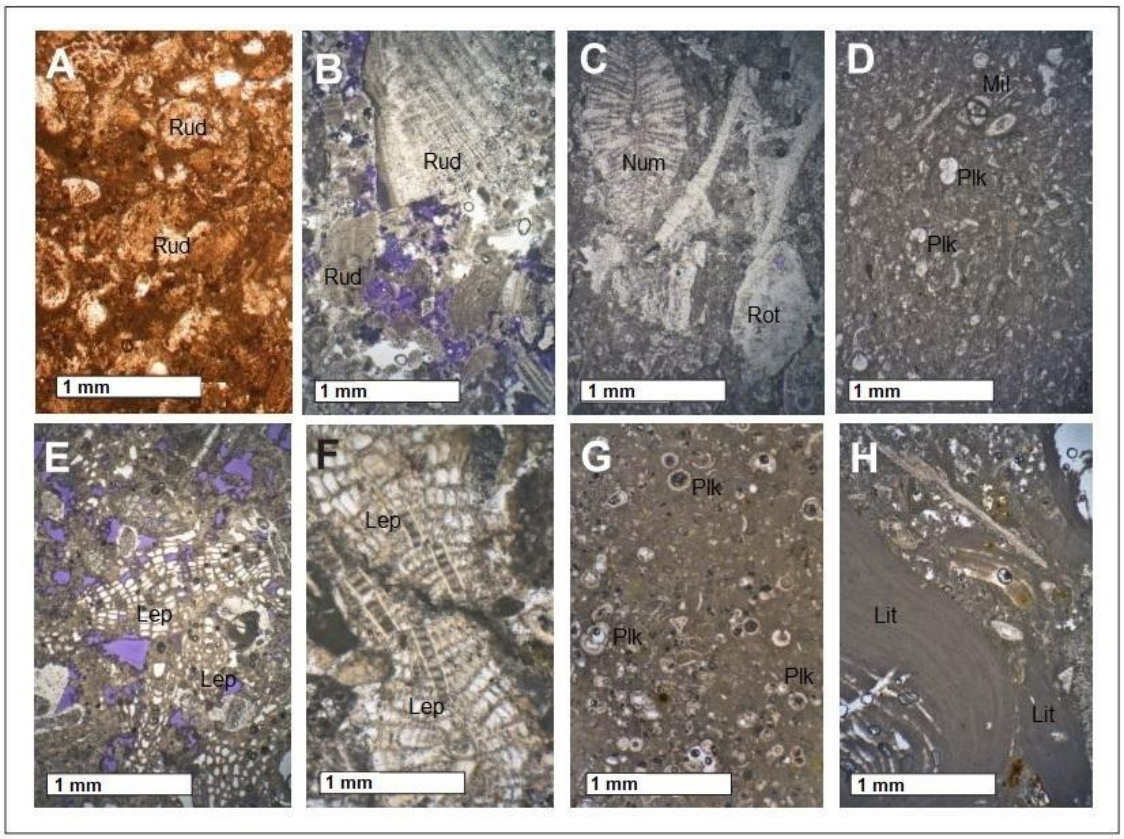

Fig.2.3. Sampled facies in thin section: A) Poorly cemented bioclastic grainstone-packstone (ORF2); B) Rudstone with large rudists fragments (ORF1); C) Grainstone to rudstone with nummulitids and rotalides (SS2); D) Fine wackestone rich in planktonics foraminifera with miliolids (SS1); E) & F) Porous rudstone is rich in Lepidocyclinids benthic foraminifera (LP); G) Fine-grained wackestone with dominant clay component and planktonic foraminifera(HM); H) Grainstone locally rudstone rich in red algae (LL). Rud: rudists. Num: nummulitids. Rot: rotalids. Mil: miliolids. Plk: planktonic foraminifera. Lep: lepidocyclinids. Lit: lithothamnion. Scale bar = 1 mm.

Orfento Formation (ORF)

Two facies belonging to ORF identified by Mutti et al., 1996 are sampled. A rudstone with large rudists fragments (ORF1) testifying the expression of the dismantled Cretaceous margin of the carbonate platform. Therefore, this facies is typical of the high energetic hydraulic regime caused by the wave motion above the half wavelength limit.

A second facies corresponds to a grainstone-packstone with clasts that rarely reach 2mm in size composed of a bioclastic mince, poorly cemented and friable (ORF2). This facies sedimented in a fairly energetic hydraulic regime but below the limit of the ordinary wave base in correspondence with the first section of the slope.

Santo Spirito Formation (SS)

Two facies belonging to SS identified by Raffi et al., 2016 have been sampled. The first one is a very fine wackestone rich in planktonic biota (SS1). This facies deposited in the distal portion of the slope, in the aphotic zone without marine hydraulic currents as demonstrate by the fine size of clasts of the sediment and the presence of planktonic foraminifera.

The second facies (SS2) corresponds to a grainstone to rudstone with large benthic foraminifera. Foraminifera mostly include nummulitids and rotalides. Some porcelain shell foraminifera are also found. This second facies – belonging to SS – is typical of the mesophotic zone, between the limit of the ordinary wave base and the limit of the storm wave base. The porcelain foraminifera belong to the photic zone, the upper portion of the carbonate platform and very close to the shore line. Finding biota dwellers in such distant areas of the platform, as well as finding a distal facies belonging to the same formation, means that the dismantling of the platform caused by gravitational phenomena such as submarine landslides and calciturbidites allowed bypass of sedimentary material from the top of the platform to the bathymetrically deepest portions of the depositional system. This is evidenced by the presence of porcelain foraminifera of shallow environments concomitant with the presence of the nummulitids typical of intermediate bathymetry and very fine material of the deeper environments with low hydraulic regime (Pomar et al., 2014, 2017).

Bolognano Formation

Five facies belonging to this Formation are sampled, as identified by Brandano et al. 2016. 1). The Lepidocyclina Calcarenites 1 (LP1) is a very porous rudstone rich in Lepidocyclinids benthic foraminifera dwellers of the mesophotic zone in which this facies developed with a medium-high hydraulic regime, ensuring that the biota of that portion of the carbonate ramp have a necessary size not to be transported by the wave motion (Pomar et al., 2014, 2017). 2) The Cherty and Marly Limestone (CM) is a bioclastic cherty wackestone to packstone resulted from a drowning event which produced a shift toward the low-energy outer ramp environment as demonstrate by the fine grain size (Brandano et al., 2016). 3) The Lepidocyclina Calcarenites 2

(LP2) is similar to LP1 in grain size and microfossilis therefore belonging to the same depositional environment and it occurs in the field outcrops in both clean and bitumen-saturated conditions. 4) The Hemipelagic Marls (HM) is a fine-grained wackestone with a more or less dominant clay component and planktonic foraminifera testify an outer ramp environment. It is a marly limestone that demonstrates the input of terrigenous material coming from behind the shore line or from an important river course. 5) The Lithothamnion Limestone (LL) is a grainstone to rudstone porous limestone rich in red algae known as lithothamnion. These algae, unlike green algae, do not need great light penetration below the sea surface to survive. They are indicators of the distal portion of the mesophotic zone in the ramp-shaped depositional model. Rolling along the slope profile they often form rounded aggregates called rhodoliths (Brandano et al., 2010).

2.4.2 Laboratory measurements

Density

Age	Formation/Bolognano Fm. Members	Bulk Density kg/m^3	Grain Density kg/m^3	Source
Pliocene	Flysch cover (**FC**)	2000	-	Mascolo and Lecomte, 2021
Tortonian-Messinian	**LL**	2200	2720	This work
Serravalian-Langhian	**HM**	2290	2690	This work
Burdigalian	**LP2** **LP2** bitumen-saturated	1870 2260	2730 2690	This work; Trippetta and Geremia, 2019; Trippetta et al.,2020; Ruggieri and Trippetta , 2020
Aquitanian	**CM**	2280	2710	This work
Rupelian-Chattian	**LP1**	1900	2730	This work
Priabonian-Rupelian	**SS2**	2530	2770	This work
Lutetian-Priabonian	**SS1**	2620	2750	This work
Maastrichtian	**ORF2**	1950	2720	This work
Campanian	**ORF1**	2070	2720	This work

Tab. 2.1. Bulk and grain density values (expressed in kg/m^3) of the lithologies characterized with their ages. The source column indicates the seismic velocity data origin. In red density of the bitumen-saturated LP2 facies.

Density measurements are reported in Tab. 2.1. The Grain density shows values around 2700 kg/m^3 as expected for pure carbonate (e.g. Mavko et al., 2009). Bulk density ranges from a minimum of about 1870 kg/m^3 measured for the LP2 facies, to a maximum of 2530 kg/m^3 for SS. The standard error is in the range 0,0372g/cm^3 to 0,0770g/cm^3.

Porosity

Measured porosities are reported in Tab. 2.2.

Age	Formation/Bolognano Fm. Members	ϕ tot. %	ϕ eff. %	Source
Tortonian-Messinian	**LL**	18,68	18,28	This work
Serravalian-Langhian	**HM**	15,04	14,65	This work
Burdigalian	**LP2** **LP2** bitumen-saturated	30,01 14,04	29,18 -	This work; Trippetta and Geremia, 2019; Trippetta et al.,2020; Ruggieri and Trippetta , 2020
Aquitanian	**CM**	12,4	12,1	This work
Rupelian-Chattian	**LP1**	29,68	29,18	This work
Priabonian-Rupelian	**SS2**	8,48	6,34	This work
Lutetian-Priabonian	**SS1**	4,76	1,15	This work
Maastrichtian	**ORF2**	28,56	28,01	This work
Campanian	**ORF1**	24,02	23,58	This work

Tab. 2.2. Age of the characterized facies with total and effective porosity values (expressed in %) measured in laboratory. In red porosity of the bitumen-saturated LP2 facies. The source column indicates the porosity data origin.

The total porosities measured vary from about 4.76% for the SS1 to more than 30% of the LP2 facies. The effective porosities are approximately equal to the total porosities. ORF1 have porosity value of 24,02% and ORF2 of 28,56. Moving upward in the stratigraphy, the SS1 shows a value of 4.76% and SS2 of 8.48%. Above, the LP1 have a measured porosity of 29,68, CM of 12,4% and LP2 of 30.01%. The HM facies which overlies the reservoir show 15,04% of porosity. Stratigraphically above all others, the LL facies have a porosity of 18,68%. The standard error is within 2%.

Vp

Measured P-waves of the lithologies of the area, are reported in Tab. 2.3.

Age	Formation/Bolognano Fm. Members	Vp m/s	Source
Pliocene	Flysch cover (**FC**)	2850	Mascolo and Lecomte, 2021
Tortonian-Messinian	**LL**	3720	This work
Serravalian-Langhian	**HM**	3920	This work
Burdigalian	**LP2** **LP2** bitumen-saturated	3630 4808	This work; Trippetta and Geremia, 2019; Trippetta et al.,2020; Ruggieri and Trippetta , 2020
Aquitanian	**CM**	3700	This work
Rupelian-Chattian	**LP1**	3650	This work
Priabonian-Rupelian	**SS2**	5300	This work
Lutetian-Priabonian	**SS1**	5500	This work
Maastrichtian	**ORF2**	3400	This work
Campanian	**ORF1**	4000	This work

Tab. 2.3. Age of the characterized facies with seismic velocity data measured in laboratory. In red porosity of the bitumen-saturated LP2 facies. The source column indicates the seismic velocity data origin.

.

The velocities of the longitudinal elastic waves (Vp) through the samples ranges from a minimum of about 3630 m/s for the LP facies up to 5500 m/s measured for SS whilst Vs range from 2120 m/s (ORF) to 3100 m/s (SS). The Vp/Vs ratio spans from 1,56 calculated for clean LP to 1,89 for bitumen-saturated LP. The standard error is between 2,2% and 4%. In order to complete the dataset necessary for the model literature velocity data acquired on the same area are integrated. The seismic velocity of Flysch cover overlying the carbonate succession have been measured by Mascolo and Lecomte, 2021 with a Vp of 2850 m/s and a Vs of 1390 m/s.

2.5 Model building

The 3D structural model is built in Petrel by the following steps.

The axes of the 3D volume were oriented following the geological features. One direction was set parallel to the dip of the main NW-SE oriented tectonic structures (Fig. 2.4), one perpendicular to the same structures, and the last parallel to the depth. Then, the volume with a dense grid of 10x10x10m sized cells is built (Janson et al., 2007b; Janson et al., 2011).

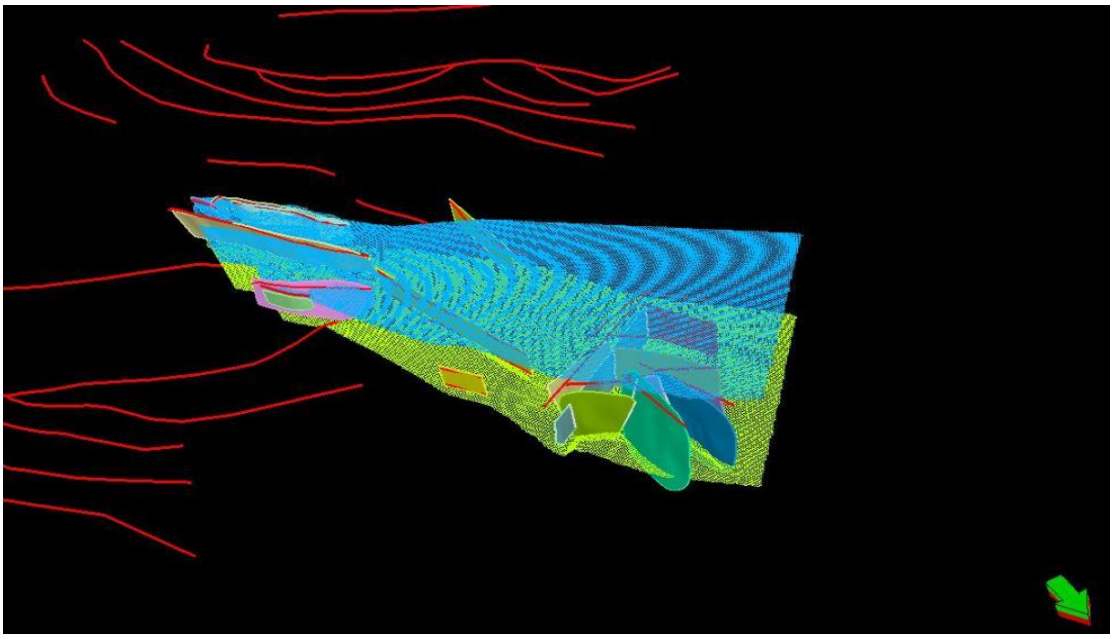

Fig. 2.4. Petrel view of the 3D grid top (in cyan) and bottom (in yellow) and its orientation with respect to the structures represented as red lines and coloured planes between the 3D grid top and bottom.

Topography is imported from a digital earth model (DEM) with a resolution of 10m. This surface represents the top surface of the model. Formation tops are then created using the well-tops data of the investigated formations (ViDEPI Project, 2012) and the thicknesses obtained from stratigraphic sections measured in the field, where available. Informations on geologic layers thicknesses were collected mainly from the few open-data wells available. On the NW flank of the Majella Massif informations from the Caramanico and Maiella 2 wells was taken into account (southern purple dots circled in black in fig.1) as well as data collected from 178 vertical wells drilled by Azienda

Lavorazione Bitumi Asfalti (ALBA) in two areas named Lettomanoppello–Fonte di Papa–Fonticelle (LFF) area, investigated by 43 wells, and the Sterparo–Cerratina (StC) area, investigated by 135 wells (black dotted area included in the black polygons in fig.1) (Lipparini et al., 2018). Caramanico is the deepest well of the area with a total depth of 5075m up to the Triassic lithologies. The first lithology drilled from this well is the Bolognano Formation with a thickness of 100m divided into 38m of the HM Member, 22m of the LP2 Member and 40m of the LP1 Member. The Caramanico well below the Bolognano Fm. drills the Santo Spirito Formation for a thickness of 70m and then the 170m thick Orfento Formation. The Maiella 2 well, drilling down to the Triassic with a total depth of 1656m, after 17m of flysch cover it perforates the Bolognano Fm. for 92m. Of this thickness 23m are attributable to the LL member, 10m to the HM member and 59m to the LP2 member. Below, the Santo Spirito Formation is drilled by Maiella 2 well for a thickness of 40m and the Orfento Formation for a thickness of 190m. To obtain the thicknesses of all the constituent members of Bolognano Fm. we used data from stratigraphic sections measured in the field and data coming from the shallow wells drilled by ALBA company, with total depths in the range of 80 to 200m below surface to the Santo Spirito Fm. From these data resulted the following Bolognano Fm. members maximum thicknesses: LL 60m, HM 90m, LP2 100m, CM 25m, LP1 50m.

Information on the thicknesses of the modeled lithologies for the distal portion of the carbonate ramp buried beneath the Cigno and Vallecupa oil fields was obtained from the study of the Cigno 2 and Vallecupa 45 wells (northern purple dots circled in black in fig.1). These are the only wells available in the Alanno concession that drill below the Eocene. Cigno 2 well reaches a total depth of 2422m to the Upper Jurassic lithologies. In this well, after 720m of flysch cover, drills for 200m the Bolognano Fm.: 100m attributable to the LL facies, 50m to the HM facies and 50m to the LP2 facies. Below the Bolognano Fm. the Santo Spirito Fm. is nearly 400m thick as well as the Orfento Fm. Vallecupa 45 well have a total depth of 2969m up to Triassic. The first lithology drilled by this well is the flysch cover 490m thick. Below, a thickness of 80m is represented by the Bolognano Fm. with 45m referred to the LL

facies, 25m to the HM facies and 10m to the LP2 facies. The Santo Spirito Fm. is 100m thick in this well and the Orfento Fm. reaches 320m (Tab 2.4).

WELLS / FACIES		Alanno Concession wells		NW Majella Flank wells		
		Cigno 2	Vallecupa 45	Majella 2	Caramanico	ALBA wells
Flysch cover		720m	490m	17m	/	/
Bolognano Fm.	LL	100m	45m	23m	/	60m
	HM	50m	25m	10m	38m	90m
	LP2	50m	10m	59m	22m	100m
	CM	/	/	/	/	25m
	LP1	/	/	/	40m	50m
Santo Spirito Fm.		400m	100m	40m	70m	/
Orfento Fm.		~400m	320m	190m	170m	/

Tab.2.4. Thicknesses of the characterized facies obtained from open-data wells available then used to perform the petrophysical model.

The comparison between the thicknesses observed in outcrops and in wells on the NW flank of the Majella Massif and the thicknesses in wells located ~10 km to the NW in the Cigno and Vallecupa oil fields, which drilled at greater depths the same facies sampled and analyzed, suggests that the carbonate ramp system is relatively undeformed and laterally continuous (Trippetta et al., 2020).

The well data were useful for determining the lithologies thicknesses in the model as the petrophysical data were totally measured in the laboratory.

The scarcity of deep drilling and geophysical surveys means that there are not a lot of open-source data available in the Majella area. To increase the amount of subsurface data available we assumed to create synthetic simsic lines in this area.

To correctly model the zones (i.e. layers) facies are identified from the thin section analysis. The complete list of detected facies is reported in table 2.1 and it represents the most complete record of lithostratigraphic units that could be drilled by a hypothetical well. However, passing from a single well (1D) to a 3D model some considerations have to be done.

For the oldest formation of the model (Orfento Formation) previously two facies were identified. However, their spatial distribution is strongly discontinuous making hard to properly separate the two facies in the model. Consequently, in the 3D model, are modeled both the facies of the ORF in petrophysical and forward modelling as a single formation taking in account the variability of the petrophysical properties of both the facies by averaging the measured values (Fig. 2.5-B).

The similar approach can be used for the SS facies, and thus they are modeled both the SS facies as a single formation.

For the five facies of the Bolognano Fm., the CM facies has not been drilled by any well pertaining to the Alanno concession. Consequently, this facies is not modeled. LP1 and LP2 facies are characterized by very similar petrophysical characteristics, thus they are merged in a single facies named LP (Fig. 2.5-B) whilst HM and LL are included in the 3D model.

Uniforming the facies unfortunately we will lose information on heterogeneity but as mentioned the modeling imposes limits despite trying to get it as close as possible to the reality.

Following the regional stratigraphy, a Flysch cover (FC) overlying the carbonate succession is added in order to complete the model. The thickness of FC was considered as what was deposited from the topographic surface of the DEM to the top of the Bolognano Fm. From the model, therefore, it appears that FC lay down in onlap on the flank of the Majella Massif where older lithologies than the flysch outcrop.

Consequently, six zones in the Petrophysical 3D model from top to bottom are defined:

The Flysch cover (FC), Lithotamnion Limestones (LL), Hemipelagic Marls (HM), Lepidocyclina Calcarenites (LP),Santo Spirito Formation (SS) and Orfento Formation (ORF) (Fig. 2.5-B).

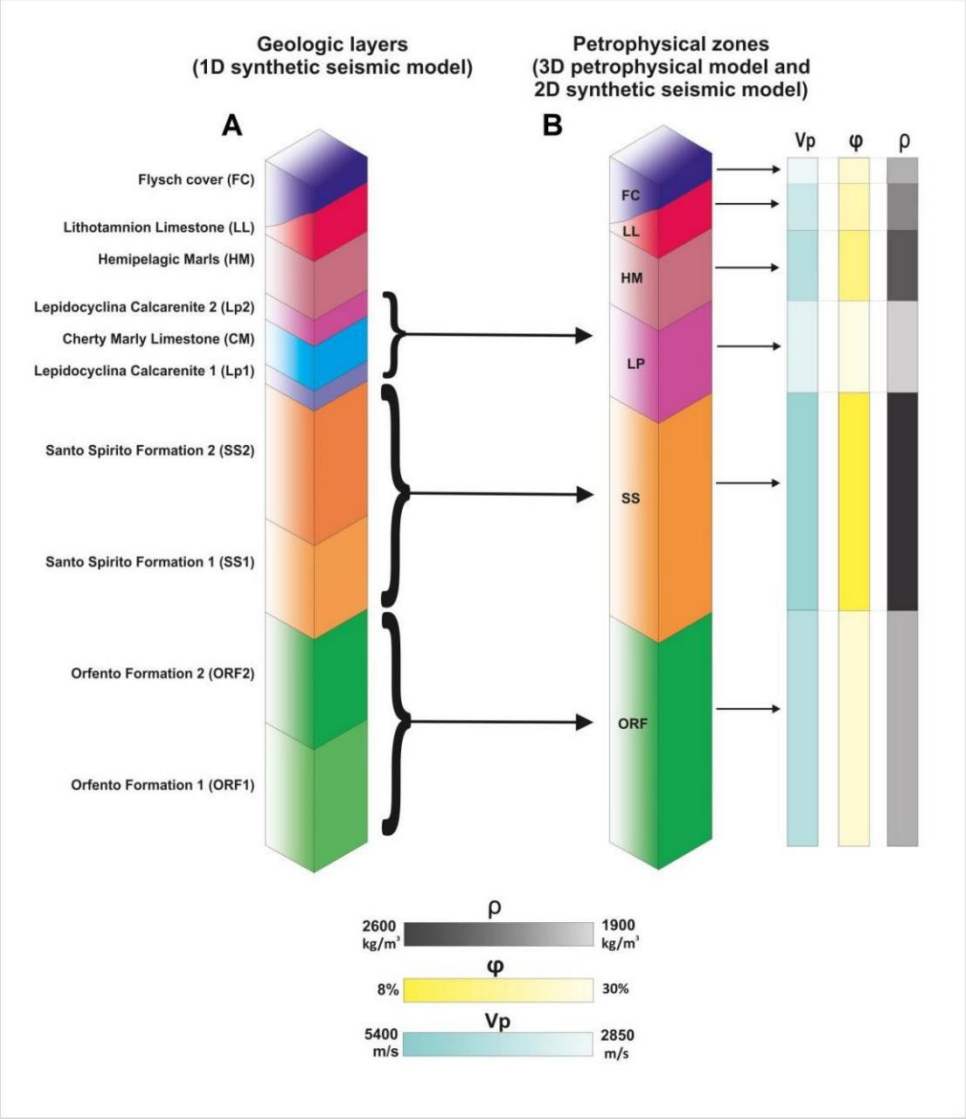

Fig. 2.5. Modeled layers and zones. A) Geologic layers used to perform the 1D synthetic seismic model. B) Petrophysical zones obtained by merging LP1 and LP2 facies in LP, SS1 and SS2 in SS and ORF1 and ORF2 in ORF used to perform the 3D petrophysical model and the synthetic seismic stack section. In grayscale are represented the density values of the petrophysical zones. In yellow are represented the porosity values of the petrophysical zones. In light blue are represented the Vp values of the petrophysical zones.

Once defined the number of zones, it is possible to start populating the cells with the proper seismic velocities.

Due to the small number of drilled wells, some areas of the model would be uncovered and the model would excessively approximate the seismic velocity of the cells. Thus, where no wells are present, seven Pseudo-wells (Fig. 2.1) logs calculated from laboratory measurements and outcrops data are created. These Pseudo-wells allow to force the model in populating the nearby cells with constrained data instead of model-calculated values.

Property modelling

Through the Petrel property modelling tool, the petrophysical zones are firstly populated with the User Defined algorithm (UD) as commonly done in seismic forward modelling (Mascolo and Lecomte, 2021). The UD is an algorithm customized by the operator with variables derived, in our case, from laboratory measurements. With the UD constant velocity values are provided for each zone by averaging the measured Vp values (Fig. 2.6-A).

In order to simulate a reliable distribution of velocities, cells are populated with heterogeneous velocities within each zone using the “Sequential Gaussian Simulation (SGS)” algorithm that is a stochastic method. This method can produce a range of uncertainty of a variable producing local changes in the distribution of facies and petrophysical properties (Journel and Ying, 2001). It should be noted that the Porto Badisco carbonate ramp model showed good results by using the TGSim algorithm where the Truncated Gaussian Simulation (TGSim) cut the coda values of the Gaussian distribution allowing more reliable facies identification. However, such coda-data can have a large influence in models where the variation of the petrophysical properties (i.e. the Vp) are investigated. Consequently, as expected, SGS (not-truncated) stochastic algorithm show a more realistic random distribution of the seismic velocity, but the lateral continuity of horizons is not preserved (Fig. 2.6-B) in agreement with literature data (Trippetta et al., 2021).

Since the outcrop data clearly highlight a strong lateral continuity of strata, “Kriging (KG)" algorithm which has a deterministic approach is also tested. The Kriging results in a more reliable continuity of the strata with respect to SGS. However, it also tends to excessively smooth the results populating most of the cells with the mean seismic velocity value (Dubrule, 1998; Chambers et al., 2000, Trippetta et al., 2021) (Fig. 2.6-C).

To preserve the strata continuity, to achieve the minimum variance of error in modelling, and to avoid an excessive smoothing, “SGS Co-Kriging (SGS-CK)” algorithm is used (Vo Thanh and Lee, 2021). This algorithm uses data from correlated variables to improve the estimation of all variables (Myers 1984). Whit SGS-CK it is possible to insert a second interpolation variable (Manthena et al., 2009; Esmaeilzadeh et al., 2013). As second variable the constant

interval velocity values of the previously created 3D model with the UD algorithm is inserted. Fig. 2.6-D shows that SGS-CK algorithm satisfactory represents the heterogeneous distribution of seismic velocity within the 3D volume keeping at the same time the lateral continuity of the zones.

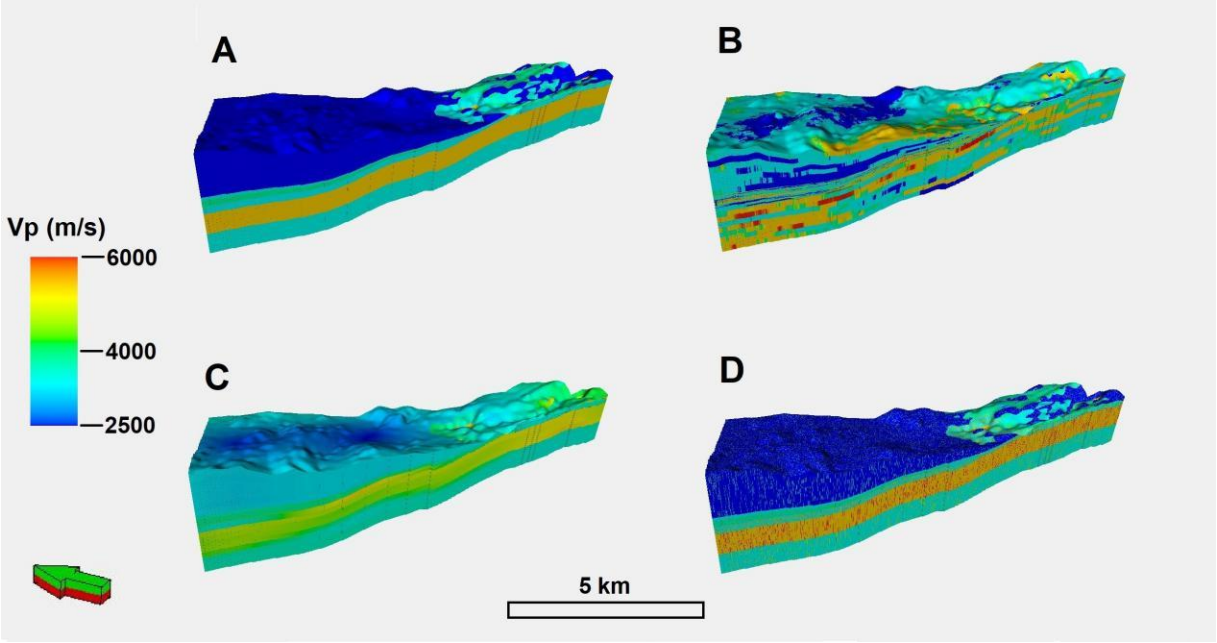

Fig.2.6. 3D seismic velocity models showing velocity values distributed through the volume with different algorithms of the Petrel property modelling tool. A) 3D seismic velocity model showing constant interval velocities carried out with the User Defined algorithm (UD). B) 3D seismic velocity model showing random velocities carried out with the SGS algorithm. C) 3D seismic velocity model showing smoothed velocities carried out with the KG algorithm. D) 3D seismic velocity model showing range interval velocities carried out with the SGS-CK algorithm.

2D section generation

A section (S) parallel to the x-direction of the model grid (Dashed yellow line in Fig. 2.1) is generated , with the Petrel calculator tool, using the following equation:

$$S = If\ (x = n, Velocity) \quad (1)$$

where n is the value of x along which is cut the section. The section is then converted into points and each point has three values, that represent the horizontal distance (x), the depth (z) and the Vp. Consequently, the points are extracted as a spreadsheet. The extracted spreadsheet is converted trough

Matlab (mark of Mathworks) into a seismic velocity values matrix. The 2D section (Fig. 2.7) is imported as input velocity matrix into Matlab in order to have a velocity model and consequently run the synthetic seismic section (De Franco et al., 2019). The velocity variation in this section clearly highlights the lateral continuity of the velocity property, together with a realistic variability between each zone.

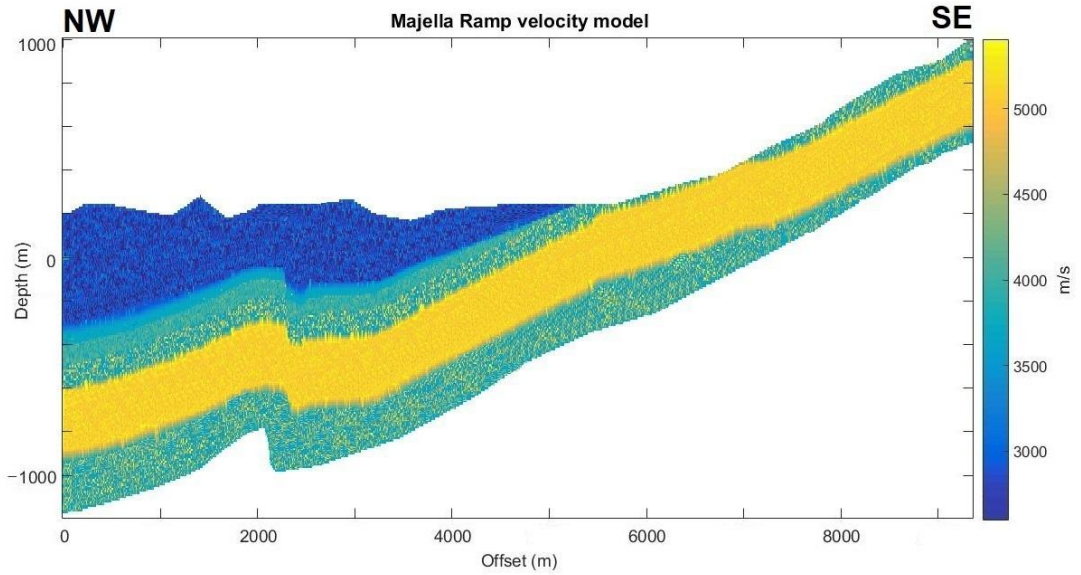

Fig. 2.7. 2D seismic velocity model extracted from Petrel and modeled in Matlab to run the synthetic seismic model.

2.6 Forward modelling

2.6.1-1D synthetic seismic forward modelling

Firstly a 1D synthetic seismic trace is calculated in Matlab (see Appendix A) to highlight the seismic response of the different facies starting with a simple model with layers characterized by variable thicknesses, densities and seismic velocities (Tab. 2.5).

As previously mentioned, a hypothetical well would encounter all the facies recognized from the thin section analysis, whilst the merging is related to the 2D-3D distribution of properties. Consequently, in the 1D synthetic seismic all the known facies are modeled (Fig. 2.5-A). Thus, from top to bottom the 1D model zones are the Flysch cover (FC), the Lithotamnion Limestones (LL), the

Hemipelagic Marls (HM), the Lepidocyclina Calcarenites 2 (both clean and bitumen saturated) (LP2), the Cherty marly Limestone (CM), the Lepidocyclina Calcarenites 1 (LP1), the Santo Spirito Formation 1 (SS1), the Santo Spirito Formation 2 (SS2), the Orfento Formation 1 (ORF1) and last Orfento Formation 2 (ORF2) (Fig. 2.5-A).

Age	Formation/Bolognano Fm. Members	Thickness m	Density kg/m^3	Vp m/s	AI MPa*s/m
Pliocene	**FC**	150	2000	2850	5,7
Tortonian-Messinian	**LL**	60	2200	3720	8,18
Serravalian-Langhian	**HM**	90	2290	3920	8,97
Burdigalian	**LP2** **LP2** bitumen-saturated	100 100	1870 2260	3630 4808	6,78 10,86
Aquitanian	**CM**	25	2280	3700	8,43
Rupelian-Chattian	**LP1**	50	1900	3650	6,93
Priabonian-Rupelian	**SS2**	150	2530	5300	13,41
Lutetian-Priabonian	**SS1**	250	2620	5500	14,41
Maastrichtian	**ORF2**	150	1950	3400	6,63
Campanian	**ORF1**	250	2070	4000	8,28

Tab 2.5. Petrophysical characteristics and thicknesses of the lithologies modeled in the 1D synthetic seismic forward modelling. In red petrophysical characteristics of the bitumen-saturated LP2 facies.

For each layer, the acoustic impedance (AI), the reflection coefficient (RC) through the normal incidence formula and the two-way travel time (TWT) are calculated.

A sampling interval of 0,002 seconds and a zero-phase Ricker wavelet with 40Hz frequency are set. Through the convolution of RC values with the reflectivity series it is possible to obtain a synthetic 1D seismogram based on clean rock properties.

To evaluate the influence of hydrocarbon, the 1D synthetic seismic trace is also calculated by using velocity measured on bitumen-saturated sample of the LP2 facies that represent the reservoir of the system and it is impregnated

in the field. These results are then compared with the 1D synthetic seismic trace calculated for clean rocks of the same facies.

Positive amplitudes occur at the transition from a medium with a lower value of AI to a higher value of AI one (Hilterman, 2001). In the clean LP synthetic seismogram (green synthetic seismogram in Fig. 2.8) positive amplitudes are registered at HM, CM SS2, SS1 and ORF1 tops whilst negative amplitudes characterize LP2, LP1 and ORF2 tops (blue and red symbols respectively in Fig. 2.8).

The comparison between the 1D synthetic seismic trace with LP2 bitumen-saturated (purple synthetic seismogram in Fig. 2.8) and clean (green synthetic seismogram in Fig. 2.8) shows evident differences. In particular, in the LP2 bitumen-saturated seismogram there is a polarity inversion and an amplitude variation at both LP2 top and bottom (yellow arrows in Fig. 2.8). Polarity switches from negative to positive at LP2 top with a 4% decrease in amplitude whilst a 11% increase in amplitude is registered at the LP2 bottom with a polarity switch from positive to negative. Moreover, the LP2 bottom is shifted upward of 0,07 seconds TWT when it is bitumen saturated. Consequently, also the underlying reflectors are shifted of the same value.

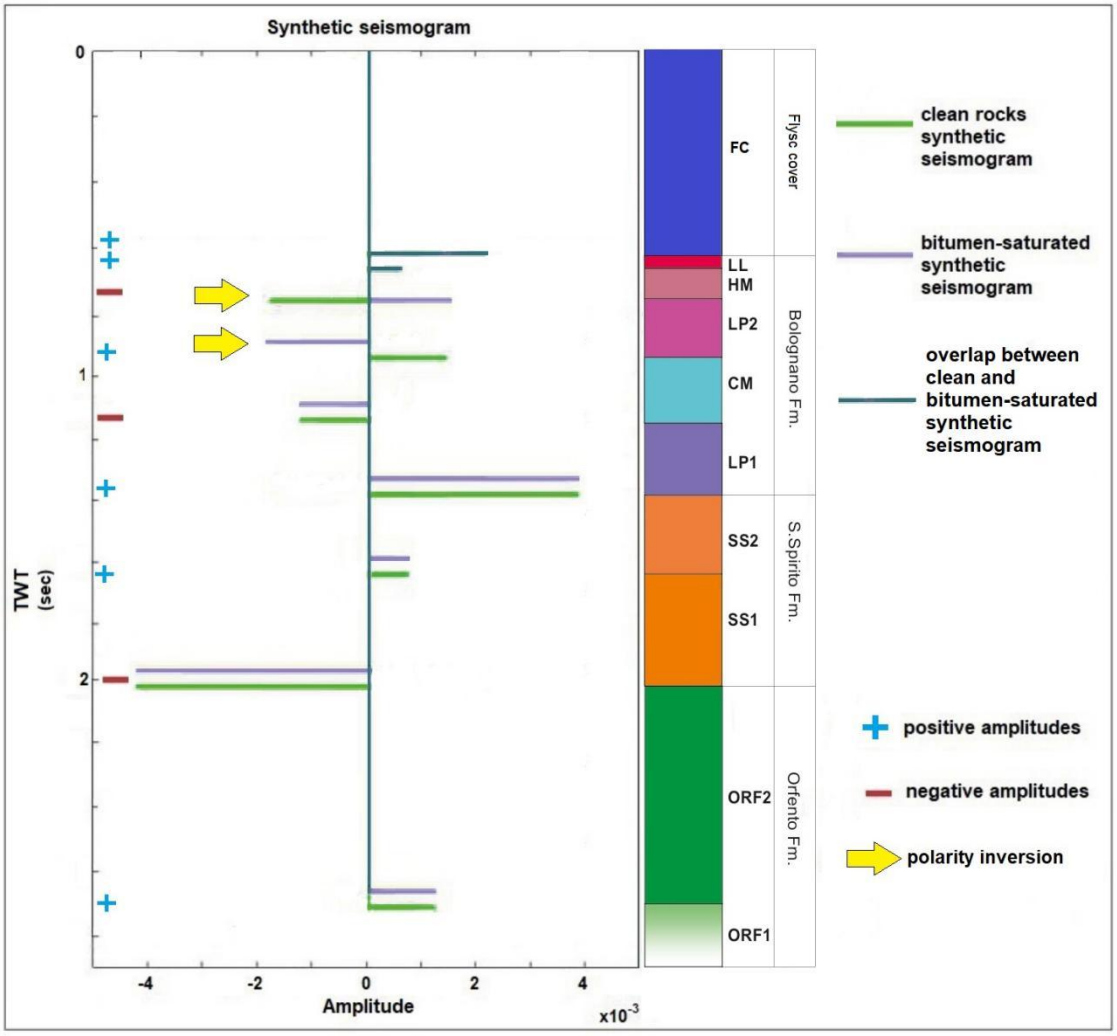

Fig.2.8 . Comparison between 1D synthetic seismic traces: in green are represented the seismic responses of the clean facies. In purple are represented the seismic responses with bitumen-saturated LP2. Blue and red symbols represent positive and negative amplitudes respectively; yellow arrows indicate the polarity inversions due to the bitumen presence.

2.6.2-2D synthetic seismic forward modelling

Modelling then proceedes to 2D synthetic seismic model. The synthetic seismic stack section is created using the CREWES consortium toolbox in Matlab, consisting in a collection of geophysical codes, which use a finite difference time domain method. The finite difference time domain method is a numerical method applicable to structurally complex media largely used in seismic for forward synthetic structural modelling (Moczo et al., 2007). Unlike ray tracing method in which significant amount of power scattered from the

surfaces is not considered (Wang et al., 2002), the finite difference time domain method calculates the total wave field.
The dimension of each cell in the velocity matrix in Matlab is set as 10x10m in x (dip) and z (depth) direction, following the 3D grid dimension (see par. 2.5).
The set variables includes: the input velocity matrix; the sample interval (2ms); the size of time step for modelling (0,5ms); the maximum time of the seismograms (2,5sec); the positions receivers in x and z; and the wavelet (40Hz). Moreover, a laplacian approximation – an operator used in the finite difference method to have a discretization of the grid points with neighbor points (Patra and Karttunen, 2006) – is used. A nine point laplacian approximation is adopted (Cho et al., 2007). At this stage it is possible to generate the output seismogram performing the convolution between AI and RC with the zero-phase Ricker wavelet resulting in a synthetic seismic stack section (De Franco et al., 2019).
2D synthetic seismic forward modelling is performed with sections extracted from both the petrophysical model characterized by constant interval velocities and from the petrophysical model characterized by heterogeneous interval velocities carried out with SGS-CK algorithm.

The synthetic 2D seismic stack section created from UD algorithm velocity (constant interval velocity), shows a very clear output characterized by continuous reflectors (Fig.2.9-A).

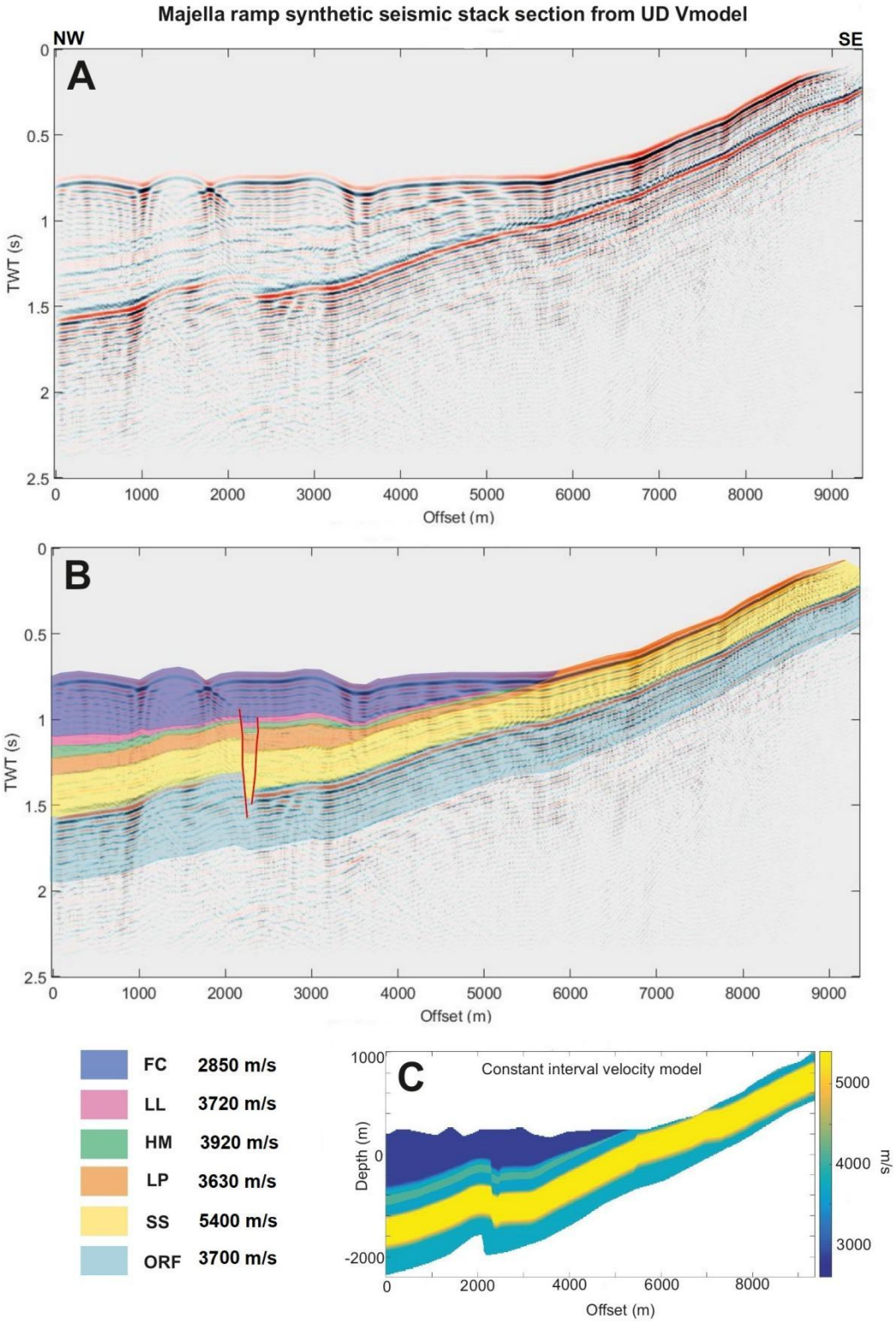

Fig. 2.9. A) 2D synthetic seismic stack section carried out from constant interval velocity model created with UD algorithm; B) seismic interpretation; C) velocity model used to perform the synthetic seismic model.

The flysch cover FC, closing in onlap on the slope at about 5800m offset and 0,75 TWT, is bounded at the top by a continuous, high-amplitude reflector. Below this reflector, there is a seismic facies of continuous low-amplitude reflectors, affected by signals which propagate downward and interpreted as diffraction hyperbolas generated by the slight elevations of the topographic surface, labeled in blue in Fig. 2.9-B. Underneath FC there is a medium amplitude reflector that corresponds to the top of LL. LL presents a small thickness (marked in pink in Fig. 2.9-B) inside which there are small disrupted low amplitude reflectors (Fig. 2.9-A). Below LL, also HM has a small thickness with a seismic facies of low-amplitude and slightly continuous reflectors (Fig. 2.9-A and marked in green in Fig. 2.9-B). Under the latter, LP is bounded by visible medium amplitude reflectors (marked in orange in Fig. 2.9-B) with a seismic facies characterized by quite continuous low amplitude reflectors. LP presents a thickness of 0.1 seconds TWT. The 0.4 seconds thickness (labeled in yellow in Fig. 2.9-B) below LP, correspond to SS, that is bounded at the top by a visible medium amplitude reflector and a seismic facies characterized by continuous reflectors. Below, SS is separated to ORF by a clear high amplitude reflector. The seismic facies marked in light blue in Fig. 2.9-B of high-amplitude continuous reflectors correspond to ORF which gradually disappears downwards for resolution reasons linked to the frequency. The interruption of the reflectors appreciable at an offset of 2200m and a depth ranging from 1sec TWT to 1.8sec TWT corresponds to a normal high angle fault system that is developed along the carbonate ramp.The unconformity visible at an offset ranging from 1500m to 2000m and at a depth from 1.6 to 1.7 TWT that breaks on the northernmost fault plane could be associated with an antiformal culmination or inherited horst The unconformity could be erroneously associated to the presence of a thrust because of the shape that the displacement of the normal fault system cause the reflectors to assume. However, the presence of a thrust is to be excluded because the compressive Majella deformation front is very distant from the modelled area and the slip plane of a thrust would be much deeper in this area that instead presents a multitude of normal faults at those depths. Despite the geodynamic context, the presence of a thrust can be excluded simply because in the volume

modeling, carried out through the study of horizons obtained from well data, we modeled normal faults.

The synthetic seismic stack section created from SGS-CK algorithm velocity model at heterogeneous velocity is more chaotic and shows a seismic signal with lower amplitudes, but closer to the output of real seismic surveys results (Fig. 2.10-A).

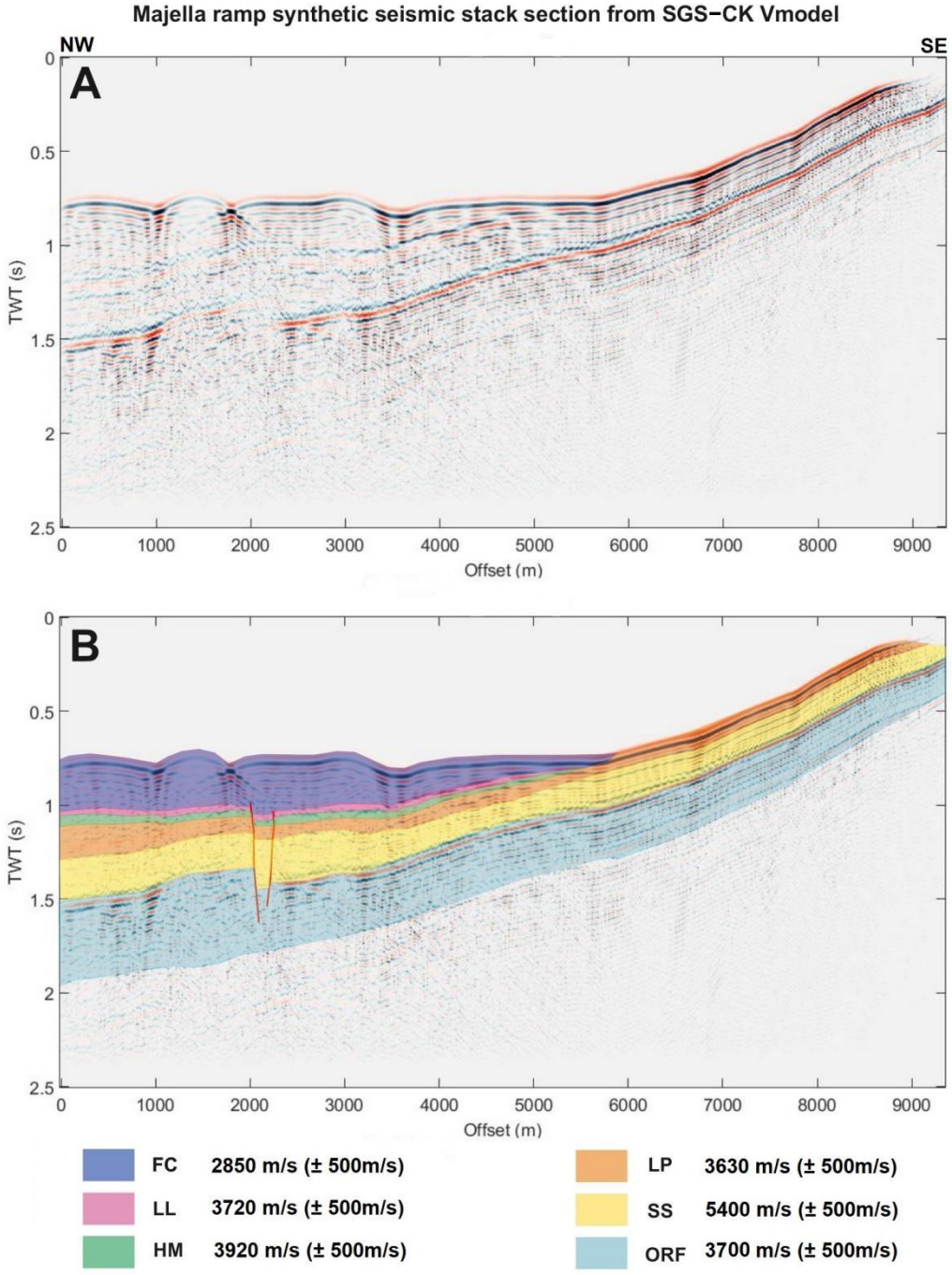

Fig.2.10. A) 2D synthetic seismic stack section carried out from heterogeneous velocity model created with SGS-CK algorithm; B) seismic interpretation.

The FC (blue thickness in Fig. 2.10-B) is characterized by a medium amplitude quite continuous reflectors seismic facies. Despite the lower resolution, the diffraction hyperbolas generated by the topographic surface are still visible. Below there is the thin LL, whose top is delimited by a disrupted medium-amplitude reflector. LL show a chaotic seismic facies but reflectors can be still followed in the seismic interpretation (marked in pink in Fig. 2.10-B). Also, in this section a thin and discontinuous seismic facies of disrupted reflectors can be observed for the HM facies (green area in Fig. 2.10-B). At its top is visible a very weak reflector. The facies below is not clearly visible but a discontinuous and low-amplitude seismic facies (in orange in Fig. 2.10-B) relate to LP, is delimited by reflectors with a low amplitude. The underlying SS is characterized by a chaotic seismic facies but its thickness (marked in yellow in Fig. 2.10-B) is clearly visible. ORF facies is bounded at its top by a strong high-amplitude continuous reflector and its seismic facies (in light blue in Fig. 2.10-B) is characterized by quite continuous reflectors of medium-high amplitude.

To evaluate the influence of hydrocarbon on the seismic response in 2D a comparison between the 2D synthetic seismic stack section – generated from the petrophysical model (see par.5) – and a synthetic seismic stack section – generated using velocities measured on bitumen-saturated LP facies then simulating thus the bitumen-saturated conditions of the LP facies in agreement with field observations – is carried out (Fig. 2.11).

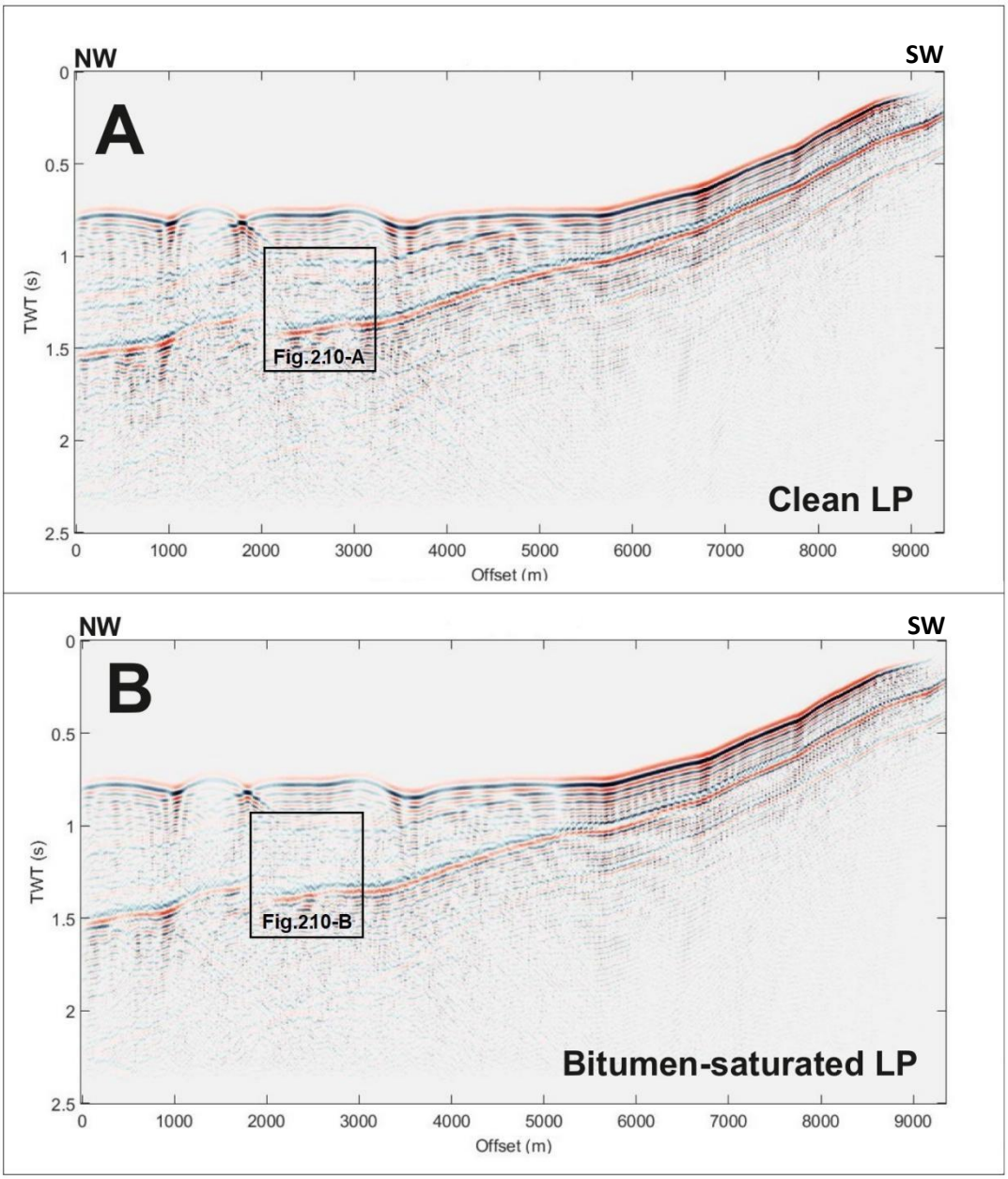

Fig. 2.11. Comparison between clean and bitumen saturated synthetic seismic stack sections. A) Synthetic seismic stack section with clean LP velocity values. B) Synthetic seismic stack section with bitumen-saturated LP velocity values. Insets are presented in Fig.2.13.

The comparison between the synthetic seismic stack section carried out with velocities measured on bitumen-saturated LP facies with those recorded on clean rocks of the LP facies, clearly shows again how the presence of bitumen affects the seismic response. Results shows that in presence of bitumen-saturated LP layer the reflectors are less marked and therefore have lower amplitudes with respect to clean LP. Moreover, the chaotic seismic facies of LP seem to become less clear when is bitumen-saturated causing low amplitude anomalies.

2.7 Discussions

2.7.1 Heterogeneity of the system

The density results show a relatively wide range of values, despite a quite constant grain density confirming a strong facies heterogeneity of the analyzed carbonate ramp system. The complex distribution of the petrophysical properties results in heterogeneities due to depositional processes (Agosta et al., 2019). The relative fluctuations of the sea level in time lead to sudden variations of the depositional environments such as that produced by the disintegration of the rudists platform margin in the Upper Cretaceous of the Orfento Fm., passing through another type of dismantled carbonate platform affected by calciturbiditic gravitational phenomena such as the nummulitic carbonate ramp represented by the Eocene Santo Spirito Fm., to arrive at the multitude of depositional environments created during the deposition of the members belonging to the Bolognano Fm. From the Rupelian a middle-to-outer ramp sedimentation is established that characterizes the LP1 facies. In the Aquitanian the system deepens creating relatively more distal deposits represented by the CM facies. In the Burdigalian the water thickness decreases again causing the sedimentation of the LP2 facies with parameters similar to LP1. Consequently between the Langhian and Serravalian the system deepens again as evidenced by the sedimentation of the HM facies and then returns, in the Tortonian, to mesophotic conditions of middle-distal ramp that allows the deposition of the LL facies. These abrupt sea-level changes have contributed in driving the strong facies heterogeneity given by different calcium carbonate-producing biota (Pomar and Kendall, 2008; Brandano et al., 2016).

Thus heterogeneity is due to the different structures and textures of each facies, to the micropaleontological components that characterize rocks with different grain sizes and different values of petrophysical characteristics (Brandano et al., 2020). As expected, the most porous facies are those with lower seismic velocity values (Trippetta et al., 2020). The resulting quite large range of velocity values complicates the resulting forward modelling in terms of seismic imaging (Jafarian et al., 2018; Grippa et al., 2019). Nevertheless,

these variations in measured petrophysical properties allow to better constrain the facies heterogeneity modelling.

The 3D petrophysical model with constant velocities carried out with the UD algorithm shows a good representation of the subsurface where modeled zones reflect the seismic velocity of the facies (Fig. 2.6-A). The resulting forward synthetic model shows a very clear output with continuous reflectors (Fig. 2.9) in agreement with previously published models (Mascolo and Lecomte, 2021). This persistent continuity of reflectors makes this output an excellent tool for the seismic interpretation with clearly detectable horizons if compared to a real seismic line. This aspect of synthetic seismic modeling results can provide great benefits, but these results are quite different with respect to outputs of current seismic surveys which usually appear chaotic especially in the carbonate realm (Eberli et al., 2004; Eberli and Betzler, 2019; Eloni et al., 2016; Sun et al., 2013) (Fig 2.12). In this work a SGS-CK algorithm is used for the reconstruction of the vertical and lateral distribution of the seismic velocities (Thanh et al., 2019; Trippetta et al., 2021) following to the realistic facies variations inferred from outcropping analogue observations and the petrophysical property measured in laboratory. The resulting synthetic seismic output becomes then closer to real geophysical surveys (Calderòn et al., 2000; Wang et al., 2020; Falivene et al., 2010) showing a more realistic background noise (Fig 2.12).

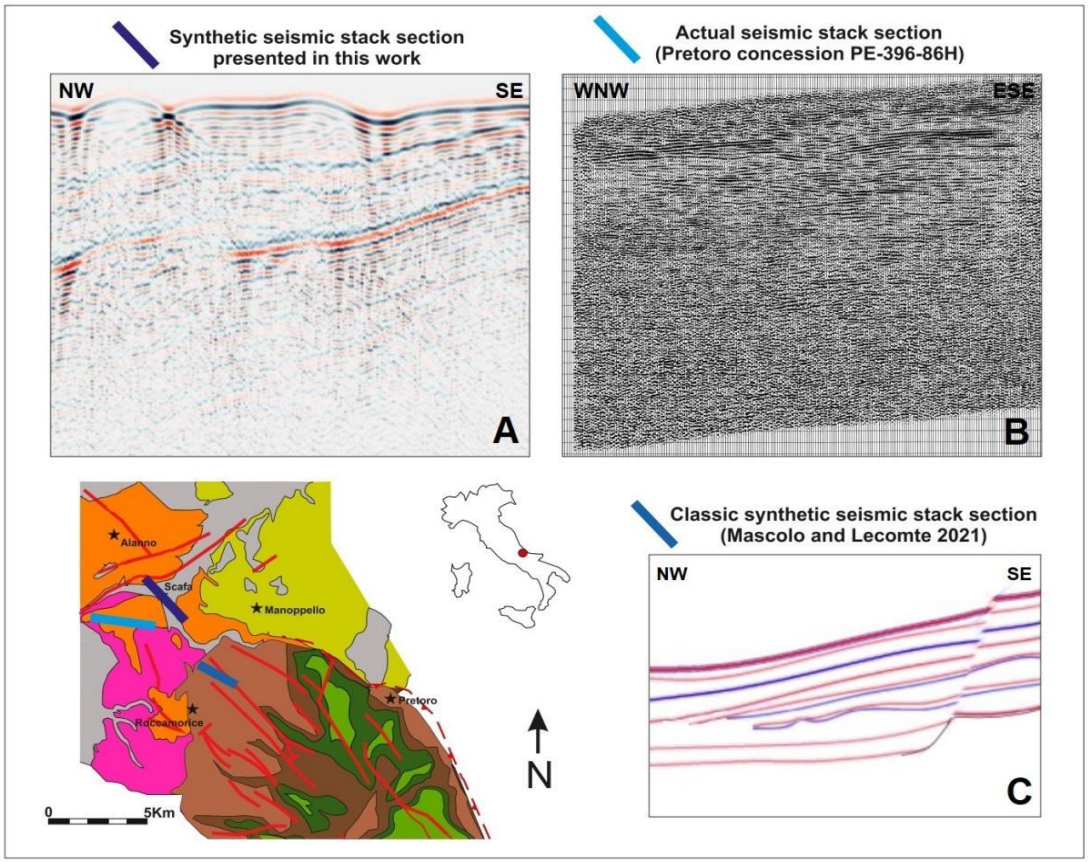

Fig.2.12. Comparison between the synthetic seismic stack section presented in this work (A) an actual seismic stack section (B) and a classic synthetic seismic stack section (C, modified after Mascolo and Lecomte, 2021). In the base map the traces of A in blue, B in light blue and C in cyan are reported.

However, noise is defined as random phenomenon caused by environmental or signal disturbances (Duchesne et al., 2006). On the contrary in our case the disturbance is not related to biases of the seismic signal or external disturbance. It, instead, reflects the response from a facies heterogeneity perturbed model and is therefore characteristic of the system (Sager et al., 2018). The output resulting from our forward modelling represents a perturbed signal affected by constructive and destructive interference generated by the variability of the physical properties of the model. However, similar disturbance in real seismic interpretations could be attributable and interpret as caused by environmental noise in terms of frequency, amplitude and complexity (Duchesne et al., 2006; De Franco et al., 2019). The synthetic nature of our seismic modelling guarantees a clean and environmental noise-free signal thus these perturbed signals provide additional information about

the carbonate ramp systems in agreement with data from carbonates (Wang et al., 2020; Falivene et al., 2010). Consequently, applying a noise reduction anisotropic diffusion filter that improves reflector appearance without creating or removing amplitudes (Iacopini and Butler, 2011) would cause a loss of precious information indicating the heterogeneity of the carbonate facies.

2.7.2 The Bitumen influence

The evaluation of the influence of bitumen on the seismic response of carbonate ramp systems has been assessed in this work both with 1D and 2D synthetic seismic models analysis. The 1D synthetic seismic model shows polarity reversals and amplitude increase at both LP2 top and bottom when passing from clean to bitumen-saturated conditions. This is due to the lower AI value with respect to HM and CM of clean LP2 that becomes larger of both HM and CM when LP2 is bitumen-saturated. Thus, by saturating the LP2 the initial negative polarity at the LP2 top and a positive polarity at the LP2 bottom turn into a positive and negative polarity, respectively. The bitumen-induced difference in AI between LP2 and HM at the top and between LP2 and CM at the bottom of LP2 layer is respectively lower (4% less) and larger (11% more) with respect to the AI recorded in absence of bitumen. This explains the decreased and increased amplitudes at the top and at the bottom of LP2, respectively, in agreement with the similar behavior observed on saturated layer in real seismic images acquired in the same area (Trippetta and Geremia, 2019). Similarly, in our 1D model, the amplitude of the LP2 bottom reflector, when it is bitumen-saturated, is enhanced becoming more detectable since the bitumen presence decreases porosity, increases the velocity, and increases density (Rabbani et al., 2016; Yuan et al., 2018; Trippetta and Geremia, 2019; Ruggieri and Trippetta, 2020). Furthermore, the 0,07 seconds TWT LP2 bottom upward-shift is related to the increase LP2 seismic velocity because of the bitumen presence and thus the P-wave crosses the layer in less time reducing its time-domain thickness. In the 2D model, LP2 and LP1 have been merged in a single layer, named LP, due to the small thickness and the scarce lateral continuity of the CM layer. The

comparison between the 2D synthetic seismic stack section generated in clean conditions and the same 2D section generated in bitumen-saturated conditions, shows that the presence of bitumen does not change the polarity (Fig. 2.13). Moreover, the amplitudes decrease at both LP top and bottom resulting in less visible reflectors (Fig. 2.13-B left inset).

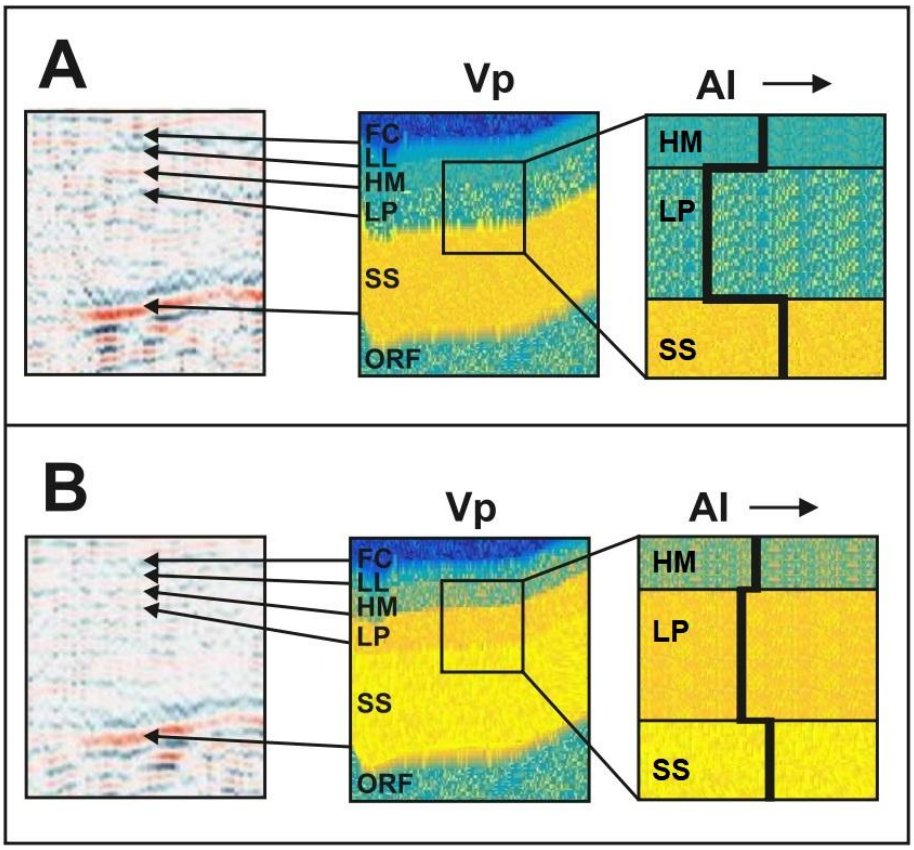

Fig.2.13. A) Analyzed portion of the synthetic seismic stack section (left inset) with clean LP velocity values (center inset) and interpretation of acoustic Impedance (AI) variation through the different layers (right inset) showing a sharp contrast in AI between LP and HM (above) and SS (below) B) Analyzed portion of the synthetic seismic stack section (left inset) with bitumen-saturated LP velocity values (center inset) and interpretation of acoustic Impedance (AI) variation through the different layers (right inset). The bitumen increases the LP value of AI leading to a lower AI contrast between HM and SS.

These two observations can appear to be in contradiction with 1D results, but they are not. In this case, the increase in AI value of the bitumen saturated LP causes a decrease in acoustic impedance contrast at both the top and at bottom of the layer (Fig. 2.13-B center inset). The variation in AI is not enough to overcome the differences in AI with HM and SS and consequently the polarity at both top and bottom of LP does not change. Thus, the presence of

bitumen in LP (in orange in Fig. 2.13-B) leads to a lower horizons seismic amplitude (Trippetta and Geremia, 2019) resulting in less clear reflections (Fig. 2.13).

The 1D and the 2D models on the bitumen influence in the seismic response demonstrate how AI contrasts and thus their reflections are closely dependent on the seismic parameters of the media in contact with the bitumen-saturated layer (Zhang et al., 2007). If the presence of bitumen increases the AI difference, as observed in the 1D model, amplitudes increase, polarity may change, and reflectors became more evident. On the contrary, if bitumen affects the seismic parameters reducing the AI gap of rocks in contact, as it happens in the 2D model, the amplitudes dramatically decrease and reflectors are less visible.

Chapter 3: Synthetic seismic forward modelling as a tool to assess the seismic signature of carbonate-bearing fault zones: control on parameters in forward modelling

The results of this work has been submitted to the special issue “Petroleum geology of Middle East, Eastern Mediterranean, and Adjacent regions” of the Journal of Asian Earth Sciences published by Elsevier.

3.1 Forward modelling of a buried normal fault system

This third chapter addresses the modelling of fault zones present in carbonate systems such as the Majella Massif. The objective is twofold. A first goal consists in the quantification of the control that can be exerted in modifying the petrophysical characteristics and thus the elastic parameters of carbonate rocks in forward seismic modelling. A second objective is related to the possibility of analyze the seismic response related to the presence of fault zones. As discussed in Chapter 2, geophysical surveys performed in the carbonate realm are difficult to interpret because of their strong facies heterogeneity (Palaz and Marfurt, 1997). Further complications are then related to the presence of faults. Fault systems can have very different effects on the seismic response of carbonate rocks (Faleide et al., 2021; Botter et al., 2014). Carbonate-bearing faults are typified by one or more slip zones (the fault core) surrounded by a region characterized by fractures, joints, veins, shear bands or compaction bands (damage zone) (Caine et al., 1996, Trippetta et al., 2017). The transition from the fault core to the adjacent zone is less well investigated (Hadizadeh and Rutter, 1983) in particular in carbonate rocks (Billi et al, 2003).

Deformation in the damage zone decreases moving from the fault core toward the undeformed host rocks (Caine et al., 1996; Trippetta et al., 2017). The lithologies belonging to both the fault core and to the damage zone have different petrophysical characteristics compared to the protolith – in which the fault is nucleated – because they experienced stress and strain caused by the movement of the fault (Wibberley et al., 2008; Michie, 2015; Michie and Haines, 2016). These dynamics cause the fault rocks to have different elastic parameters from the protolith and thus different acoustic impedance contrasts from the surrounding rocks (Faleide et al., 2021; Botter et al., 2014). Fault zones from shallow-water carbonate rocks are characterized by variable brittle deformation modes (Caine et al., 1996; Antonellini et al., 2008; Trippetta et al., 2017). In this lithologies faulting is often associated with opening mode fractures (Mollema and Antonellini, 1999). However, carbonate dissolution allows development of pressure solution and the subsequent shearing of solution surfaces (Antonellini et al., 2008; Mollema and Antonellini, 1996;

Storti et al., 2007; Rustichelli et al., 2012). These processes combined with microcracking and grain comminution (Heap, 2015; Wong and Baud, 2009; Baud et al., 2004) lead to the formation of compaction bands which more often occurs in sandstones (Fortin et al., 2006).

3.2 Geological setting and background

As for Chapter 2, also this work focuses on shallow-water carbonate rocks of the Majella Massif (see par. 2.2) (Fig.3.1) but instead of modelling the seismic response of facies heterogeneity, in this chapter we analyze the seismic response of fault systems set up in the same geological context. The Majella Massif allows the synthetic seismic modelling of carbonate-bearing faults. In this chapter we therefore study the same lithologies but driven by different objectives. The considered formations are the Campanian-Maastrichtian Orfento Formation, the Paleocene to Eocene Santo Spirito Formation and the Oligo-Miocenic Bolognano Formation with its five informal members (Brandano et al., 2016) (see par. 2.2). Faults analyzed in this work outcrop on the east, central and north-west sectors of the Majella Mountain. The first analyzed fault in this work is the Piano delle Cappelle fault (named PDC in Fig. 3.1), which is almost 8km long and is hosted in the Bolognano Formation striking N150° and dipping 60° to SW. This is a regional fault with a normal component of slip (Tomassetti et al, 2021) and with a total displacement of 240 m.

The second investigated fault which has a length of 1 km, is hosted in the Bolognano Formation and outcrops close to Decontra village striking N200° and dipping 56° to S (named DE LP in Fig. 3.1). Kinematic indicators highlight oblique-normal faulting slip with a total displacement ranging from tens of centimeters to one meter.

The third examined fault with a length of 750 m, is hosted in the Orfento Formation and outcrops close to Pennapiedimonte village striking N40° and dipping 90° (named PE ORF in Fig. 3.1). Kinematic indicators, such as slickenlines and mineral (calcite) growth, show that the PE ORF fault is

characterized by transtentional slip with a total displacement from few centimeters to tens of centimeters.

The last analyzed fault with a length of 2 km, is hosted in the Santo Spirito Formation and outcrops in the Santo Spirito Valley striking N220° and dipping 68° to SW (Fig. 3.1 FS SS) Kinematic indicators mainly suggest normal slip with a total displacement up to few meters.

In the sampling areas, all analyzed faults are intraformational and therefore displacements do not cause structural contacts between different formations. Geodynamic processes characterized by the extension in the Majella area has been disputed in literature and consequently also the presumed times of the activity of these faults: Miocene-Early Pliocene by Scisciani et al. (2002), Quaternary by Ghisetti and Vezzani (2002) and pre-Quaternary by Pizzi et al. (2010) (Rustichelli et al., 2016; Agosta and Aydin, 2006).

From the field analysis, the studied faults show a classic architecture pattern characterized by a centimetric fault core, where most of the deformation accumulates, and a damage zone of a few tens of meters where deformation gradually decreases towards the host rock (Caine et al., 1996; Fossen, 2016). It is worth noting that in the damage zone of the analyzed faults no major fracture systems are appreciable.

On the other hand, several faults outcropping in the Majella area are characterized by high fracturing with an increased porosity in the damage zone (Marchegiani et al., 2006; Pisani et al., 2021), allowing fluid flow (Romano et al., 2017) especially in the Bolognano Formation outcrops of the Roman Quarry close to Lettomanoppello village (Fig.1) (Agosta et al., 2009; Giorgioni et al., 2009; Volatili et al., 2019; Zambrano et al., 2021).

Independently with respect to the architecture of the fault zone (fractured or not) field observations and literature data (Agosta et al., 2009; Giorgioni et al., 2009; Romano et al., 2020) suggest that, on average, the damage zones of all the faults outcropping in the Majella area show a maximum width of 50 meters; beyond that distance no deformations are generally appreciable at the outcrop scale.

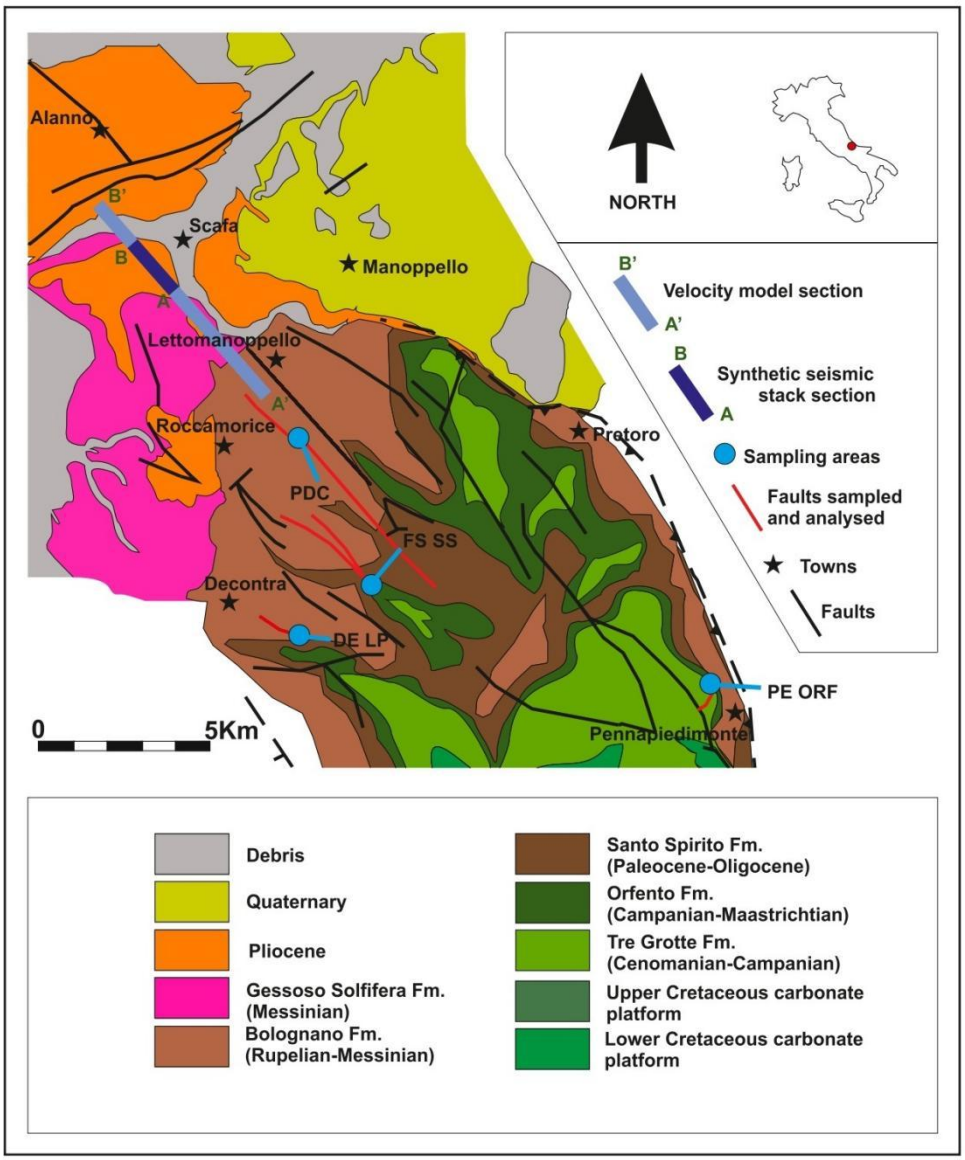

Fig. 3.1. Simplified geological sketch of the Majella Mountain (modified after Vecsei and Sanders, 1999 and Trippetta et al. 2021) showing sampling areas, sampled faults (drawn in red), and location of the velocity model section and the synthetic seismic stack section, modeled in this work and represented with a light blue line and a blue line, respectively.

3.3 Methods

3.3.1 Field work and sampling

Samples were collected from the Piano delle Cappelle fault (Fig. 3.2A), from the fault outcropping close to Decontra village (Fig. 3.2C), from the fault close to Pennapiedimonte village (Fig. 3.2D) and from the fault outcropping in the Santo Spirito Valley (Fig. 3.2B).

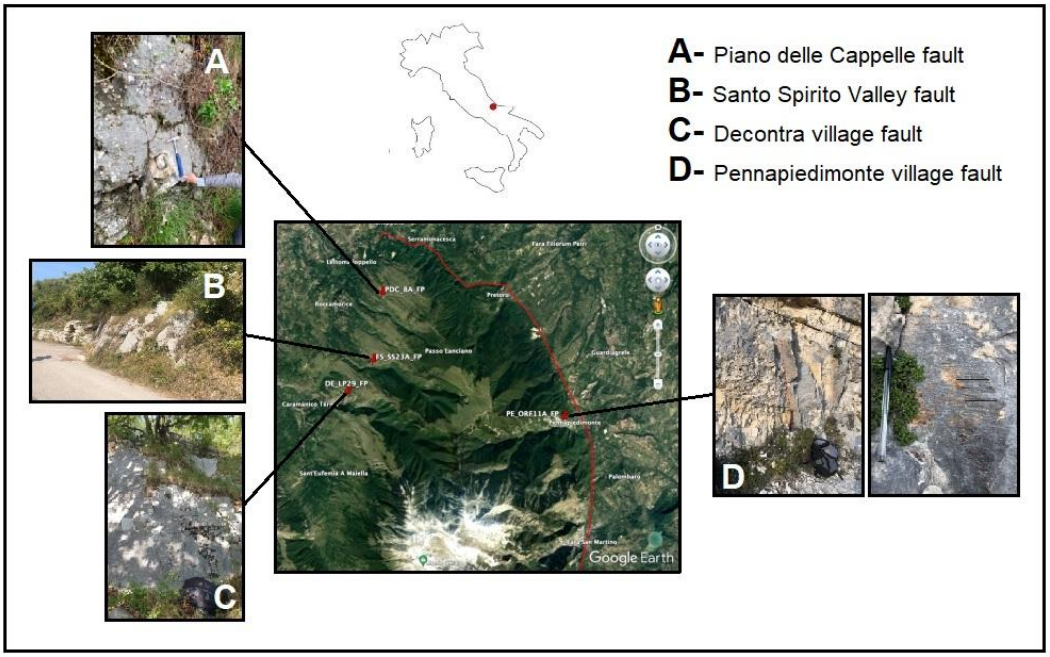

Fig. 3.2. Locations of collected samples and outcrops view.

For each fault we collected samples at progressive distances from the fault plane to assess the petrophysical variations moving away from the slip plane. All samples collected and analyzed were grouped according to 3 end members categories: samples belonging to the fault core, to the damage zone, and to the undeformed host rock. From observations in the field the damage zone has a maximum width of 50 meters as beyond that distance no deformations are appreciable (Fig. 3.3).

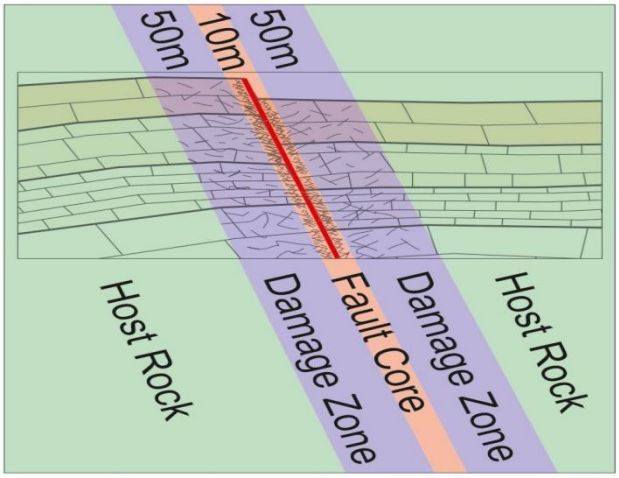

Fig. 3.3. Representative sketch of the width of the damage zone observed in the field. Host rock samples were collected beyond 50m from the fault plane (in the green area of the sketch). Damage zone samples were collected within 50m from the fault plane (in the blue area of the sketch). Samples related to the fault core were collected on the slip plane and within a few meters from it (in the red area of the sketch).

3.3.2 Laboratory measurements

The methodologies used to measure the petrophysical characteristics of the samples are the same as those used in Chapter 2 (see par. 2.3.2). Density and porosity are measured using Anton Paar Ultra-pyc 5000 helium pycnometer.

P-wave velocity (Vp) and S-wave velocity (Vs) are measured by using the USB 8M 8-channels ultrasonic device generator developed by Mistras Eurosonic and piezoelectric transducers.

3.4 Samples characterization

Thin section analysis.

We produced a set of 34 thin sections from samples collected during the field work to recognize microstructures related to faulting (Fig.3.4). The thin sections analysis confirms the field observations, i.e. that the studied faults show a classical model characterized by a fault core and a damage zone

where microstructures generated by the stress are present, and an unformed host rock that does not show tectonic-related microstructures.

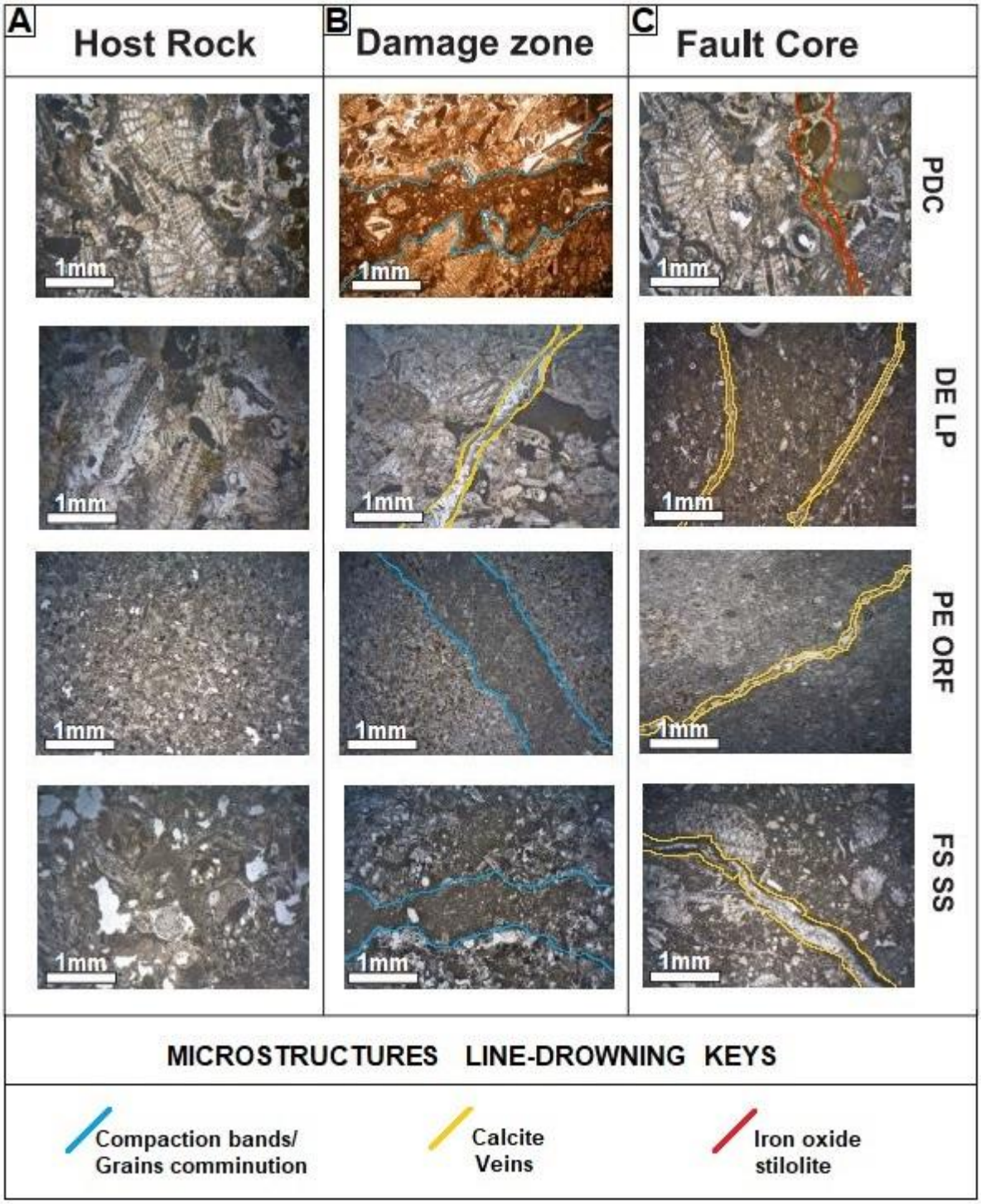

Fig.3.4. Sampled fault rocks in thin sections belonging to the different faults analyzed (PDC, DE LP, PE ORF, FS SS). A) Host rocks samples. B) Damage zone samples. C) Fault core samples. The coloured line drowning represents some relevant microstructural observations. Scale bar = 1mm.

Host rock

Samples belonging to the host rock appear undeformed and therefore reflect the characteristics of the protolith in which the fault developed (Fig.3.4A).

The host rock samples belong to the Lepidocyclina Limestone informal member of the Bolognano Formation, the Orfento Formation and the Santo Spirito Formation. The Lepidocyclina Limestone consists of a rudstone calcarenite according to the classification of Dunham (1962) and Embry and Klovan (1971), whose major components are large benthic foraminifera such as lepidocyclinids, rotalids and fragments of non-articulate red algae (PDC and DE LP faults).

The Orfento Formation is a fine grainstone to packstone with clasts dimension up to 2mm top in size composed of a bioclastic mince, poorly cemented and friable (Dunham, 1962; Embry and Klovan, 1971) (PE ORF fault).

The Santo Spirito Formation corresponds to a grainstone to rudstone (Dunham, 1962; Embry and Klovan, 1971) with large benthic foraminifera. Foraminifera mostly include nummulitids and rotalides (FS SS fault).

Damage zone

Damage zone samples were collected in an area extending from the fault core to a distance of about 50 meters from it. These samples typically show structures with thickness around 1mm characterized by clear evidence of grain breakage and grain comminution with no detectable shear offset (Fig.3.4B). These structures can be referred to compaction bands causing a reduction in porosity, grain fracture and dissolution at grain contact points (cyan line drowning in Fig.3.4B) (Mollema and Antonellini, 1996; Baud et al., 2004; Fortin et al., 2006; Storti et al., 2007; Wong and Baud, 2009; Fossen et al., 2011; Heap et al., 2015).

Fault core

This fault-portion, which accommodated most of the slip, consists of a narrow zone, (~1–15cm thick). Samples of the fault core show brittle deformation structures, represented by fractures where calcite and/or iron oxides (Fig.3.4C) re-precipitated. Veins, filled with calcite crystals, are often present probably originated from fractures in which circulating fluids deposit crystalline material inside (Fossen, 2016). The microscopic morphology of calcite crystals shows a blocky texture characterized by equidimensional and randomly oriented

crystals (yellow line drowning in Fig.3.4B-C). These are syntaxial veins in which the filler minerals are of the same type as the minerals in the host rock (Bons et al., 2012; Fossen, 2016).

Density

Densities [kg/m^3]		Fault portion		
		HR	**DZ**	**FC**
Fault	PDC	2020	2250	2660
	PE ORF	2125	2240	2260
	FS SS	2090	2300	2670
	DE LP	2280	2530	2580
	Mean	**2129**	**2330**	**2542**

Tab. 3.1. Bulk density values (expressed in kg/m^3) of the lithologies sampled and characterized belonging to the fault core (FC), damage zone (DZ) and host rock (HR).

The density measurements show differences between the samples collected on the fault core, on the damage zone and on the host rock (Tab. 3.1). The firsts have higher density values respect to the samples of the damage zone which in turn have higher density values than samples of the host rock.
The standard error is in the range 0,03g/cm^3 to 0,07g/cm^3.

Porosity

The effective and total porosities were then calculated and are reported in Tab. 3.2.

Porosity [%] total - effective		Fault portion		
		HR	**DZ**	**FC**
Fault	PDC	25,93 - 24,84	16,97 - 16,43	0,73 - 0,73
	PE ORF	22,50 - 22,19	21,63 - 21,11	18,45 - 18,20
	FS SS	22,63 - 22,58	15,54 - 14,96	3,38 - 2,93
	DE LP	20,34 - 20,01	8,90 - 7,83	5,23 - 2,18
	Mean	**22,85 - 22,4**	**15,76 - 15,08**	**6,95 - 6,01**

Tab. 3.2. Total and effective porosity values (expressed in %) of the lithologies sampled and characterized belonging to the fault core (FC), damage zone (DZ) and host rock (HR).

Samples related to the fault core show very low porosity values which goes even below the 1%. The rocks belonging to the damage zone have a higher porosity compared to samples collected on the fault core but it is still lower than the host rock samples. Host rock related samples show porosities higher than 20% being almost entirely effective porosities. The standard error is within 2%.

Seismic velocity

Measured seismic velocities of the sampled lithologies at ambient pressure, are reported in Tab. 3.3.

Seismic velocity [m/s] Vp - Vs - Vp/Vs		Fault portion		
		HR	**DZ**	**FC**
Fault	PDC	4120 - 2520 - 1,63	4410 - 2620 - 1,68	5890 - 3240 - 1,81
	PE ORF	3730 - 2250 - 1,66	3860 - 2350 - 1,64	3950 - 2420 - 1,64
	FS SS	3820 - 2350 - 1,63	4470 - 2670 - 1,68	5440 - 3120 - 1,74
	DE LP	3780 - 2270 - 1,66	4730 - 2770 - 1,71	5400 - 3080 - 1,75
	Mean	**3862 - 2347 - 1,65**	**4367 - 2602 - 1,68**	**5170 - 2965 - 1,73**

Tab. 3.3. Seismic velocity of P and S waves values (expressed in m/s) and Vp/Vs ratio of the lithologies sampled and characterized belonging to the fault core (FC), damage zone (DZ) and host rock (HR).

The lithologies characterized by higher seismic velocities are the rocks sampled on the fault core. Lower seismic velocities are measured for the rocks related to the damage zone region. As expected, due to the higher porosity, the lithologies with the lowest seismic velocities values are those belonging to host rock.

The standard error is between 2,2% and 4%.

3.5 Model building

The petrophysical model used for the analysis of the seismic response of fault zones is that related to Chapter 2 (see par. 2.5) in which the petrophysical

characteristics of rocks adjacent to the two south-east dipping normal faults present below the flysch cover are modified.

In fact, in the velocity model extract from Petrel and imported into Matlab – used as a starting point for this forward modelling exercise – two south-east dipping normal faults are visible. They affect the entire carbonate succession excluding the flysch cover (Fig.3.5-A). These high-angle faults observed in the section are steep as most normal faults at intermediate and shallow depths in sedimentary basins (Faleide et al., 2021).

The modelling is focused on this fault system. The section extracted for this model is parallel to the model section presented in Chapter 2 and located at a distance of 100 m to the NE from that in Fig. 2.7 (see par. 2.5). The extracted section is cut to zoom in on the fault zone. The vertical exaggeration is removed to get a sharper view of the fault system analyzed (Fig. 3.5-B). A crucial step includes the modification of Vp values in the damage zone region. Finally, the velocity model is run in Matlab to perform the synthetic seismic fault model.

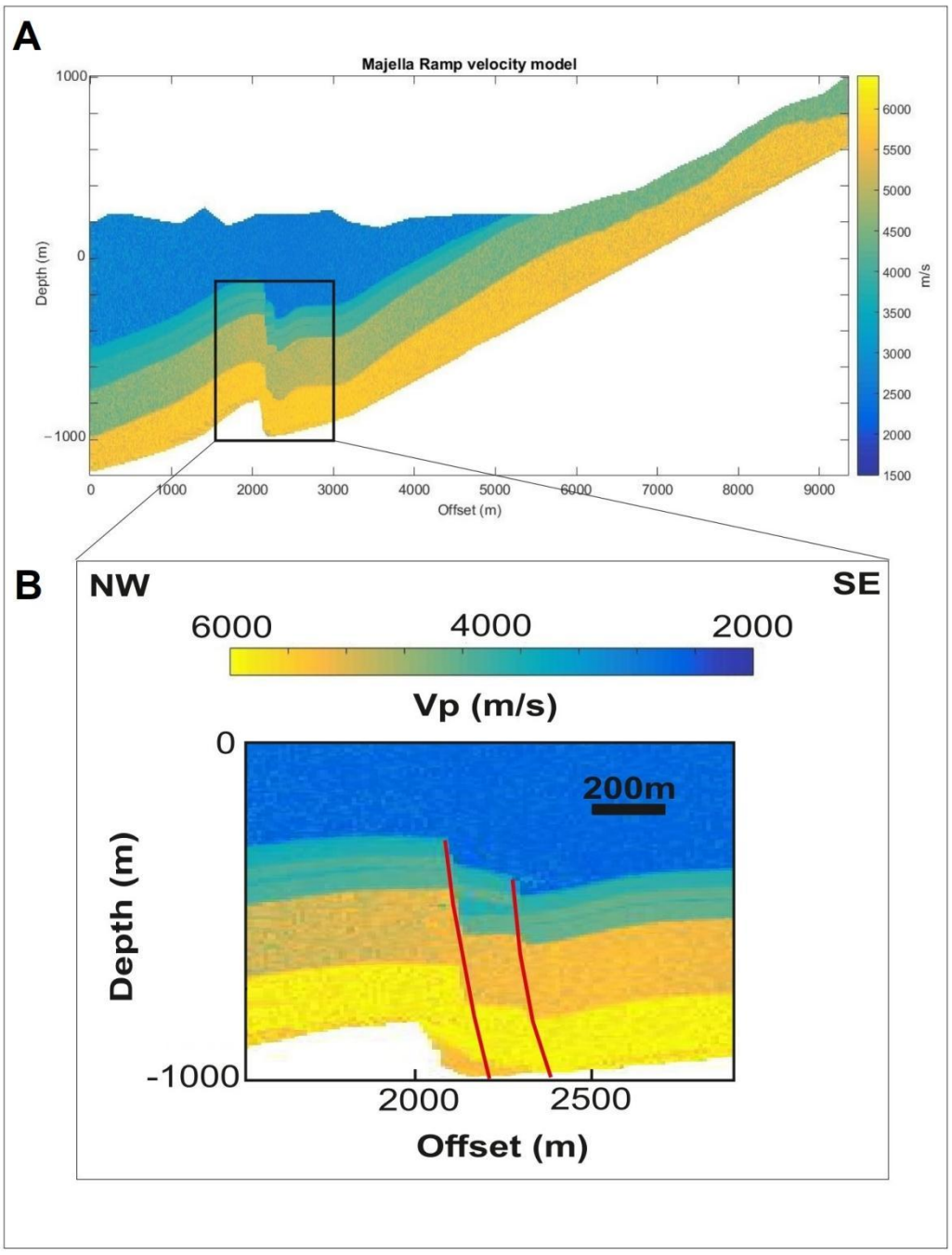

Fig.3.5. A) 2D seismic velocity model extracted from the Petrel and modeled in Matlab. The trace of the section is reported in Fig.3.1. B) Detail on the fault system without verical exaggeration.

3.6 Forward modelling

3.6.1 Fault zone synthetic seismic forward modelling

It is well known in the literature that fault activity influences the petrophysical characteristics of the surrounding rocks as confirmed by the petrophysical characterization previously illustrated. The resulting behaviour, also in terms of fluid transport properties (Romano et al., 2017; Pisani et al., 2021) can be twofold (Caine, 1996; Fossen, 2016; Michie, 2015; Michie and Haines, 2016; Antonellini et al., 2008; Trippetta et al., 2017; Mollema and Antonellini, 1996; Storti et al., 2007; Rustichelli et al., 2012; Heap et al., 2015; Wong and Baud, 2009; Baud et al., 2004) within the study area (Marchegiani et al., 2006; Agosta et al., 2009; Giorgioni et al., 2009; Volatili et al., 2019; Zambrano et al., 2021). On one hand the movement along fault can cause fracturing with consequent increase of porosity and decrease of P-wave seismic velocity (Fig.3.6A). On the other hand, sliding on the fault plane can cause compaction and thus a decrease in porosity and consequent increase in P-wave seismic velocity (Fig.3.6B) being this typically the case for porous host rocks as observed during the field work previously illustrated.

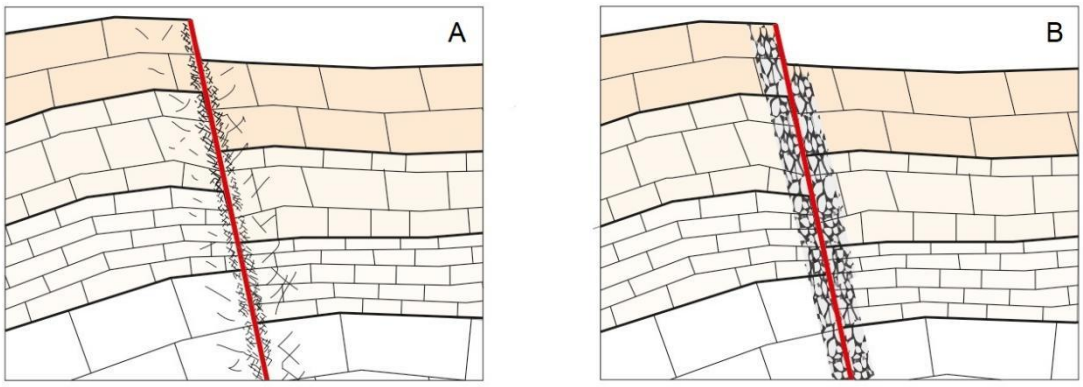

Fig.3.6. Sketch showing the two end members in accord with the movement along fault affects the petrophysical characteristics of the rocks of the damage zone (not to scale). A) Fault causing fracturing, increased porosity and decreased of P-wave velocity. B) Fault causing compaction, decreased porosity, increased P-wave velocity.

This twofold behavior is confirmed by field and laboratory data collected on faults outcropping in the Majella area where example of both increased porosity (Agosta et al., 2019, Romano et al., 2020) and decreased porosity (this work) damage zones have been observed and characterized. Following these two end members, we carried out in Matlab a fault zone synthetic seismic forward modeling of the two high angle south-east dipping normal faults buried below a flysch cover that affect the sampled carbonate ramp lithologies shown Fig.3.5 decreasing or increasing the Vp values of the damage zone with respect to the Vp values of the host rock. Thus, the first scenario (S1) simulates a damage zone characterized by opening fractures causing increased porosity whilst the second scenario (S2) simulates a damage zone characterized by the presence of compaction bands or mineralized veins both causing decreased porosity as confirmed by the thin section analysis.

Laboratory measurements of actual fault rocks showed that porosity strongly decreases from the host rock (~23%) to the fault core (~4%), however, its thickness is on the order of a few centimeters and thus not visible at seismic scale. On the other hand, the thicker damage zone still shows a decreased porosity (~17%) with respect to the host rock. For samples collected in the field a change in rock porosity of ~6% (23% in the host rock and 17 in the damage zone), corresponds to a change in P-wave velocity of about 500 m/s (Fig.3.7). These data are also in agreement with literature data collected on the same lithologies (Ruggieri and Trippetta, 2020).

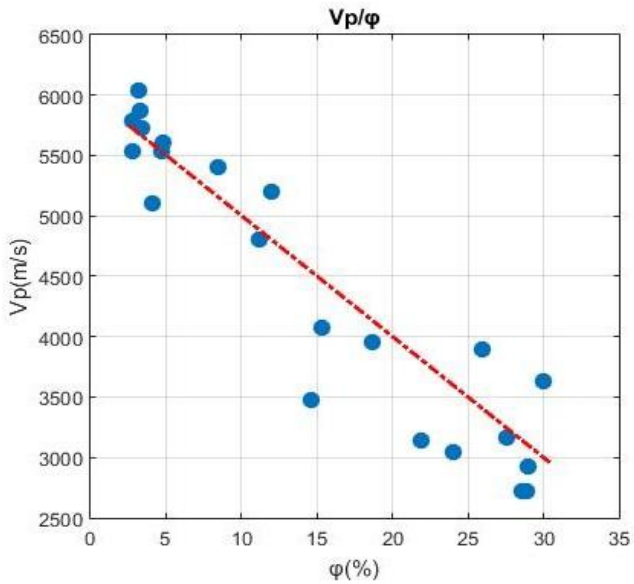

Fig.3.7. P-wave velocity versus porosity plot (Vp/φ) showing how porosity varies at different seismic velocities through samples collected in the field and measured in laboratory.

Following the petrophysical results, we built two velocity models (Fig.3.8). In S1 (Fig.3.8A) the damage zone is modeled with Vp values 500m/s lower, thus with a 5% higher porosity, for each geologic layer if compared to the starting velocity model, shown in Fig.5 which can be considered as the undeformed host rock. In S2 the damage zone is modeled with increased Vp values of 1000m/s (Fig.3.8B), thus a 10% lower porosity with respect to the host rock. We voluntarily doubled the increased seismic velocity values with respect to measured data to enhance the differences in the seismic response. The modeled damage zone is 50 meters wide from each fault plane in agreement with the field observations.

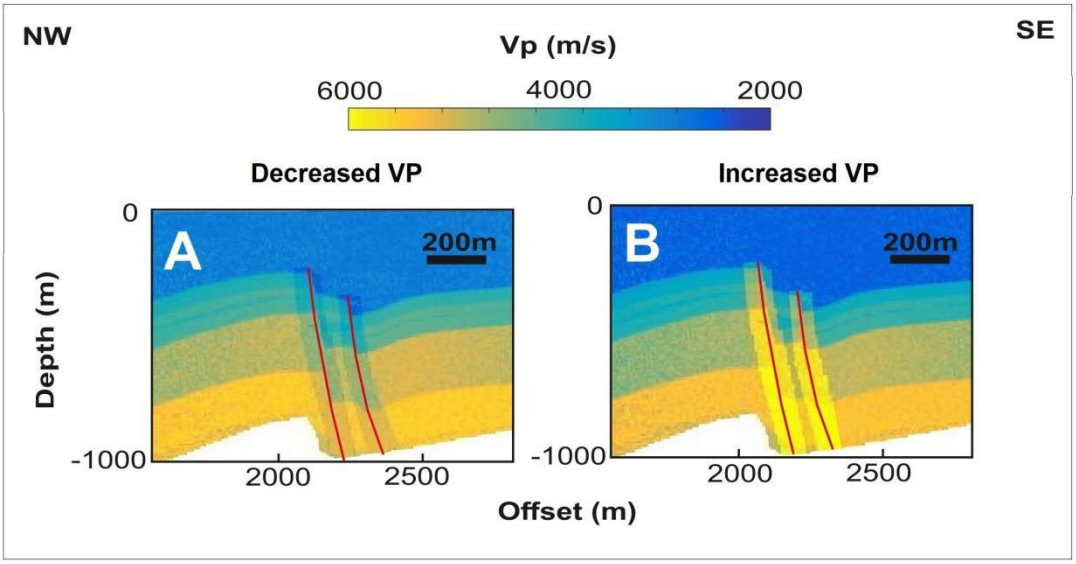

Fig.3.8. Velocity models with modified Vp values of the damage zone region. A) Damage zone modeled with decreased Vp values with respect to the host rock (S1). B) Damage zone modeled with increased Vp values with respect to the host rock (S2).

Then, we run the synthetic seismic models with the CREWES consortium toolbox in Matlab, obtaining two different seismic responses (Fig.3.9). The set variables were: the input velocity matrix derived from the velocity models; the sample interval (2ms); the size of the time step for modeling (0,5ms); the maximum time of the seismograms (2,5sec); the positions receivers in x and z; and the wavelet (40Hz). Then, it was possible to generate the seismic stack sections (Fig.3.9) through the convolution between AI and RC with the zero-phase Ricker wavelet (De Franco et al., 2019; Tomassi et al., 2022).

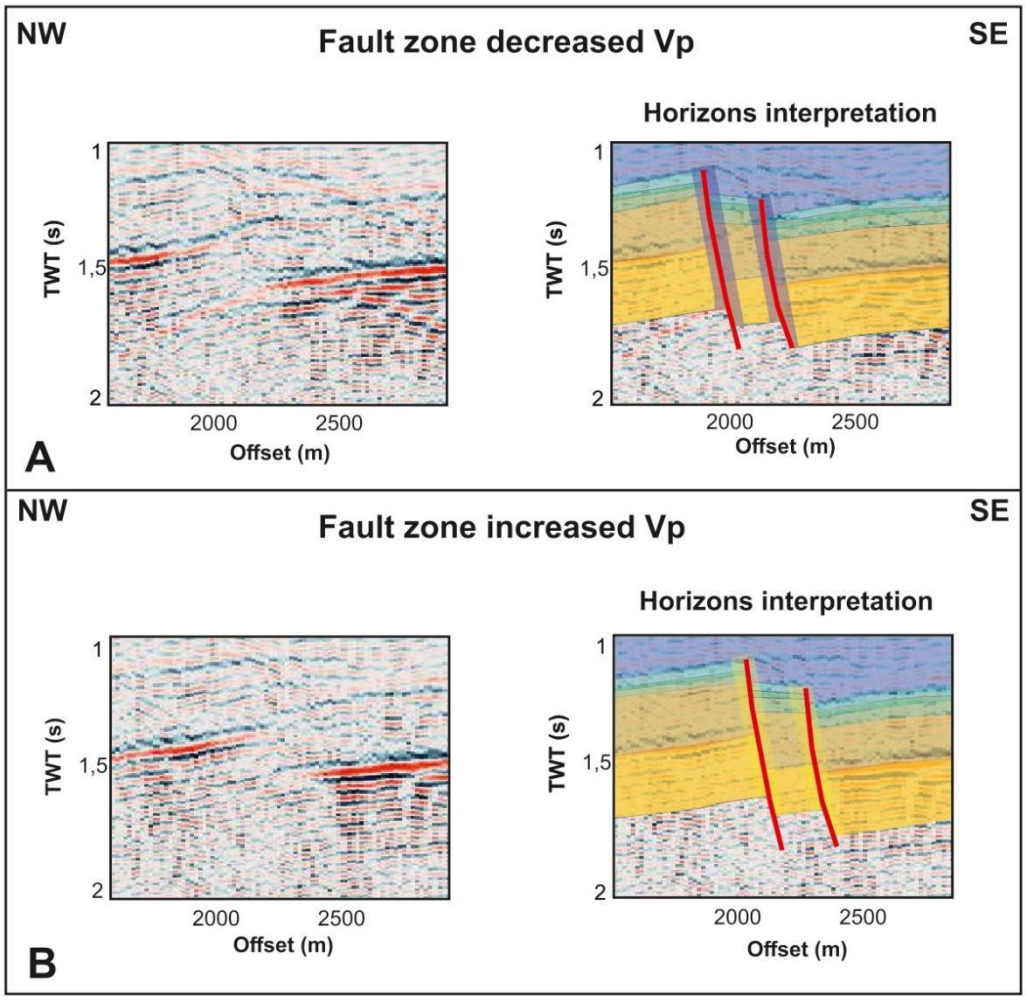

Fig. 3.9. Synthetic seismic models and horizons interpretations of the modeled fault zone carried out in Matlab from the velocity models shown in Fig.3.8. A) S1 synthetic seismic model. B) S2 synthetic seismic model.

Comparing the two seismic stack sections different in seismic responses characterize the the two fault zones (Fig. 3.9). If Vp is reduced (S1, Fig. 3.9A) the damage zone seismic response is affected by the presence of marked diffraction hyperbolas causing a difficult interpretation of seismic lines. If Vp is increased (S2, Fig.3.9B) the damage zone seismic response does not show appreciable artifacts even if the simulated increase in Vp has been doubled with respect to what is reasonably expected.

3.6.2 Sensitivity test

In order to determine if factors, that produce the diffraction hyperbolas in fault zones seismic images, are only due to the variation in petrophysical characteristics, we performed a sensitivity test. In particular, we assessed the influence of factors, such as the fault geometry, on the seismic response by varying the thickness of the damage zone and the dip of the fault.

The sensitivity test is carried out in Matlab starting from the same synthetic seismic forward model performed in the Majella area . This allows to include the facies heterogeneities during the analysis of the seismic response of carbonate-bearing fault zones.

Thus, velocity models were built (Fig.3.10-3.11-3.12) to run the synthetic seismic using the CREWES consortium toolbox (Tomassi et al., 2022). In the host rock, velocities were distributed with a value of 5000 m/s (±500m/s to represent heterogeneity), simulating carbonates, whilst for the cap rock, which overlay the buried fault zone, we adopted a value of 2000m/s (±500 m/s) simulating flysch formations.

Following the two end members scenarios S1 and S2 at increased or decreased porosity of the damage zone - due to opening fractures causing increased porosity or presence of compaction bands and mineralized veins causing decreased porosity - we modeled the seismic velocities in the damage zone with values from 4000m/s to 4500 m/s in one scenario (Fig.3.10A-3.11A-3.12A) and with Vp values range between 5500m/s and 6500m/s in the other scenario (Fig.3.10B-3.11B-3.12B).

Firstly, we simulated a 50m-thick high angle (70°) fault zone based on field observation and thus a similar situation as that observed in Majella (Fig.3.10).

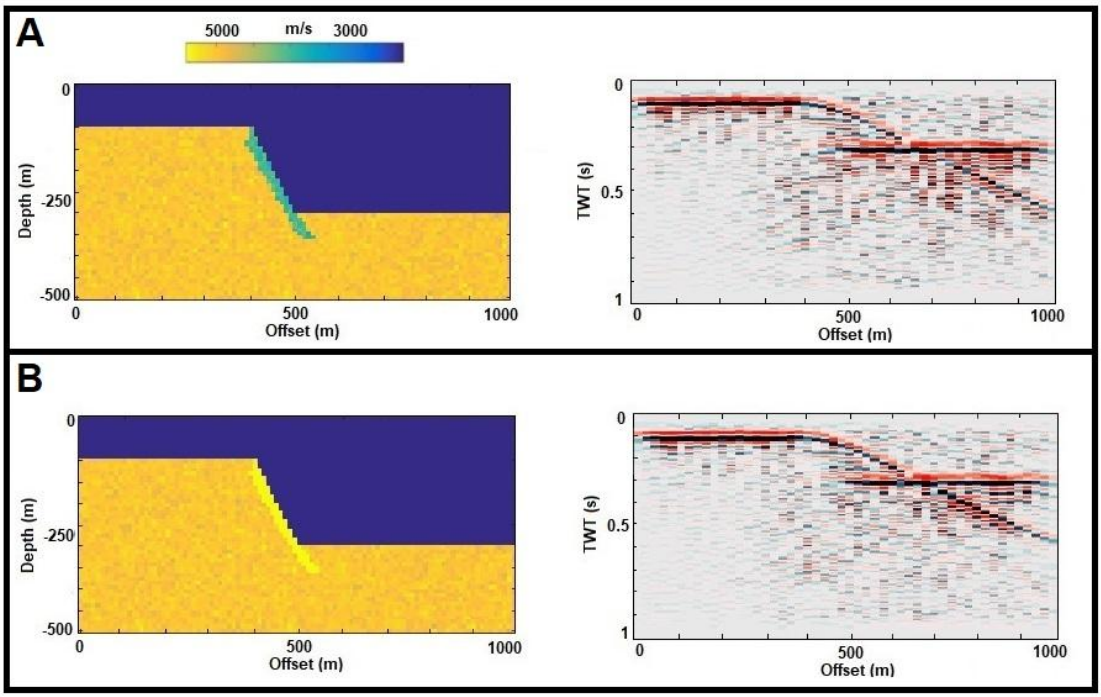

Fig.3.10. Velocity models and related synthetic seismic stack sections created in Matlab to simulate 70° dipping fault zones with a 50m wide damage zone. A) Fault zone modeled at lower seismic velocities than host rock, simulating an increased porosity damage zone (S1). B) Fault zone modeled at higher seismic velocities than host rock, simulating a decreased porosity damage zone (S2).

In the seismic response of S1 the increased porosity in the damage zone (Fig.3.10A) is characterized by marked diffraction hyperbolas in the fault region appearing more chaotic than the seismic response of S2 (Fig.3.10B). In S2 the seismic image is less characterized by large amplitude variations or by particular artifacts.

These results reflect the outcome of the fault zone synthetic seismic forward modeling of the two high angle south-east dipping normal faults affecting the Majella carbonate ramp. Thus, to evaluate what drives the generation of diffraction hyperbolas in the fault zone we considered the influence of the damage zone width on the seismic response. Consequently, we expanded the damage zone thickness in the model up to a thickness of 100m maintaining a high angle geometry with dip of 70° (Fig.3.11).

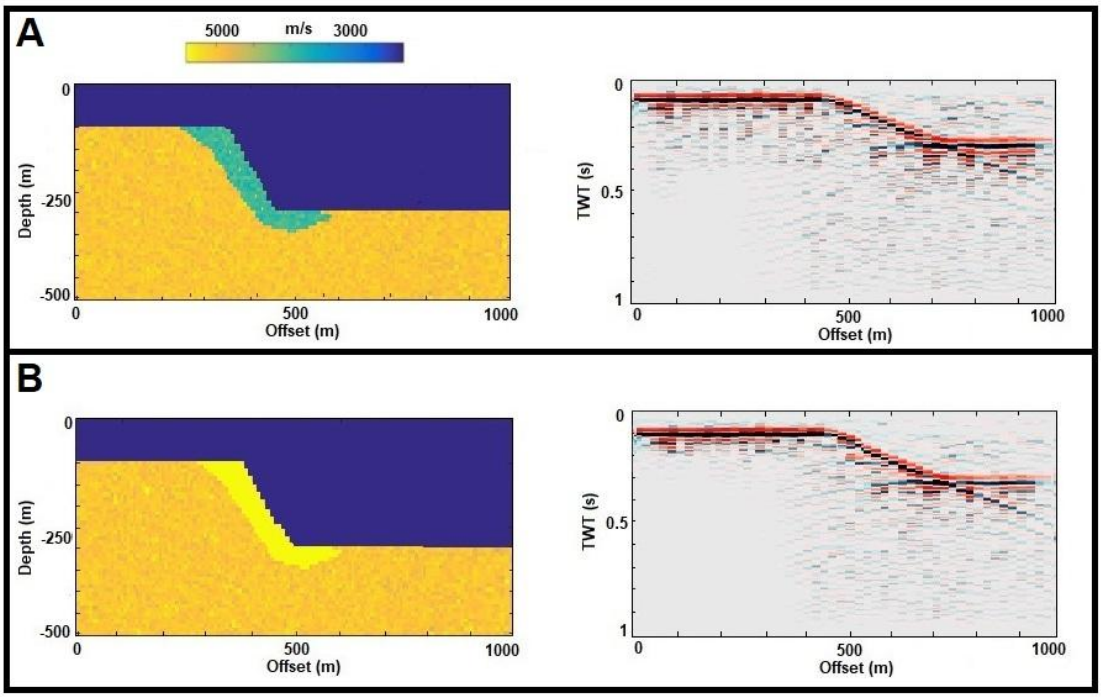

Fig.3.11. Velocity models and related synthetic seismic stack sections created in Matlab to simulate 70° dipping fault zones with a 100m wide damage zone. A) S1 fault zone model. B) S2 fault zone model.

The seismic response of the 100m wide damage zone shows in general less artifacts and less pronounced diffraction hyperbolas than the seismic response of the 50m wide damage zone.

However, the seismic response of S1 with 100m-width damage zone (Fig.3.11A), is still characterized by diffraction hyperbolas in the fault region even if there are fewer artifacts with respect to Fig.3.10. On the contrary, the seismic response of S2 (Fig.3.11B) is almost free of hyperbolas if compared to 100m-width damage zone S1.

To evaluate the influence of the dip in the generation of diffraction hyperbolas, we modeled lower-angle fault dipping 25° maintaining the narrow damage zone width of 50m (Fig.3.12) since maximum hyperbolas are generated by minimum damage zone thickness as shown in Fig.3.10 and Fig.3.11.

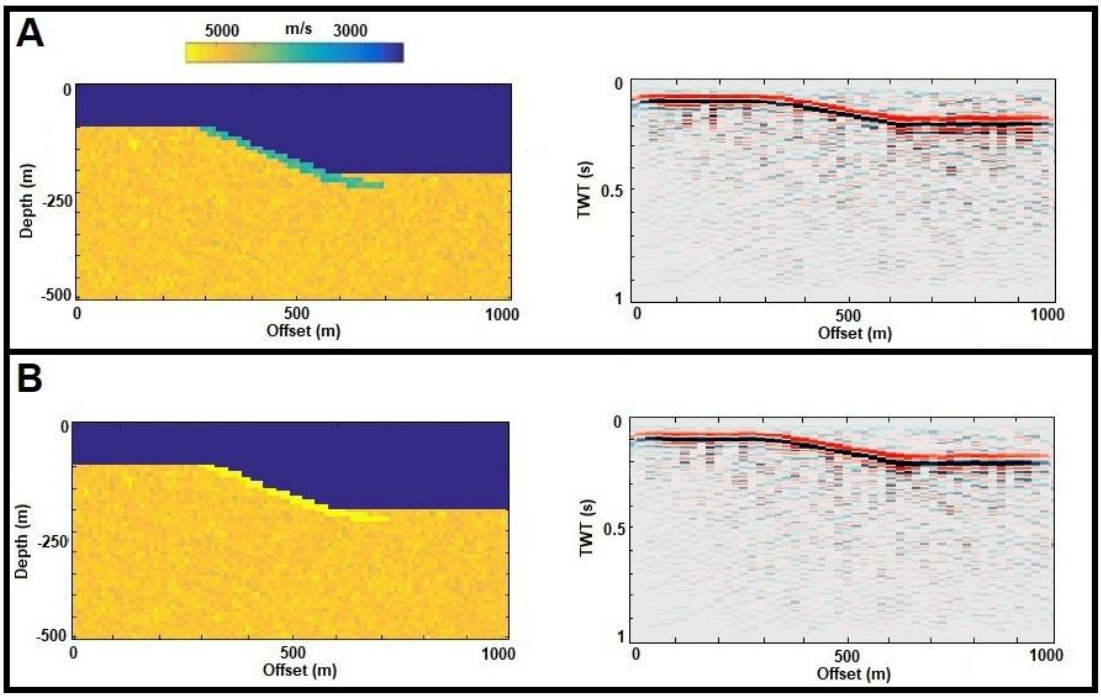

Fig.3.12. Velocity models and related synthetic seismic stack sections created in Matlab to simulate 25° dipping fault zones with a 50m wide damage zone. A) S1 fault zone model. B) S2 fault zone model.

The seismic response of the model with the 25° dipping fault zone changes considerably. These seismic images are almost free of diffraction hyperbolas with respect to those related to the 70° dipping fault zones. In particular, the S1 25° dipping fault model (Fig.3.12A) shows very weak diffraction hyperbolas compared to the S2 model (Fig.3.12B). Consequently, the latter seismic image is the one with the fewest diffraction hyperbolas of the whole sensitivity test.

3.7 Discussions

The modification of the petrophysical characteristics of the rocks in the damage zone region, according to the two simulated end members, highlights large differences in the seismic response. Marked diffraction hyperbolas in the seismic response of the fault zone area are generated simulating decreased seismic velocity values with respect to the host rock. This scenario simulates an increased porosity due to the presence of fractures and secondary porosity

(S1) (Giles, 1987) and it is in very well agreement with observation from GPR (Ercoli et al. 2013). On the contrary, the opposite scenario (S2 with increased Vp values) shows less marked diffraction hyperbolas in the seismic response. Lithologies outcropping in the study area show in thin section the presence of compaction bands and mineralized veins in samples belonging to the fault core and the damage zone, leading thus to a decreasing in porosity relatively to the host rock (Rustichelli et al., 2012; Mollema and Antonellini, 1996). The presence of compaction bands is also supported by the petrophysical measurements carried out on the samples, collected on the fault core and on the damage zone, which show higher seismic velocity and lower porosity than the samples collected in the host rock. Both methods highlight a decrease in the porosity and increase in seismic velocity values moving from the host rock toward the fault core. (Mollema and Antonellini, 1996; Storti et al., 2007; Fossen et al., 2011; Rustichelli et al., 2012) because rocks analyzed in this work show sorting and porosity values very similar to those of fine to coarse sandstone allowing the development of compaction bands caused by sliding along the fault plane, intensive microcracking and grain comminution (Heap et al., 2015; Baud et al., 2004; Baud et al., 2009; Rustichelli et al., 2012; Cilona et al., 2012).

Consequently, the model that most faithfully represents the Majella Massif fault zone, addressed in this study, is the one represented in Fig.3.9B. The diffraction hyperbolas in the faults studied in the Majella Massif are almost not visible in the modeling because in this situation compaction bands develop (S2) decreasing the porosity values of the damage zone with respect to the host rock, while the marked diffraction hyperbolas are generated modeling an increased porosity of the damage zone (S1, Fig.3.9A).

To understand the influence of faults geometric factors on the generation of the diffraction hyperbolas in the seismic response, we performed the sensitivity test. Results of the sensitivity test show that the diffraction hyperbolas are increasingly pronounced for faults with an increasing angle from 25° to 70°. The test also showed that as the width of the damage zone increases, the hyperbolas gradually become less pronounced. As a result, the hyperbolas almost disappear for a damage zone thicker than 100m.

In literature several works highlighted diffraction hyperbolas due to the presence of a fault zone in shallow context where the main driving factor has been related to the geometry of the faults (Liner and Liner 1997; Bano et al., 2002; Pauselli et al. 2010; Ercoli et al. 2012; Ercoli et al. 2013). Considering the Majella Massif case study, the fault geometry alone is not enough to generate diffraction hyperbolas. In order to be generated the marked diffraction hyperbolas, the fault damage zone must be characterized by an increase in porosity of with respect to the host rock, regardless of fault geometry.

The results of this work confirm that diffraction hyperbolas can preferably be generated in the seismic response of shallow fault systems (Pauselli et al. 2010; Ercoli et al. 2012; Ercoli et al. 2013) where the low stress allows the fractures to remain open. This would also explain why faults are generally almost free of hyperbolas at depth. On one hand faults could be characterized by a lower-porosity damage zone due to the observed deformation mechanisms. On the other hand, also in fractured damage zones, the large stress acting at depth would close the fractures decreasing the porosity of the damage zone.

Conclusions

Based on the obtained results, the following considerations can be addressed:
1) The first chapter discusses how the Porto Badisco calcarenite represents an useful case study for 3D facies heterogeneity modelling and for the investigation of carbonate ramp systems petrophysical characteristics.
-Facies heterogeneity is confirmed by outcrop analysis as well as petrophysical characteristics measured in laboratory. Density, porosity and seismic velocity show wide ranges of values among the different recognized facies.
-Porosity is measured through three different methodologies with different results. Porosity analysis through point counting strongly underestimates values up to 25%. Porosity results obtained by image analysis match those of the helium pycnometer measurements. Helium pycnometer is to be considered as the best methodology to estimate a petrophysical characteristic such as porosity. In fact, it carries out the measurement on a volume of sample instead of a surface as for the other methodologies used in this work. From the correlation between the porosity measurements obtained with the pycnometer and those of seismic velocity performed with the oscilloscope, it is clear that the less porous facies are those with higher values of seismic velocity. Laboratory data allowed to create two 2D petrophysical models, one of the porosity and one of seismic velocity which characterize the different facies of the carbonate ramp. These models clearly show that heterogeneity is not only lithological but reflects as well the physic features of rocks.
-Field data used as input in Petrel allowed to create a 3D facies heterogeneity model of the Porto Badisco calcarenite Chattian ramp. TGSim stochastic method algorithm used for modelling fits with the facies heterogeneity observed in the field and in the facies analysis on thin sections. TGSim respect the facies distribution on the depositional profile reproducing the facies transitions from the inner to the outer ramp and validating the depositional model. Thus, TGSim resulted in an adequate and powerful tool

for modelling facies heterogeneity and their relationships in the architecture of carbonate systems.

2) In the second chapter there is a multiple combination of field sampling, laboratory measurements, structural modelling with Petrel, property modelling and synthetic seismic modelling, to obtain the seismic images related to the carbonate ramp system both clean and bitumen-saturated characterized by facies heterogeneity. Based on the obtained results, the following considerations can be addressed:

-The SGS-CK algorithm give the best results for the distribution of seismic velocity data through the model since it realistically distributes the petrophysical properties of the system preserving a reliable lateral continuity of the layers. It is shown again that the best algorithm to distribute petrophysical data such as seismic velocity through a digital model has a stochastic method reflecting the petrophysical characteristics of the facies constituting the carbonate ramp system.

-Forward modelling based on facies heterogeneity results in a disturbed synthetic seismic output closer to real seismic section. The disturbance is not proper noise but it is due to the heterogeneity of the carbonate system. The presented model evidences a possible pitfall in the interpretation of seismic sections. In fact, it is here demonstrated that a genuine heterogeneous facies model exhibits a complex and perturbed reflection pattern that can be erroneously interpret as related to the presence of noise in the data. Thus, it should pay attention in field data and seismic section processing, and in particular in the excessive filter application that could lead to a loss in information on the genuine architecture of the reservoirs as in the classical synthetic seismic models.

-The presence of bitumen in rocks exerts a significant role on seismic response. Modeled bitumen-saturated rocks cause variation in both amplitudes and polarity with a complex reflectivity pattern. These variations can result in increase or decrease of the amplitude of the reflectors depending on the seismic properties of the lithologies that are in contact with the bitumen-saturated layers.

3)In the third chapter, a synthetic seismic forward modelling of a fault zone developed in a carbonate ramp is performed. Results show that the

deformation behavior of carbonates along fault zones affects the seismic parameters of the rocks.

- Carbonate fault rocks of the Majella area show a deformation behavior similar to sandstone and mainly generate compaction bands instead of fracturing due to the high primary porosity. The fractures in the fault core are filled with reprecipitated calcite. These phenomena lead to a progressive decrease in porosity and an increase in seismic velocities approaching fault planes.
- The modification of the petrophysical characteristics of carbonate-bearing fault systems in synthetic seismic forward modeling leads to a different behavior if seismic velocity and porosity values can be increased or decreased in the damage zone. Damage zones with higher porosity and a lower seismic velocity with respect to the host rock, are characterized by seismic response with important diffraction hyperbolas. Damage zones with a lower porosity are characterized by a seismic response almost free of hyperbolas. The latter modeling reflects the behavior of the faults that are the subject of this study.
- The presence of marked diffraction hyperbolas in the seismic response of a fault zone is strictly related to the increase in porosity of the damage zone rocks with respect to the host rock. Other factors, such as the geometry of the fault or the thickness of the damage zone, can only enhance or reduce the hyperbolas. Thus, the weak presence of hyperbolas in seismic images can be interpreted as the evidence of a relatively lower porosity damage zone with respect to the host rock.

4) Digital modelling of carbonate rocks leads to new insights for understanding these systems. Seismic response of carbonate successions varies due to facies heterogeneity, hydrocarbon presence and fault systems. Using the consequent modifications on the petrophysical parameters as input data is at the heart of forward modelling.

This thesis highlights how such a tool can give very important clues in investigating subsurface especially in the complex carbonate realm. The correct interpretation of subsurface structure belonging to this carbonate-realm has an increasing importance due to the possibility of using these reservoirs for many energy purposes.

Appendix A

1D synthetic seismic forward model script

```
clc
clear all
%define the layer thickness
L = [60 90 100 25 50 150 250 250 250];
%define the denities of layer
 ro = [2200 2290 1870 2280 1900 2530 2620 1950 2070];
%define the velocities of layer

 pvel = [3720 3920 3630 3700 3650 5000 5400 3700 4200];
% calculate the acoustic impedance for each layer
IA1 = (ro(1)*pvel(1));
IA2 = (ro(2)*pvel(2));
IA3 = (ro(3)*pvel(3));
IA4 = (ro(4)*pvel(4));
IA5 = (ro(5)*pvel(5));
IA6 = (ro(6)*pvel(6));
IA7 = (ro(7)*pvel(7));
IA8 = (ro(8)*pvel(8));
IA9 = (ro(9)*pvel(9));
 % calculate the reflection coefficient for each layer

 % normal incidence formula
RC1 = ( IA2 - IA1) / ( IA2 + IA1);
RC2 = ( IA3 - IA2) / ( IA3 + IA2);
RC3 = ( IA4 - IA3) / ( IA4 + IA3);
RC4 = ( IA5 - IA4) / ( IA5 + IA4);
RC5 = ( IA6 - IA5) / ( IA6 + IA5);
RC6 = ( IA7 - IA6) / ( IA7 + IA6);
RC7 = ( IA8 - IA7) / ( IA8 + IA7);
RC8 = ( IA9 - IA8) / ( IA9 + IA8);
% calculation of two way travel time for each layer

twt1 = ((2*L(1))/ pvel(1));
twt2 = (twt1+(2*(L(1)+ L(2)))/ pvel(2));
twt3 = (twt2+(2*(L(1)+ L(2)+ L(3)))/ pvel(3));
twt4 = (twt3+(2*(L(1)+ L(2)+ L(3)+ L(4)))/ pvel(4));
twt5 = (twt4+(2*(L(1)+ L(2)+ L(3)+ L(4)+ L(5)))/ pvel(5));
twt6 = (twt5+(2*(L(1)+ L(2)+ L(3)+ L(4)+ L(5)+ L(6)))/ pvel(6));
twt7 = (twt6+(2*(L(1)+ L(2)+ L(3)+ L(4)+ L(5)+ L(6)+ L(7)))/ pvel(7));
twt8 = (twt7+(2*(L(1)+ L(2)+ L(3)+ L(4)+ L(5)+ L(6)+ L(7)+ L(8)))/ pvel(8));

twt = [twt1, twt2, twt3, twt4, twt5, twt6, twt7, twt8];
%dt is sample interval
dt = 0.00002;
%generate the series of zeros upto 10000
N = 100;
for n=1:N
    R(n) = 0;
end

%calculate the sample no where we have to place the value of R.C
n1 = twt(1)/dt;
n1 = round (n1);
R(n1) = RC1;
IA(n1) = IA1;
% for second layer
n2 = twt(2)/dt;
n2 = round (n2);
```

```
59 -    R(n2) = RC2;
60 -    IA(n2) = IA2;
61      %for third layer
62 -    n3 = twt(3)/dt;
63 -    n3 = round (n3);
64 -    R(n3) = RC3;
65 -    IA(n3) = IA3;
66      %for fourth layer
67 -    n4 = twt(4)/dt;
68 -    n4 = round (n4);
69 -    R(n4) = RC4;
70 -    IA(n4) = IA4;
71      %for fivt layer
72 -    n5 = twt(5)/dt;
73 -    n5 = round (n5);
74 -    R(n5) = RC5;
75 -    IA(n5) = IA5;
76      %for sixth layer
77 -    n6 = twt(6)/dt;
78 -    n6 = round (n6);
79 -    R(n6) = RC6;
80 -    IA(n6) = IA6;
81      %for seventh layer
82 -    n7 = twt(7)/dt;
83 -    n7 = round (n7);
84 -    R(n7) = RC7;
85 -    IA(n7) = IA7;
86      %for eight layer
87 -    n8 = twt(8)/dt;
88 -    n8 = round (n8);
89 -    R(n8) = RC8;
90 -    IA(n8) = IA8;
91
92      %generate ricker wavelet by a function of ricker that is made
93
94 -    wt = ricker (30,0.0002);
95      %convolve the ricker wavelet with series of reflectivity
96 -    y = conv(wt,R);
97
98      %generate the figures
99
100 -   figure(1); %reflection coefficient
101 -   stem(R,'c','linew',2);
102 -   ylabel('Reflection coefficient');
103 -   xlabel('two-way time');
104 -   title ('Reflectivity series');
105 -   view([90 90])
106 -   figure(2); %ricker wavelet
107
108 -   plot(wt,'r','linew',2);
109 -   ylabel('Amplitude');
110 -   xlabel('two-way time');
111 -   title ('Ricker 40Hz at 2ms');
112 -   figure(3);% synthetic seismogram
113 -   plot(y,'b','linew',1.5);
114 -   view([90 90])
115 -   ylabel('Amplitude');
116 -   xlabel('two-way time');
117 -   title ('synthetic seismogram');
```

References

Agosta, F., & Aydin, A. (2006). Architecture and deformation mechanism of a basin-bounding normal fault in Mesozoic platform carbonates, central Italy. Journal of Structural Geology, 28(8), 1445-1467.

Agosta, F., Alessandroni, M., Tondi, E. and Aydin, A., 2009. Oblique normal faulting along the northern edge of the Majella Anticline, central Italy: Inferences on hydrocarbon migration and accumulation. Journal of Structural Geology, 31(7), pp.674-690.

Agosta, F., Alessandroni, M., Antonellini, M., Tondi, E. and Giorgioni, M., 2010. From fractures to flow: A field-based quantitative analysis of an outcropping carbonate reservoir. Tectonophysics, 490(3-4), pp.197-213.

Agosta, F., Ruano, P., Rustichelli, A., Tondi, E., Galindo-Zaldívar, J. and de Galdeano, C.S., 2012. Inner structure and deformation mechanisms of normal faults in conglomerates and carbonate grainstones (Granada Basin, Betic Cordillera, Spain): Inferences on fault permeability. Journal of Structural Geology, 45, pp.4-20.

Agosta, F., Giuseppe Longhitano, S., Mazzoli, S., Minelli, G. and Tondi, E., 2019. Geofluids and Energy for the XXI Century.

Al-Salmi, M., John, C.M. and Hawie, N., 2019. Quantitative controls on the regional geometries and heterogeneities of the Rayda to Shu'aiba formations (Northern Oman) using forward stratigraphic modelling. Marine and Petroleum Geology, 99, pp.45-60.

Alaei, B., 2012. Seismic modeling of complex geological structures. Seismic Waves-Research and Analysis, 11.

Aminu, M.D., Nabavi, S.A., Rochelle, C.A. and Manovic, V., 2017. A review of developments in carbon dioxide storage. Applied Energy, 208, pp.1389-1419.

Amour, F., Mutti, M., Christ, N., Immenhauser, A., Benson, G.S., Agar, S.M., Tomás, S. and Kabiri, L., 2013. Outcrop analog for an oolitic carbonate ramp reservoir: A scale-dependent geologic modeling approach based on stratigraphic hierarchy. AAPG bulletin, 97(5), pp.845-871.

Anselmetti, F.S. and Eberli, G.P., 1993. Controls on sonic velocity in carbonates. Pure and Applied geophysics, 141(2), pp.287-323.

Anselmetti, F.S., Eberli, G.P. and Bernoulli, D., 1997. Seismic modeling of a carbonate platform margin (Montagna della Maiella, Italy): Variations in seismic facies and implications for sequence stratigraphy. In Carbonate seismology (pp. 373-406). Society of Exploration Geophysicists.

Antonellini, M., Tondi, E., Agosta, F., Aydin, A. and Cello, G., 2008. Failure modes in deep-water carbonates and their impact for fault development: Majella Mountain, Central Apennines, Italy. Marine and Petroleum Geology, 25(10), pp.1074-1096.

Avseth, P. and Bachrach, R., 2005. Seismic properties of unconsolidated sands: Tangential stiffness, Vp/Vs ratios and diagenesis. In SEG Technical Program Expanded Abstracts 2005 (pp. 1473-1476). Society of Exploration Geophysicists.

Avseth, P., Mukerji, T. and Mavko, G., 2010. Quantitative seismic interpretation: Applying rock physics tools to reduce interpretation risk. Cambridge university press.

Avseth, P., 2015. Explorational rock physics: the link between geological processes and geophysical observables. In Petroleum Geoscience (pp. 455-488). Springer, Berlin, Heidelberg.

Bano, M., Edel, J. B., Herquel, G., & EPGS class 2001–2002. (2002). Geophysical investigation of a recent shallow fault. The Leading Edge, 21(7), 648-650.

Bassi, D., Nebelsick, J.H., Puga-Bernabéu, Á. and Luciani, V., 2013. Middle Eocene Nummulites and their offshore re-deposition: A case study from the Middle Eocene of the Venetian area, northeastern Italy. Sedimentary Geology, 297, pp.1-15.

Baud, P., Klein, E. and Wong, T.F., 2004. Compaction localization in porous sandstones: spatial evolution of damage and acoustic emission activity. Journal of Structural Geology, 26(4), pp.603-624.

Baud, P., Vinciguerra, S., David, C., Cavallo, A., Walker, E., & Reuschlé, T. (2009). Compaction and failure in high porosity carbonates: Mechanical data and microstructural observations. Pure and Applied Geophysics, 166(5), 869-898.

Bernoulli, D., 1972. North Atlantic and Mediterranean Mesozoic facies: a comparison. Initial reports of the deep sea drilling project, 11, pp.801-871.

Bernoulli, D., 2001. Mesozoic-Tertiary carbonate platforms, slopes and basins of the external Apennines and Sicily. In Anatomy of an orogen: The Apennines and adjacent Mediterranean basins (pp. 307-325). Springer, Dordrecht.

Billi, A., Salvini, F. and Storti, F., 2003. The damage zone-fault core transition in carbonate rocks: implications for fault growth, structure and permeability. Journal of Structural geology, 25(11), pp.1779-1794.

Birch, F., 1960. The velocity of compressional waves in rocks to 10 kilobars: 1. Journal of Geophysical Research, 65(4), pp.1083-1102.

Birch, F., 1961. The velocity of compressional waves in rocks to 10 kilobars: 2. Journal of Geophysical Research, 66(7), pp.2199-2224.

Bosellini, A., 1991. Introduzione allo studio delle rocce carbonatiche. Bovolenta.

Bosellini, A., Bosellini, F., Colalongo, M.L., Parente, M., Russo, A. and Vescogni, A., 1999. Stratigraphic architecture of the Salento coast from Capo d'Otranto to S. Maria di Leuca (Apulia, southern Italy).

Bosellini A., 2002. "Dinosaurs «re-write» the geodynamics of the eastern Mediterranean and the paleogeography of the Apulia Platform." Earth Science Reviews, 59, 211–234.

Bosellini A., 2004. "The western passive margin of Adria and its carbonate platforms". Special Vol. of Ita. Geol. Soc. for the 32nd IGC Florence-2004, 79-92.

Bons, P. D., Elburg, M. A., & Gomez-Rivas, E. (2012). A review of the formation of tectonic veins and their microstructures. Journal of Structural Geology, 43, 33-62.

Botter, C., Cardozo, N., Hardy, S., Lecomte, I., Escalona, A., 2014. From mechanical modeling to seismic imaging of faults: a synthetic workflow to study the impact of faults on seismic. Marine and Petoleum Geology 57, 187–207. https://doi.org/10.1016/j.marpetgeo.2014.05.013.

Botter, C., Cardozo, N., Qu, D., Tveranger, J. and Kolyukhin, D., 2017. Seismic characterization of fault facies models. Interpretation, 5(4), pp.SP9-SP26.

Braathen, A., Tveranger, J., Fossen, H., Skar, T., Cardozo, N., Semshaug, S.E., Bastesen, E. and Sverdrup, E., 2009. Fault facies and its application to sandstone reservoirs. AAPG bulletin, 93(7), pp.891-917.

Brandano, M., Morsilli, M., Vannucci, G., Parente, M., Bosellini, F. and Mateu-Vicens, G., 2010. Rhodolith-rich lithofacies of the Porto Badisco Calcarenites (upper Chattian, Salento, southern Italy). Italian journal of geosciences, 129(1), pp.119-131.

Brandano, M., Lipparini, L., Campagnoni, V. and Tomassetti, L., 2012. Downslope-migrating large dunes in the Chattian carbonate ramp of the Majella Mountains (Central Apennines, Italy). Sedimentary Geology, 255, pp.29-41.

Brandano, M., Cornacchia, I., Raffi, I. and Tomassetti, L., 2016. The Oligocene–Miocene stratigraphic evolution of the Majella carbonate platform (Central Apennines, Italy). Sedimentary Geology, 333, pp.1-14.

Brandano, M., Tomassetti, L., Trippetta, F. and Ruggieri, R., 2020. Facies heterogeneities and 3D porosity modelling in an Oligocene (Upper Chattian) carbonate ramp, Salento peninsula, southern Italy. Journal of Petroleum Geology, 43(2), pp.191-208.

Burchette, T.P., 2012. Carbonate rocks and petroleum reservoirs: a geological perspective from the industry. Geological Society, London, Special Publications, 370(1), pp.17-37.

Buxton, M.W.N. and Pedley, H.M., 1989. Short Paper: A standardized model for Tethyan Tertiary carbonate ramps. Journal of the Geological Society, 146(5), pp.746-748.

Caine, J.S., Evans, J.P. and Forster, C.B., 1996. Fault zone architecture and permeability structure. Geology, 24(11), pp.1025-1028.

Calderón-Macías, C., Sen, M.K. and Stoffa, P.L., 2000. Artificial neural networks for parameter estimation in geophysics [Link]. Geophysical prospecting, 48(1), pp.21-47.

Campagnoni, V., Tomassetti, L., Lipparini, L., Brandano, M. and Pignatti, J., 2013. Core based facies analysis of the Oligocene/Miocene offshore central Adriatic Sea, Italy. Journal of Mediterranean Earth Sciences, 5, p.19.

Carcione, J.M., Herman, G.C. and Ten Kroode, A.P.E., 2002. Seismic modeling. Geophysics, 67(4), pp.1304-1325.

Catuneanu, O., 2006. Principles of sequence stratigraphy. Elsevier.

Chambers, R.L., Yarus, J.M. and Hird, K.B., 2000. Petroleum geostatistics for nongeostaticians: Part 2. The Leading Edge, 19(6), pp.592-599.

Cho, D., Hogan, C. and Margrave, G.F., 2007. Acoustic finite difference parameter analysis and modelling in MATLAB. Crewes Project Report, 19(1), pp.1-7.

Cilona, A., Baud, P., Tondi, E., Agosta, F., Vinciguerra, S., Rustichelli, A., & Spiers, C. J. (2012). Deformation bands in porous carbonate grainstones: Field and laboratory observations. Journal of Structural Geology, 45, 137-157.

Cornacchia, I., Andersson, P., Agostini, S., Brandano, M. and Di Bella, L., 2017. Strontium stratigraphy of the upper Miocene Lithothamnion Limestone in the Majella Mountain, central Italy, and its palaeoenvironmental implications. Lethaia, 50(4), pp.561-575.

D’Argenio B., 1976. “Le piattaforme carbonatiche periadriatiche.Una rassegna di problemi nel quadro geodinamico mesozoico dell’area mediterranea”. Memorie della Società Geologica Italiana, 18, pp 1-28.

Danaei, S., Neto, G.M.S., Schiozer, D.J. and Davolio, A., 2020. Using petro-elastic proxy model to integrate 4D seismic in ensemble based data assimilation. Journal of petroleum science and engineering, 194, p.107457.

De Franco, R., Petracchini, L., Scrocca, D., Caielli, G., Montegrossi, G., Santilano, A. and Manzella, A., 2019. Synthetic Seismic Reflection Modelling in a Supercritical Geothermal System: An Image of the K-Horizon in the Larderello Field (Italy). Geofluids, 2019.

Di Luzio, E., Bianchi-Fasani, G., Esposito, C., Saroli, M., Cavinato, G. P., & Scarascia-Mugnozza, G. (2004). Massive rock-slope failure in the Central Apennines (Italy): the case of the Campo di Giove rock avalanche. Bulletin of Engineering Geology and the Environment, 63(1), 1-12.

Dockrill, B. and Shipton, Z.K., 2010. Structural controls on leakage from a natural CO2 geologic storage site: Central Utah, USA. Journal of Structural Geology, 32(11), pp.1768-1782.

Dubrule, O. 1998. Geostatistics in Petroleum Geology, AAPG Course Note Series, AAPG, Tulsa, 38, 52.

Duchesne, M.J., Long, B.F., Labrie, J. and Simpkin, P.G., 2006. On the use of computerized tomography scan analysis to determine the genesis of very high resolution seismic reflection facies. Journal of Geophysical Research: Solid Earth, 111(B10).

Dunham, R.J., 1962. Classification of carbonate rocks according to depositional textures. AAPG Mem., 1, pp. 108–121.

Dvorkin, J., Gutierrez, M.A. and Grana, D., 2014. Seismic reflections of rock properties. Cambridge University Press.

Eberli, G.P., Bernoulli, D., Sanders, D. and Vecsei, A., 1993. From Aggradation to Progradation: The Maiella Platform, Abruzzi, Italy: Chapter 18.

Eberli, G.P., Baechle, G.T., Anselmetti, F.S. and Incze, M.L., 2003. Factors controlling elastic properties in carbonate sediments and rocks. The Leading Edge, 22(7), pp.654-660.

Eberli, G.P., Masaferro, J.L. and Sarg, J.R., 2004. Seismic imaging of carbonate reservoirs and systems.

Eberli, G.P. and Betzler, C., 2019. Characteristics of modern carbonate contourite drifts. Sedimentology, 66(4), pp.1163-1191.

Eloni, R., Sahidu, M.H., Panggeleng, I., Birt, C.S. and Manning, T., 2016. From Chaos to Caves–An Evolution of Seismic Karst Interpretation at the Vorwata Field.

Embry A.F. and Klovan. J.E, (1971). “A Late Devonian reef tract on northeastern Banks Island, Northwest Territories”. Bull. Can. Pet. Geol., 33, pp. 730–781.

Ercoli, M., Pauselli, C., Frigeri, A., Forte, E. and Federico, C., 2013. “Geophysical paleoseismology” through high resolution GPR data: A case of shallow faulting imaging in Central Italy. Journal of Applied Geophysics, 90, pp.27-40.

Esmaeilzadeh, S., Afshari, A. and Motafakkerfard, R., 2013. Integrating Artificial Neural Networks Technique and Geostatistical Approaches for 3D Geological Reservoir Porosity modeling with an Example from One of Iran's Oil Fields. Petroleum science and technology, 31(11), pp.1175-1187.

Faleide, T. S., Braathen, A., Lecomte, I., Mulrooney, M. J., Midtkandal, I., Bugge, A. J., & Planke, S. (2021). Impacts of seismic resolution on fault interpretation: Insights from seismic modelling. Tectonophysics, 816(February), 229008. https://doi.org/10.1016/j.tecto.2021.229008

Falivene, O., Arbues, P., Gardiner, A., Pickup, G., Munoz, J.A. and Cabrera, L., 2006. Best practice stochastic facies modeling from a channel-fill turbidite sandstone analog (the Quarry outcrop, Eocene Ainsa basin, northeast Spain). AAPG bulletin, 90(7), pp.1003-1029.

Falivene, O., Arbués, P., Ledo, J., Benjumea, B., Muñoz, J.A., Fernández, O. and Martínez, S., 2010. Synthetic seismic models from outcrop-derived reservoir-scale three-dimensional facies models: The Eocene Ainsa turbidite system (southern Pyrenees). AAPG bulletin, 94(3), pp.317-343.

Fortin, J., Stanchits, S., Dresen, G. and Guéguen, Y., 2006. Acoustic emission and velocities associated with the formation of compaction bands in sandstone. Journal of Geophysical Research: Solid Earth, 111(B10).

Fossen, H., R. Schultz, and A. Torabi (2011), Conditions and implications for compaction band formation in the Navajo Sandstone, Utah, J. Struct. Geol., 33(10), 1477– 1490, doi:10.1016/j.jsg.2011.08.001.

Fossen, H., 2016. Structural geology. Cambridge university press.

Fournier, F., & Borgomano, J. (2007). Geological significance of seismic reflections and imaging of the reservoir architecture in the Malampaya gas field (Philippines). AAPG bulletin, 91(2), 235-258.

Ghisetti, F., & Vezzani, L. (2002). Normal faulting, extension and uplift in the outer thrust belt of the central Apennines (Italy): role of the Caramanico fault. Basin Research, 14(2), 225-236.

Giles, M.R., 1987. Mass transfer and problems of secondary porosity creation in deeply buried hydrocarbon reservoirs. Marine and Petroleum Geology, 4(3), pp.188-204.

Giorgioni, M., Cilona, A., Tondi, E. and Agosta, F., 2011, March. Fault Zone Properties In The Roman Valley Quarry Reservoir Analogue: Insight For Well Logs, Core And Field Data. In Offshore Mediterranean Conference and Exhibition. OnePetro.

Greenfield, L., Millett, J.M., Howell, J., Jerram, D.A., Watton, T., Healy, D., Hole, M.J. and Planke, S., 2020. The 3D facies architecture and petrophysical properties of hyaloclastite delta deposits: An integrated photogrammetry and petrophysical study from southern Iceland. Basin Research, 32(5), pp.1091-1114.

Grippa, A., Hurst, A., Palladino, G., Iacopini, D., Lecomte, I. and Huuse, M., 2019. Seismic imaging of complex geometry: Forward modeling of sandstone intrusions. Earth and Planetary Science Letters, 513, pp.51-63.

Hadizadeh, J. and Rutter, E.H., 1983. The low temperature brittle-ductile transition in a quartzite and the occurrence of cataclastic flow in nature. Geologische Rundschau, 72(2), pp.493-509.

Hairabian, A., Fournier, F., Borgomano, J. and Nardon, S., 2014. Depositional facies, pore types and elastic properties of deep-water gravity flow carbonates. Journal of Petroleum Geology, 37(3), pp.231-249.

Heap, M.J., Brantut, N., Baud, P. and Meredith, P.G., 2015. Time-dependent compaction band formation in sandstone. Journal of Geophysical Research: Solid Earth, 120(7), pp.4808-4830.

Heinemann, N., Booth, M.G., Haszeldine, R.S., Wilkinson, M., Scafidi, J. and Edlmann, K., 2018. Hydrogen storage in porous geological formations–onshore play opportunities in the midland valley (Scotland, UK). International Journal of Hydrogen Energy, 43(45), pp.20861-20874.

Hilterman, F.J., 2001. Seismic amplitude interpretation. Society of Exploration Geophysicists and European Association of Geoscientists and Engineers.

Iacopini, D. and Butler, R.W., 2011. Imaging deformation in submarine thrust belts using seismic attributes. Earth and Planetary Science Letters, 302(3-4), pp.414-422.

Jafarian, E., de Jong, K., Kleipool, L.M., Scheibner, C., Blomeier, D.P. and Reijmer, J.J., 2018. Synthetic seismic model of a Permian biosiliceous carbonate–carbonate depositional system (Spitsbergen, Svalbard Archipelago). Marine and Petroleum Geology, 92, pp.78-93.

Janson, X., Kerans, C., Bellian, J.A. and Fitchen, W., 2007a. Three-dimensional geological and synthetic seismic model of Early Permian redeposited basinal carbonate deposits, Victorio Canyon, west Texas. AAPG bulletin, 91(10), pp.1405-1436.

Janson, X., Eberli, G.P., Bonnaffe, F., Gaumet, F. and De Casanove, V., 2007b. Seismic expressions of a Miocene prograding carbonate margin, Mut Basin, Turkey. AAPG bulletin, 91(5), pp.685-713.

Janson, X., Fomel, S., Martinsen, O.J., Pulham, A.J., Haughton, P.D.W. and Sullivan, M.D., 2011. 3-D forward seismic model of an outcrop-based geocellular model. Concepts in Sedimentology and Paleontology, 10, pp.87-106.

Journel, A.G. and Ying, Z., 2001. The theoretical links between sequential Gaussian simulation, Gaussian truncated simulation, and probability field simulation. Mathematical Geology, 33(1), pp.31-40.

Kolyukhin, D.R., Lisitsa, V.V., Protasov, M.I., Qu, D., Reshetova, G.V., Tveranger, J., Tcheverda, V.A. and Vishnevsky, D.M., 2017. Seismic imaging and statistical analysis of fault facies models. Interpretation, 5(4), pp.SP71-SP82.

Lallier, F., Caumon, G., Borgomano, J., Viseur, S., Fournier, F., Antoine, C., & Gentilhomme, T. 2012. Relevance of the stochastic stratigraphic well correlation approach for the study of complex carbonate settings: Application to the Malampaya buildup (Offshore Palawan, Philippines). Geological Society, London, Special Publications, 370(1), 265-275.

Liner, C. L., & Liner, J. L. (1997). Application of GPR to a site investigation involving shallow faults. The Leading Edge, 16(11), 1649-1651.

Lipparini, L., Trippetta, F., Ruggieri, R., Brandano, M. and Romi, A., 2018. Oil distribution in outcropping carbonate-ramp reservoirs (Maiella Mountain, Central Italy): Three-dimensional models constrained by dense historical well data and laboratory measurements. AAPG Bulletin, 102(7), pp.1273-1298.

Macgregor, D.S. and Moody, R.T., 1998. Mesozoic and Cenozoic petroleum systems of North Africa. Geological Society, London, Special Publications, 132(1), pp.201-216.

Malvić, T., Pimenta Dinis, M.A., Velić, J., Sremac, J., Ivšinović, J., Bošnjak, M., Barudžija, U. and Veinović, Ž., 2020. Geological risk calculation through probability of success (PoS), applied to radioactive waste disposal in deep wells: A conceptual study in the pre-neogene basement in the northern Croatia. Processes, 8(7), p.755.

Manthena, D.V., Kadiyala, A. and Kumar, A., 2009. Interpolation of radon concentrations using GIS-based kriging and cokriging techniques.

Manzocchi, T., Childs, C. and Walsh, J.J., 2010. Faults and fault properties in hydrocarbon flow models. Geofluids, 10(1-2), pp.94-113.

Marchegiani, L., Van Dijk, J.P., Gillespie, P.A., Tondi, E. and Cello, G., 2006. Scaling properties of the dimensional and spatial characteristics of fault and fracture systems in the Majella Mountain, central Italy. Geological Society, London, Special Publications, 261(1), pp.113-131.

Marini, A. I., & Spadafora, E., 2014. G&G Data Integration to Model a Carbonate Giant Field: Predicting & Managing Reservoir Properties in an Underexplored Basin till Production Phase. In Abu Dhabi International Petroleum Exhibition and Conference. Society of Petroleum Engineers.

Margrave, G.F. and Lamoureux, M.P., 2019. Numerical methods of exploration seismology: With algorithms in MATLAB®. Cambridge University Press.

Mascolo, V. and Lecomte, I., 2021. Seismic modelling of outcrop carbonate systems: an application to the Cretaceous platform-to-basin system of the Maiella Mountain (central Apennines, Italy). Geological Society, London, Special Publications, 509.

Matheron, G., Beucher, H., de Fouquet, C., Galli, A., Guerillot, D. and Ravenne, C., 1987, September. Conditional simulation of the geometry of fluvio-deltaic reservoirs. In Spe annual technical conference and exhibition. OnePetro.

Mavko, G. and Bandyopadhyay, K., 2009. Approximate fluid substitution for vertical velocities in weakly anisotropic VTI rocks. Geophysics, 74(1), pp.D1-D6.

Michie, E.A.H., 2015. Influence of host lithofacies on fault rock variation in carbonate fault zones: A case study from the Island of Malta. Journal of Structural Geology, 76, pp.61-79.

Michie, E.A.H. and Haines, T.J., 2016. Variability and heterogeneity of the petrophysical properties of extensional carbonate fault rocks, Malta. Petroleum Geoscience, 22(2), pp.136-152.

Moczo, P., Robertsson, J.O. and Eisner, L., 2007. The finite-difference time-domain method for modeling of seismic wave propagation. Advances in geophysics, 48, pp.421-516.

Mollema, P.N. and Antonellini, M., 1999. Development of strike-slip faults in the dolomites of the Sella Group, Northern Italy. Journal of Structural Geology, 21(3), pp.273-292.

Mollema, P.N. and Antonellini, M.A., 1996. Compaction bands: a structural analog for anti-mode I cracks in aeolian sandstone. Tectonophysics, 267(1-4), pp.209-228.

Mutti, M., Bernoulli, D., Eberli, G.P. and Vecsei, A., 1996. Depositional geometries and facies associations in an Upper Cretaceous prograding carbonate platform margin (Orfento Supersequence, Maiella, Italy). Journal of Sedimentary Research, 66(4), pp.749-765.

Mutti, M., Bernoulli, D. and Stille, P., 1997. Temperate carbonate platform drowning linked to Miocene oceanographic events: Maiella platform margin, Italy. Terra Nova, 9(3), pp.122-125.

Mutti, M., Bernoulli, D., Spezzaferri, S. and Stille, P., 1999. Lower and Middle Miocene carbonate facies in the central Mediterranean: the impact of paleoceanography on sequence stratigraphy.

Myers, D.E., 1984. Co-kriging—New developments. In Geostatistics for natural resources characterization (pp. 295-305). Springer, Dordrecht.

Neto, G.M.S., Davolio, A. and Schiozer, D.J., 2020. 3D seismic data assimilation to reduce uncertainties in reservoir simulation considering model errors. Journal of petroleum science and engineering, 189, p.106967.

Palaz, I., Marfurt, K.J., 1997. Carbonate Seismology, Carbonate Seismology. https://doi.org/10.1190/1.9781560802099

Palermo, D., Aigner, T., Nardon, S. and Blendinger, W., 2010. Three-dimensional facies modeling of carbonate sand bodies: Outcrop analog study in an epicontinental basin (Triassic, southwest Germany). AAPG bulletin, 94(4), pp.475-512.

Patacca, E., Scandone, P., Di Luzio, E., Cavinato, G.P. and Parotto, M., 2008. Structural architecture of the central Apennines: Interpretation of the CROP 11 seismic profile from the Adriatic coast to the orographic divide. Tectonics, 27(3).

Patra, M. and Karttunen, M., 2006. Stencils with isotropic discretization error for differential operators. Numerical Methods for Partial Differential Equations: An International Journal, 22(4), pp.936-953.

Pauselli, C., Federico, C., Frigeri, A., Orosei, R., Barchi, M. R., & Basile, G. (2010). Ground penetrating radar investigations to study active faults in the Norcia Basin (central Italy). Journal of applied geophysics, 72(1), 39-45.

Pisani, L., Antonellini, M., D'Angeli, I.M. and De Waele, J., 2021. Structurally controlled development of a sulfuric hypogene karst system in a fold-and-thrust belt (Majella Massif, Italy). Journal of Structural Geology, 145, p.104305.

Pizzi, A., Falcucci, E., Gori, S., Galadini, F., Messina, P., Di Vincenzo, M., Esestime, P., Giaccio, B., & Sposato, A., 2010. Active faulting in the Maiella massif (central Apennines, Italy). GeoActa, 3, 57-73.

Pomar, L. and Kendall, C., 2008. Architecture of carbonate platforms: a response to hydrodynamics and evolving ecology. In Controls on carbonate platform and reef development (Vol. 89, pp. 187-216). SEPM Special Publication.

Pomar, L., Mateu-Vicens, G., Morsilli, M. and Brandano, M., 2014. Carbonate ramp evolution during the late Oligocene (Chattian), Salento Peninsula, southern Italy. Palaeogeography, Palaeoclimatology, Palaeoecology, 404, pp.109-132.

Pomar, L., Esteban, M., Martinez, W., Espino, D., de Ott, V. C., Benkovics, L., & Leyva, T. C., 2015. Oligocene–Miocene carbonates of the Perla Field, Offshore Venezuela: Depositional model and facies architecture.

Pomar, L., Baceta, J.I., Hallock, P., Mateu-Vicens, G. and Basso, D., 2017. Reef building and carbonate production modes in the west-central Tethys during the Cenozoic. Marine and Petroleum Geology, 83, pp.261-304.

Qui, L., Carr, T.R. and Goldstein, R.H., 2007. Geostatistical three-dimensional modeling of oolite shoals, St. Louis Limestone, pp.69-96.

Rabbani, A., Ong*, O., Chen, X., Schmitt, D., Nycz, J. and Gray, K., 2016. Rock physics laboratory experiments on bitumen-saturated carbonates from the Grosmont Formation, Alberta. In SEG Technical Program Expanded Abstracts 2016 (pp. 3464-3467). Society of Exploration Geophysicists.

Racey, A., 2001. A review of Eocene nummulite accumulations: structure, formation and reservoir potential. Journal of petroleum geology, 24(1), pp.79-100.

Raffi, I., Ricci, C., Garzarella, A., Brandano, M., Cornacchia, I. and Tomassetti, L., 2016. Calcareous nannofossils as a dating tool in shallow marine environment: an example from an upper Paleogene carbonate platform succession in the Mediterranean. Newsletters on Stratigraphy, 49(3), pp.481-495.

Romano, V., Hyman, J.D.H., Karra, S., Valocchi, A.J., Battaglia, M. and Bigi, S., 2017. Numerical modeling of fluid flow in a fault zone: a case of study from Majella Mountain (Italy). Energy Procedia, 125, pp.556-560.

Romano, V., Bigi, S., Carnevale, F., De'Haven Hyman, J., Karra, S., Valocchi, A.J., Tartarello, M.C., Battaglia, M., 2020. Hydraulic characterization of a fault zone from fracture distribution. J. Struct. Geol. 135, 104036. https://doi.org/10.1016/j.jsg.2020.104036

Routa, A.K. and Mohanty, P.R., 2020. Seismic imaging of subsurface geological structures by Kirchhoff's migration based on extended Born approximation. Journal of Earth System Science, 129(1), pp.1-10.

Ricchetti, G., Ciaranfi, N., Luperto Sinni, E., Mongelli, F. and Pieri, P., 1988. Geodinamica ed evoluzione sedimentaria e tettonica dell'avampaese apulo. Memorie della Società Geologica Italiana, 41, pp.57-82.

Ruggieri, R. and Trippetta, F., 2020. Petrophysical properties variation of bitumen-bearing carbonates at increasing temperatures from laboratory to model. Geophysics, 85(5), pp.MR297-MR308.

Rusciadelli, G., Sciarra, N. and Mangifesta, M., 2003. 2D modelling of large-scale platform margin collapses along an ancient carbonate platform edge (Maiella Mt., Central Apennines, Italy): geological model and conceptual framework. Palaeogeography, Palaeoclimatology, Palaeoecology, 200(1-4), pp.245-262.

Rusciadelli, G. and Ricci, C., 2008. New geological constraints for the extension of the northern Apulia platform margin west of the Maiella Mt. (Central Apennines, Italy). Bollettino della Società Geologica Italiana, 127(3), pp.375-387.

Rustichelli, A., Tondi, E., Agosta, F., Cilona, A. and Giorgioni, M., 2012. Development and distribution of bed-parallel compaction bands and pressure solution seams in carbonates (Bolognano Formation, Majella Mountain, Italy). Journal of Structural Geology, 37, pp.181-199.

Sager, K., Boehm, C., Ermert, L., Krischer, L. and Fichtner, A., 2018. Sensitivity of seismic noise correlation functions to global noise sources. Journal of Geophysical Research: Solid Earth, 123(8), pp.6911-6921.

San Miguel, G., Aurell, M., Bádenas, B., Martinez, V., Caline, B., Pabian-Goyheneche, C., Rolando, J.P., Grasseau, N., 2013. Facies heterogeneity of a Kimmeridgian carbonate ramp (Jabaloyas, eastern Spain): a combined outcrop and 3D geomodeling analysis. J. Iber. Geol. 39 (2), 233–252.

Sattler, U., Zampetti, V., Schlager, W., & Immenhauser, A. 2004. Late leaching under deep burial conditions: a case study from the Miocene Zhujiang Carbonate Reservoir, South China Sea. Marine and Petroleum Geology, 21(8), 977-992.

Scisciani, V., Tavarnelli, E., & Calamita, F. (2002). The interaction of extensional and contractional deformations in the outer zones of the Central Apennines, Italy. Journal of Structural Geology, 24(10), 1647-1658.

Smeraglia, L., Trippetta, F., Carminati, E., Mollo, S., 2014. Tectonic control on the petrophysical properties of foredeep sandstone in the Central Apennines, Italy. J. Geophys. Res. Solid Earth 119, 9077–9094. https://doi.org/10.1002/2014JB011221.Received

Storti, F., Balsamo, F. and Salvini, F., 2007. Particle shape evolution in natural carbonate granular wear material. Terra Nova, 19(5), pp.344-352.

Sun, Q., Cartwright, J., Wu, S. and Chen, D., 2013. 3D seismic interpretation of dissolution pipes in the South China Sea: Genesis by subsurface, fluid induced collapse. Marine Geology, 337, pp.171-181.

Thanh, H.V., Sugai, Y., Nguele, R. and Sasaki, K., 2019. Integrated workflow in 3D geological model construction for evaluation of CO2 storage capacity of a fractured basement reservoir in Cuu Long Basin, Vietnam. International Journal of Greenhouse Gas Control, 90, p.102826.

Tjolsen, C.B., Jonhsen, G., Halvorsen, G., Ryseth, A. and Damsleth, E., 1996. Seismic data can improve the stochastic facies modeling. SPE Formation Evaluation, 11(03), pp.141-146.

Tomás, S., Zitzmann, M., Homann, M., Rumpf, M., Amour, F., Benisek, M., Marcano, G., Mutti, M. and Betzler, C., 2010. From ramp to platform: building a 3D model of depositional geometries and facies architectures in transitional carbonates in the Miocene, northern Sardinia. Facies, 56(2), pp.195-210.

Tomassetti, L., Petracchini, L., Brandano, M., Trippetta, F. and Tomassi, A., 2018. Modeling lateral facies heterogeneity of an upper Oligocene carbonate ramp (Salento, southern Italy). Marine and Petroleum Geology, 96, pp.254-270.

Tomassetti, L., Petracchini, L., Brandano, M., Mascaro, G. and Scrocca, D., 2021. Stratigraphical and sedimentological relationships of the Bolognano Formation (Oligocene–Miocene, Majella Mountain, Central Apennines, Italy) revealed by geological mapping and 3D visualizations. GEOLOGICA CARPATHICA, 72(1), pp.3-16.

Tomassetti, L., Brandano, M. and Mateu-Vicens, G., 2022. 3D modelling of the upper Tortonian-lower Messinian shallow ramp carbonates of the Hyblean domain (Central Mediterranean, Faro Santa Croce, Sicily). Marine and Petroleum Geology, 135, p.105393.

Tomassi, A., Trippetta, F., de Franco, R. and Ruggieri, R., 2022. From petrophysical properties to forward-seismic modeling of facies heterogeneity in the carbonate realm (Majella Massif, central Italy). Journal of Petroleum Science and Engineering, 211, p.110242. https://doi.org/10.1016/j.petrol.2022.110242.

Tondi, E., Antonellini, M., Aydin, A., Marchegiani, L. and Cello, G., 2006. The role of deformation bands, stylolites and sheared stylolites in fault development in carbonate grainstones of Majella Mountain, Italy. Journal of structural geology, 28(3), pp.376-391.

Trippetta, F., Collettini, C., Barchi, M.R., Lupattelli, A. and Mirabella, F., 2013. A multidisciplinary study of a natural example of a CO2 geological reservoir in central Italy. International Journal of Greenhouse Gas Control, 12, pp.72-83.

Trippetta, F., Carpenter, B.M., Mollo, S., Scuderi, M.M., Scarlato, P. and Collettini, C., 2017. Physical and transport property variations within carbonate-bearing fault zones: insights from the Monte Maggio Fault (Central Italy). Geochemistry, Geophysics, Geosystems, 18(11), pp.4027-4042.

Trippetta, F. and Geremia, D., 2019. The seismic signature of heavy oil on carbonate reservoir through laboratory experiments and AVA modelling. Journal of Petroleum Science and Engineering, 177, pp.849-860.

Trippetta, F., Ruggieri, R., Brandano, M. and Giorgetti, C., 2020. Petrophysical properties of heavy oil-bearing carbonate rocks and their implications on petroleum system evolution: Insights from the Majella Massif. Marine and Petroleum Geology, 111, pp.350-362.

Trippetta, F., Durante, D., Lipparini, L., Romi, A. and Brandano, M., 2021. Carbonate-ramp reservoirs modelling best solutions: Insights from a dense shallow well database in Central Italy. Marine and Petroleum Geology, 126, p.104931.

Tveranger, J., Braathen, A., Skar, T. and Skauge, A., 2005. Centre for Integrated Petroleum Research–Research activities with emphasis on fluid flow in fault zones. Norwegian Journal of Geology, 85(1-2), pp.63-71.

Valencia, F. L., & Laya, J. C. 2020. Deep-burial dissolution in an Oligocene-Miocene giant carbonate reservoir (Perla Limestone), Gulf of Venezuela Basin: Implications on microporosity development. Marine and Petroleum Geology, 113, 104144.

Vecsei, A., Sanders, D.G., Bernoulli, D., Eberli, G.P. and Pignatti, J.S., 1998. Cretaceous to Miocene sequence stratigraphy and evolution of the Maiella carbonate platform margin, Italy.

Vecsei, A. and Sanders, D.G., 1999. Facies analysis and sequence stratigraphy of a Miocene warm-temperate carbonate ramp, Montagna della Maiella, Italy. Sedimentary Geology, 123(1-2), pp.103-127.

ViDEPI Project (2012). Visibility of petroleum exploration data in Italy. MISE, Ministero dello sviluppo economico DGRME, Società Geologica Italiana, and Assomineraria. http://unmig.sviluppoeconomico.gov.it/videpi/videpi.asp.

Vo Thanh, H. and Lee, K.K., 2021. 3D geo-cellular modeling for Oligocene reservoirs: a marginal field in offshore Vietnam. Journal of Petroleum Exploration and Production Technology, pp.1-19.

Volatili, T., Zambrano, M., Cilona, A., Huisman, B.A.H., Rustichelli, A., Giorgioni, M., Vittori, S. and Tondi, E., 2019. From fracture analysis to flow simulations in fractured carbonates: The case study of the Roman Valley Quarry (Majella Mountain, Italy). Marine and Petroleum Geology, 100, pp.95-110.

Wang, Y., Chaudhuri, S.K. and Safavi-Naeini, S., 2002. An FDTD/ray-tracing analysis method for wave penetration through inhomogeneous walls. IEEE Transactions on Antennas and Propagation, 50(11), pp.1598-1604.

Wang, Y., Ge, Q., Lu, W. and Yan, X., 2020. Well-logging constrained seismic inversion based on closed-loop convolutional neural network. IEEE Transactions on Geoscience and Remote Sensing, 58(8), pp.5564-5574.

Wang, Z., Palaz, I. and Marfurt, K.J., 1997. Seismic properties of carbonate rocks. Carbonate seismology, 6, pp.29-52.

Wang, Z., Harbert, W.P., Dilmore, R.M. and Huang, L., 2018. Modeling of time-lapse seismic monitoring using CO2 leakage simulations for a model CO2 storage site with realistic geology: Application in assessment of early leak-detection capabilities. International Journal of Greenhouse Gas Control, 76, pp.39-52.

Weger, R.J., Eberli, G.P., Baechle, G.T., Massaferro, J.L. and Sun, Y.F., 2009. Quantification of pore structure and its effect on sonic velocity and permeability in carbonates. AAPG bulletin, 93(10), pp.1297-1317.

Wibberley, C.A., Yielding, G. and Di Toro, G., 2008. Recent advances in the understanding of fault zone internal structure: a review. Geological Society, London, Special Publications, 299(1), pp.5-33.

Wong, T.F. and Baud, P., 2009. Grain crushing, pore collapse and strain localization in porous sandstone. Mechanics of Natural Solids, pp.239-254.

Yao, T. and Chopra, A., 2000. Integration of seismic attribute map into 3D facies modeling. Journal of petroleum science and engineering, 27(1-2), pp.69-84.

Yuan, H., Han, D.H., Zhao, L., Huang, Q. and Zhang, W., 2018. Rock-physics characterization of bitumen carbonates: A case study. Geophysics, 83(3), pp.B119-B132.

Zambrano, M., Volatili, T., Mancini, L., Pitts, A., Giorgioni, M. and Tondi, E., 2021. Pore-scale dual-porosity and dual-permeability modeling in an exposed multi-facies porous carbonate reservoir. Marine and Petroleum Geology, 128, p.105004.

Zampetti, V., Sattler, U., & Braaksma, H. 2005. Well log and seismic character of Liuhua 11-1 Field, South China Sea; relationship between diagenesis and seismic reflections. Sedimentary Geology, 175(1-4), 217-236.

Zappaterra E., 1994. “Source-rock distribution model of the Periadriatic Region”. AAPG Bulletin, 78, 333–354.

Zhang, W., Youn, S. and Doan, Q.T., 2007. Understanding reservoir architectures and steam-chamber growth at Christina Lake, Alberta, by using

4D seismic and crosswell seismic imaging. SPE Reservoir Evaluation & Engineering, 10(05), pp.446-452.